

Louisiana State University

## LSU Scholarly Repository

---

LSU Doctoral Dissertations

Graduate School

---

2004

### Replication of metal-based high-aspect microscale structures by high temperature micromolding

Dongmei Cao

*Louisiana State University and Agricultural and Mechanical College*

Follow this and additional works at: [https://repository.lsu.edu/gradschool\\_dissertations](https://repository.lsu.edu/gradschool_dissertations)



Part of the [Mechanical Engineering Commons](#)

---

#### Recommended Citation

Cao, Dongmei, "Replication of metal-based high-aspect microscale structures by high temperature micromolding" (2004). *LSU Doctoral Dissertations*. 2078.

[https://repository.lsu.edu/gradschool\\_dissertations/2078](https://repository.lsu.edu/gradschool_dissertations/2078)

This Dissertation is brought to you for free and open access by the Graduate School at LSU Scholarly Repository. It has been accepted for inclusion in LSU Doctoral Dissertations by an authorized graduate school editor of LSU Scholarly Repository. For more information, please contact [gradetd@lsu.edu](mailto:gradetd@lsu.edu).

**REPLICATION OF METAL-BASED HIGH-ASPECT-RATIO MICROSCALE  
STRUCTURES BY HIGH TEMPERATURE MICROMOLDING**

A Dissertation  
Submitted to the Graduate Faculty of the  
Louisiana State University and  
Agricultural and Mechanical College  
in partial fulfillment of the  
requirement for the degree of  
Doctor of Philosophy

in

The Department of Mechanical Engineering

By

Dongmei Cao

B.S., Sichuan University, Chengdu, China, 1996

M.S., Sichuan University, Chengdu, China, 1999

M.S., Louisiana State University, Baton Rouge, U.S.A, 2001

August, 2004

## **DEDICATION**

In the journey of the completion of my degree, including this dissertation, my family has been such an important part for achieving this goal. Although they do not always know what I was doing and what I was going through, their support, love and confidence in me helped me to know that I could accomplish not only this, but many things I chose to do in this life. This dissertation is dedicated to my husband who is always there when I need him to share my laugh and tears and who always encourages me in pursuing my goal; to my Mom and Dad who always understand me and support me in my decision about my academic career; to my brothers who support me both financially and spiritually. Thank you all. Your love has been truly my inspiration.

## ACKNOWLEDGEMENTS

This dissertation would not have been possible without the love and guidance of those who have supported my efforts.

In the journey of my dissertation research, I am deeply indebted to my major professor Dr. Meng for his dedication and support throughout my research and for leading me to countless moments of revelation. Not only so, with his enthusiasm, insights and methodology in the research, he has set an incredible example upon which I can model in my future career. So instead I will simply thank you, your deep influence on my life will keep me thanking you for the rest of my life.

I am grateful to Dr. Kelly for his insightful feedback and timely, indispensable support in this research. I only wish I could have benefited more from your expertise throughout my dissertation process.

I feel so honored to have Dr. Feldman, Dr. Khonsari and Dr. Sprunger to be my dissertation committee members. I thank you all for your time and effort in this dissertation process. I appreciate your positive comments and personal encouragements.

I also want to thank Dr. Sinclair for his contribution in the modeling part in the molding mechanics of metal micromolding in this dissertation.

I would like to thank my husband Wei Guo for putting up with the many hours I spent in the research when I could have contributed to my family activity. I thank you for your understanding and your strong support.

Along the journey, I have received additional encouragements and votes of confidence from my relatives, friends and lab mates. I feel so blessed to have you all around me and I am lucky to have so many and varied examples upon which to model myself in the future.

## TABLE OF CONTENTS

DEDICATION .....	ii
ACKNOWLEDGMENTS .....	iii
ABSTRACT .....	vi
CHAPTER 1. AN OVERVIEW OF THE CURRENTLY DEVELOPED AND UNDERDEVELOPED MICROFABRICATION TECHNOLOGIES FOR METAL MICROSTRUCTURES .....	1
Introduction to Microfabrication .....	1
Microfabrication Techniques for Metal Structures .....	4
High Temperature Micromolding of Metals .....	13
Summary .....	16
References .....	16
CHAPTER 2. FRICTION AND WEAR CHARACTERISTICS OF TITANIUM CONTAINING AMORPHOUS HYDROCARBON CERAMIC NANOCOMPOSITE COATINGS .....	21
Introduction .....	21
Experimental .....	21
Results and Discussion .....	23
Conclusion .....	27
References .....	27
CHAPTER 3 TRIBOLOGICAL CHARACTERIZATION OF Ti-C:H COATINGS BY RAMAN SPECTROSCOPY AND ATOMIC FORCE MICROSCOPY .....	30
Introduction .....	30
Experimental .....	30
Results and Discussion .....	32
Conclusion .....	39
References .....	40
CHAPTER 4 CONFORMAL COATING OF Ti-C:H NANOCOMPOSITES OVER LiGA FABRICATED HIGH-ASPECT-RATIO MICROSCALE STRUCTURES AND ITS MEMS APPLICATION .....	42
Introduction .....	42
Experimental .....	44
Results and Discussion .....	45
Summary .....	52
References .....	52
CHAPTER 5 COMPRESSION MOLDING OF Pb AND Zn WITH LiGA FABRICATED MICROSCALE MOLD INSERTS .....	54

Introduction .....	54
Experimental .....	55
Results and Discussion .....	57
Summary .....	63
References .....	64
 CHAPTER 6 HIGH-TEMPERATURE INSTRUMENTED MICROSCALE COMPRESSION MOLDING OF Pb .....	 66
Introduction .....	66
Experimental .....	67
Results and Discussion .....	68
Summary .....	75
References .....	75
 CHAPTER 7 MICROSCALE COMPRESSION MOLDING OF Al WITH SURFACE ENGINEERED LiGA INSERTS .....	 76
Introduction .....	76
Experimental .....	78
Results and Discussion .....	79
Summary .....	86
References .....	86
 CHAPTER 8 STRESS DURING MICROMOLDING OF METALS AT ELEVATED TEMPERATURES: PILOT EXPERIMENTS AND A SIMPLE MODEL .....	 89
Introduction .....	89
Microscale Compression Molding at Elevated Temperatures .....	91
Development of a Simple Model: Ball Indentation Stresses .....	95
Development of a Simple Model: Post Indentation Stresses .....	99
Tensile Testing at Elevated Temperatures .....	105
Comparison of Experiments with Modeling .....	107
Conclusion .....	110
References .....	111
 CHAPTER 9 GLOBAL CONCLUSION .....	 115
 APPENDIX LETTERS OF COPYRIGHT PERMISSION .....	 116
 VITA .....	 120

## ABSTRACT

In microsystem technology a large range of materials will be available only after the necessary microfabrication technologies have been developed or adapted. More than a decade ago, the existing microfabrication technologies were restricted to structuring and shaping techniques producing three-dimensional microstructures out of silicon, mostly unfilled plastics or a few pure metals or binary alloys. However, the choice of materials for microcomponents is determined by the function and conditions of use of microsystems. Some microdevices can only work well when made of specific metal components. To meet this need, several microfabrication techniques have been developed, such as second electroforming of molded plastic mold, microcasting, microinjection molding, ultra precision micromilling, micro electrical discharge machining, and their modified techniques, each with a certain range of metal choices. In chapter 1, these techniques are reviewed briefly and compared with each other. More importantly, a new technique for fabricating microscale metal structures – high-temperature compression molding is proposed and the related issues are discussed, including surface engineering of the mold insert, molding behavior comparison between molding different metals and molding with surface modified inserts and unmodified inserts, and molding mechanics.

Chapters 2, 3 and 4 focus on the first issue – surface engineering of the mold insert, including characterization of Ti containing hydrocarbon (Ti-C:H) coatings in terms of microstructure, mechanical properties, tribological characteristics and tribochemistry, and conformal coating of Ti-C:H over LiGA fabricated microscale structures. The second issue – molding behavior is discussed in chapters 5, 6 and 7, including preliminary experiments on micromolding of Pd and Zn, instrumented micromolding of Pb and high-temperature instrumented micromolding of Al with LiGA fabricated Ni inserts. Chapter 8 focuses on the third issue – the mechanics of molding. In this chapter, a simple mechanics model of the micromolding process was developed, which relates the stresses on the insert during micromolding primarily to the yield strength of the molded metal and frictional tractions on the sides of the insert. Finally, chapter 9 summarizes this whole dissertation research with main results and achievements highlighted and the future research discussed.

# **CHAPTER 1. AN OVERVIEW OF THE CURRENTLY DEVELOPED AND UNDERDEVELOPED MICROFABRICATION TECHNOLOGIES FOR METAL STRUCTURES**

## **Introduction to Microfabrication**

### **I. Technical Demand and Technological Response**

A large part of the world has reached a high standard of living at the expense of an extensive exploitation of natural resources. It is a highly ranked goal in technologically developed countries to stabilize and to improve this standard. In those parts of the world which are less rich the most important goal is to increase the technological standard in order to reach a standard of living comparable to that in the developed countries <sup>1</sup>. Nevertheless, the consumption of resources can hardly be further increased without causing serious damage to the ecosphere. Therefore, the necessary development can only be made by an increase in efficiency. From this follows a great demand for new systems which consume less and perform better. In order to operate a system in an optimized way, a considerable effort in measurement and control is necessary. This results in an increasing need for small and powerful systems for sensing, analyzing and actuating. These needs prompt the technological world at hand to work out an adequate response. There are a large number of different technologies, ideas, visions and possible interactions. Among these the synergy of two elements are very promising with respect to the specific demands: the first one is an outstanding manufacturing technology -- the microfabrication technology on which attention will be focused in this chapter. The second one is an important new vision and development idea, i.e. the systems approach.

### **II. Microfabrication Technologies**

Microfabrication or micromachining (or micro-manufacturing) was developed in response to demands for new micro-electro-mechanical systems (MEMS). It refers to the technologies and practice of making three dimensional structures and devices with overall dimensions on the order of a few or a few hundred micrometers.

Microfabrication technologies are largely based on microelectronics processing technologies and micromachining. Microelectronics processing technologies, producing integrated electronic circuitry (IC), are very well developed. Micromachining is the generic name covering a range of technologies used to produce micro-scale structures and moving parts.

One of the main goals of microfabrication is to integrate microelectronic circuitry into micromachined structures, to produce completely integrated systems (Microsystems). Such systems could have the same advantages of low cost, reliability and small size as silicon chips produced in the microelectronics industry.

Many efforts from academic institutions and industrial companies have been put in the exploration and study of the microfabrication technologies. Hence, quite a few technologies have been developed and put into practice successfully such as photolithography <sup>2</sup>, Excimer laser micromachining <sup>3 4</sup>, silicon bulk and surface micromachining <sup>5</sup>, LiGA technique <sup>6</sup>, hot embossing <sup>7</sup>. Other techniques are still



underdeveloped but showing some promising results, examples include microcasting<sup>8 9</sup>, microinjecting molding<sup>10 11</sup>, ultra precision micromilling<sup>12</sup>, micro electron discharge machining (EDM)<sup>13 14</sup>, etc.

### A. Photolithography

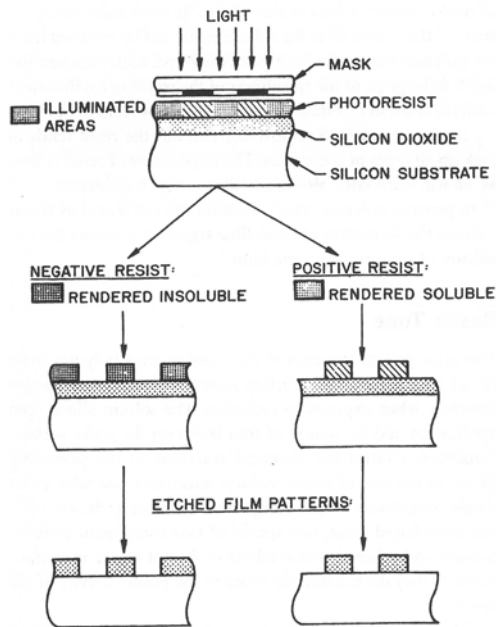


**Fig. 1.1 Process of photolithography**

Photolithography is a basic technique used to define the shape of micromachined structures, and is the foundation of most microfabrication techniques. Fig. 1.1 shows the main steps of the photolithography process. With photolithography, firstly, a mask needs to be produced. This will typically be a chromium pattern on a glass plate. A substrate covered with a thin layer of another type of material which needs to be selectively removed is then coated with a polymer which is sensitive to ultraviolet light, called a photoresist. Ultraviolet light is then shone through the mask onto the photoresist. The photoresist is then developed which transfers the pattern on the mask to the photoresist layer. A chemical (or some other method) is then used to remove the material where it is exposed through the openings in the resist. Finally the resist is removed leaving the patterned structure.

In the IC industry, pattern transfer from masks onto thin films is accomplished almost exclusively via photolithography. Accurate registration and exposure of a series of successive patterns lead to complex multilayered ICs. Photolithography matured rapidly and has become better and better at resolving smaller and smaller features. This essentially two-dimensional process has a limited tolerance for nonplanar topography, creating a major constraint for building microstructures which exhibit extreme topographies<sup>2</sup>.

### B. Excimer Laser Micromachining

Excimer lasers are a family of pulsed lasers operating in the ultraviolet region of the spectrum. The source of the emission is a fast electrical discharge in a high-pressure mixture of a rare gas and a halogen gas. The particular combination of a rare gas and halogen determines the output wavelength. The combination of short ultraviolet wavelengths with high peak and average powers makes Excimer lasers uniquely suited for laser microfabrication. The basic mechanisms of Excimer laser micromachining is based on the absorption of UV energy by various substrate materials. Most metals, glasses, polymers, and other dielectrics used in micromachining absorb UV energy very

intensely, each with a characteristic absorption coefficient. This makes the Excimer laser micromachining applicable to almost all kinds of MEMS materials<sup>4</sup>.

When machining organic materials the laser is operated in the pulsed mode, removing material with each pulse. The amount of material removed is dependent on the material itself, the length of the pulse, and the intensity of the laser light. The shape of the structures produced is controlled by using chrome on quartz mask, like the masks used in photolithography. In the simplest system the mask is placed in contact with the material being machined, and the laser light is shone through it. Material is selectively removed where the laser light strikes it. Structures with vertical sides can be created. By adjusting the optics it is possible to produce structures with tapered sidewalls.

### **C. Silicon Micromachining**

Among the existing microfabrication technologies, silicon micromachining is the most prominent, since it is one of the best developed microfabrication techniques. Silicon is the primary substrate material used in IC production, and is a natural candidate for extension to fabrication of microsystems.

There are a number of basic techniques that can be used to pattern thin films that have been deposited on a silicon wafer, and to shape the wafer itself, to form a set of basic microstructures (bulk silicon micromachining) including photolithography, wet etching, dry etching, lift off technique for noble metals, etc. The techniques for depositing and patterning thin films can be used to produce quite complex microstructures on the surface of silicon wafer (surface silicon micromachining). Electrochemical etching techniques are being investigated to extend the set of basic silicon micromachining techniques. Silicon bonding techniques can also be utilized to extend the structures produced by silicon micromachining techniques into multilayer structures.

With silicon bulk micromaching, one of the simplest possible and most obvious structures is the patterning of insulated electrical conductors. One possible application of this could be to use electric field to manipulate individual cells. Anisotropic etching with KOH can easily form V shaped grooves, or cut pits with tapered walls into silicon. KOH can also be used to produce mesa structures. Silicon diaphragms from about 20 $\mu$ m thick upwards can be made by etching through an entire wafer with KOH. The silicon diaphragm is the basic structure used in microengineered pressure sensors, for example. It can also be adapted for use as an acceleration sensor. Concentration dependent etching can also be used to produce narrow bridges, or cantilever beams. One of the applications for the beams and bridges is as resonant sensors. A combination of dry etching and isotropic wet etching can be used to form very sharp points. Very fine points fabricated on the end of cantilever beams can serve as probes for use in atomic force microscopy. Surface micromaching can potentially produce quit complicated structure; such as microengineered tweezers, and gear trains. Wafer bonding techniques can potentially be combined with some of the basic micromachined structures to form the valves, pumps, etc, of a microfluid handling system.

Silicon micromaching involves only silicon-based materials including crystalline silicon, polycrystalline silicon, silicon dioxide (oxide), silicon nitride, and also some noble metals such as gold. Material selection is restricted to a very narrow range. While

silicon-based materials are easily machined with the well-developed microelectronic processing techniques, they have obvious disadvantages over metal materials when used as the structuring material.

#### D. LiGA Technique

The acronym LiGA comes from the German name for the process (Lithographie, Galvanoformung and Abformung). LiGA uses lithography, electroplating, and molding processes to produce microscale structures. It is capable of creating of very finely defined microstructures of up to 1000 $\mu\text{m}$  in height.

In the process as originally developed, a special kind of photolithography using X-rays (X-ray lithography) is used to produce patterns in very thick layers of photoresist. The X-rays from a synchrotron source are shone through a special mask onto a thick photoresist layer (sensitive to X-rays) which covers a conductive substrate (Fig 1.2a). This resist is then developed (Fig 1.2b). The pattern formed is then electroplated with metal (Fig 1.2c). Such a primary metal structure produced can be the final product; however it is common to use it as a mold insert (Fig 1.2d). This mold insert can then be filled with a suitable materials, such as plastic (Fig 1.2e), to produce the final product in that material (Fig 1.2f).

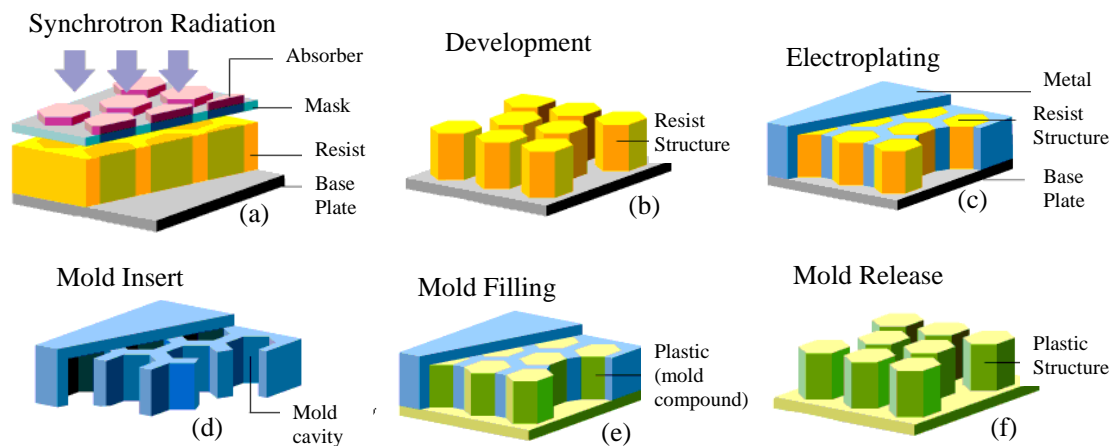


**Fig. 1.2 The LiGA process**

X-ray lithography is superior to optical lithography because of the shorter wavelength and a very large DOF (depth of focus) and due to the fact that exposure time and development conditions are not as stringent. Reproducibility is high as results are almost independent of surface reflections and wafer topography<sup>2</sup>. LiGA exploits all the above advantages of X-ray lithography.

#### Microfabrication Techniques for Metal Structures

In process accompanying the structuring techniques used for silicon, metals are produced as thin layers from the gas phase, or thicker structures are made by electroforming. The LiGA technique was developed to manufacture three-dimensional

microscale structures out of various materials. Today, lithographic process steps furnish only a few polymer resist systems, for example, Polymethyl methacrylate (PMMA). Readily electroplatable materials have been limited to gold, copper, nickel and nickel alloys. Molding techniques is limited to polymeric materials. While material choice for microcomponents is determined by the function and conditions of use of the microsystems, many researchers in different fields are exploring new techniques for improving the efficiency of the microfabrication of metal microscale structures or techniques for microscale structures fabricated with broader range of metal materials. The techniques fall into two broad categories: molding related techniques such as electroplating of lost plastic micromolds<sup>8 15 16</sup> (second electroplating step), microcasting, microinjection molding, hot embossing, micro electrical discharge machining and non-mold-related techniques such as ultra precision micromilling. These processes are reviewed next.

## **I. Electroplating of Lost Plastic Micromolds**

In an economically viable process of manufacturing metal microstructures, an obvious idea is to produce conductive microstructures by an inexpensive molding technique; these microstructures are subsequently inverted into metal microstructures by electroforming. It is for this purpose that V. Piottter et. al.<sup>17</sup> have developed the injection molding of conductive plastics as one way of producing micromolds which can serve as electroforming substrates. In their study, highly filled plastics with a surface resistance of less than 1 kohm are chosen to ensure sufficient conductivity of the plastic micromolds over relatively long cycle times in the electrolyte. The mold inserts employed in injection molding of microstructures are LiGA mold inserts made of nickel, and micromechanically produced mold inserts made of brass, respectively. To avoid abrasive wear of the mold inserts during injection molding, conductive carbon black was used as the filler. Injection molding inverted the microstructure of the mold inserts into a conductive plastics structure. Subsequent electroforming copied the mold inserts in nickel.

Although the dimensions of the microscale structures, and also their surface quality, are electroformed in good quality, detailed examinations of transverse sections of the column-like arrays show cavities shaped like gothic church windows in the nickel body at aspect ratios (height-to-width of the structure) in excess of 5. There are probably caused by the current density distribution between the close-spaced plastic structures and the diffusion coefficient of the nickel ions in the electrolyte. The nickel coat on top of the conductive plastic structures begins at the base, between the plastics structures, and simultaneously at the structural walls. At an aspect ratio of 5, and with close-spaced plastic structures, nickel deposition along the walls is complete before the gap between the plastic microstructure is completely filled with nickel from the base of the structure. This problem is diminished slightly when a very low current density is applied, but it cannot be disposed of entirely. By establishing a conductivity gradient in the plastic microstructures, the problem can also be improved. But even this conductivity gradient was not sufficient with close-spaced plastic microstructures to produce void-free nickel structures. This led to the efforts by A Thies, et. al.<sup>18</sup> on a process using Ag-Cluster deposition to establish conductivity on insulating microstructures (PMMA). In this study, injection molded plastic microstructures made of an insulating plastic material were used,

and a nozzle beam source characterized by high directionality and high density of the cluster beam was then employed to generate a metal coat on the substrate surface and the fronts, but not on the sidewalls, as a consequence of the plane-parallel walls of LiGA microstructures. This method works as long as the metal microstructure to be electroformed has a continuous electroforming starting layer. Failing this, substrate islands are completely surrounded by insulating plastic microstructures. As a consequence, area on the island-shaped substrate surface is not in electrical contact, and there is no metal deposition in these areas. Thus, parts of the structure are missing, and the overall structure produced contains defects and cannot be used.

The process of electroforming of plastic microstructures filled with conductive carbon black does furnish useful metal microstructures. In many applications, especially where metal microstructures are hardly subjected to mechanical loads and stresses, microstructures with voids can also be used, as their structural surface are free from defects.

It is worthy to point out that all methods by which a metal microstructure is produced by electroforming are restricted in their choice of materials to those electrolytes which allow microstructures with high aspect ratio to be deposited. This line of materials at present is limited to copper, gold, nickel, and a few nickel-based alloys. In order to make the full range of materials available in microsystems engineering which is required for future applications of metal microscale structures, and which resembles the range of materials for macroscopic products, additional techniques for fabricating metal microstructures need to be developed.

## **II. Micro Precision Casting**

Micro Precision Casting (microcasting) is a suitable process for the shaping of microparts made of metallic alloys with high mechanical strength and high aspect ratio. As early as in 1997, R. Ruprecht et. al.<sup>8</sup> has developed this new technique. In 2002, G. Baumeister, et. al.<sup>19</sup> made further studies on this process. The process is an improved process applied to the manufacturing of microstructures. This includes structures smaller than 1mm or larger but with extremely fine structures in the  $\mu\text{m}$  range. Like the investment casting process, microcasting is a lost-wax lost- mold process, which is known to obtain the best results concerning precision and surface quality. In this technique, injection molded plastic microstructures are used as lost molds and embedded in a ceramic investment material. While the investment material is baked into a hollow ceramic mold, the plastic microstructures undergo pyrolysis. The heated hollow ceramic mold, whose inner walls carry the image of the plastic microstructures, is filled with molten metal. Complete filling of the mold with molten metal is achieved either by centrifugal casting or by vacuum pressure casting. In centrifugal casting, the mold is filled by the centrifugal force; in vacuum pressure casting, filling is achieved by pouring the molten metal into an evacuated ceramic mold and applying a gas pressure to the molten metal after pouring. After the metal has solidified and the ceramic mold has cooled down, the microcomponent is removed. In microsystem technology the investment material is dissolved selectively without destroying the metal microscale structures by mechanical or chemical attack.

Metal microscale structures of gold alloys and palladium-based alloy as well as aluminum bronze have so far been produced by microcasting. Microcomponents with minimum wall thicknesses of  $50\mu\text{m}$  and aspect ratio of approx. 10 have so far been made successfully. The technique lends itself particularly well to molding fully three-dimensional microstructures. This has been documented by molding, for instance, microturbine housings of 2.5 mm outside diameter and hole structures for the fluid inlet and outlet (see Fig. 1.3). The wall thickness of the center axis, 1mm long, for accepting a hollow turbine shaft is approximately  $110\mu\text{m}$ . The microturbine housings were casted using lost PMMA micromolds injection molded with a mold insert produced by micromechanical cutting and assembly techniques.

Also LiGA structures of various alloys have already been made by microcasting. Compared to the conventional LiGA structures, the surfaces of the metal microscale structures have an increased surface roughness, primarily as a result of the investment materials. One example is shown in Fig. 1.4. The surfaces of the honeycomb walls have an average roughness of slightly less than  $1\mu\text{m}$ . The quality of the structures certainly would be appropriate for use in heat exchanger and catalytic converters, but the present developments of microcasting are intended especially to improve the surface quality of metal microstructures.

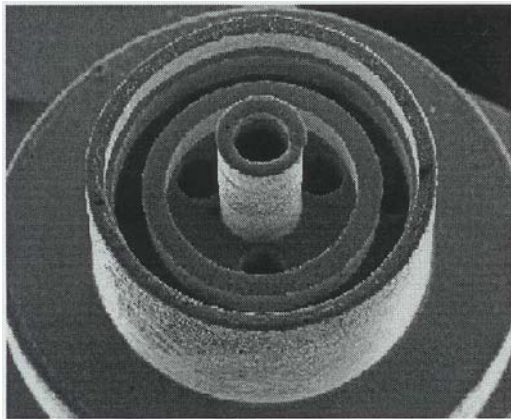


**Fig. 1.3 Microturbine housings of 2.5 mm outside diameter made of Palliag M palladium alloy, produced by microcasting. The hollow center axis of 1mm length has a wall thickness of  $110\mu\text{m}$** <sup>19</sup>

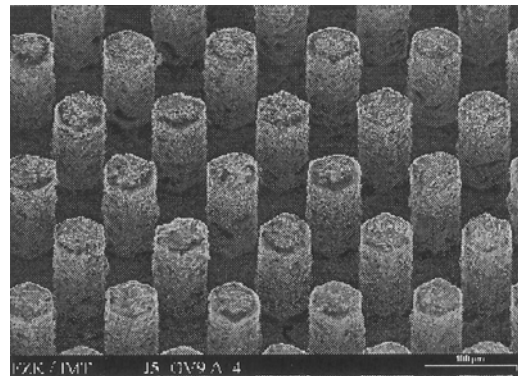


**Fig. 1.4 LiGA honeycomb structures made by microcasting of a palladium alloy. The width across flats of the honeycomb structures is  $50\mu\text{m}$ , the structural height is  $250\mu\text{m}$** <sup>19</sup>

Microcasting allows a considerably broader range of metals compared to electroforming, especially multi-component alloys and superalloys, to be tailored for microsystem engineering application. However, this still does not provide all the metals for microcomponents which have been specially developed for specific macro-engineering applications, such as aluminum-titanium alloys for high-temperature applications, or hard metals for components subject to wear. Moreover, the complicated processing and copying steps compared to other straightforward techniques for metal

microstructures are going to an issue from the economic point of view as well as the efficiency problem when mass fabrication is considered.

### **III. Micro Metal Injection Molding (MIM)**

One economically viable process for mass producing complex precision parts is powder metallurgical injection molding, or Metal Injection Molding (MIM). In 1997 or even earlier R. Ruprecht et. al.<sup>8</sup> developed Micro MIM technique. T. Shimizu et. al.<sup>20</sup> also utilized metal injection molding combined with high aspect ratio structuring to fabricate micro-parts using the supercritical debinding method. More recently, Z. Y. Liu et. al.<sup>21</sup> have manufactured 316L stainless microstructures with MIM. In the Micro MIM process, fine metal powders are mixed with a binder system into a feedstock and injected into the mold; the mold contains the microstructured mold inserts. In order to achieve good filling of the mold inserts, injection molds which can be evacuated and heated, are required along with highly fluid feedstock. Safe mold removal of the microstructures requires low mold temperatures and relatively high mechanical stability of the binder system. After metallurgical injection molding, the filling is processed further in the furnace, mostly under an oxidizing atmosphere, to remove the binder system, generating the first contact spots between the powder particles. Subsequently, in a defined atmosphere, the brown compact is sintered into a solid microstructure of close-to-theoretical density.

In some preliminary experiments, test structures were injection molded by MIM with a 260 $\mu$ m lateral width and an aspect ratio of 5. Feedstock was used which had been prepared from carbonyl iron powder with a mean particle size of 4-5 $\mu$ m plus 7% by volume of binder, all prepared in a mixer. In the more than one hundred injection molding cycles, mostly with automated machine operation, no wear phenomena were detected in the nickel mold inserts coated with gold of a thickness of approximate 500nm.

Scanning Electron Microcopy (SEM) examination of the injection molded microstructures before and after debinding and sintering showed that sometimes at the edges of the curvatures the mold was not filled completely and on the surface as well as in the center of the metal structures there still existed some pores and cracks. Therefore, optimization studies still need to be conducted for the injection molding process, binder removal and sintering, in order to achieve micro MIM of defect-free metal microstructures.

### **IV. Micro Electrical Discharge Machining (EDM)**

EDM is the process of electrically removing material from any conductive workpiece. This is achieved by applying high-frequency pulsed, AC or DC current to the workpiece through an electrode or wire, which melts or vaporizes the workpiece material. Positioned very precisely near the workpiece, the electrode never touches the workpiece but discharges its current through an insulating dielectric fluid (water or oil) across a very small gap. The spark is reported to be in the range of 8000 to 12000°C (14432 to 21632°F), and it vaporizes and melts the workpiece material. This process is used when the workpiece material is too hard, or the shape or location of the detail cannot easily be



conventionally machined. This makes many formerly difficult projects more practical, and many times it can be the only feasible way to machine a part or material <sup>22</sup>.

While EDM was introduced over fifty years ago, in recent decades, micro EDM technique has received attentions by some research groups including T. Masaki et. al. <sup>23</sup> who are some of the pioneers in conducting this research, followed by K. Takahata, et. al. <sup>24</sup> who produced high-aspect-ratio WC-Co microstructures by combining LiGA technique with micro-EDM, and G. L. Benavides, et. al. <sup>14</sup> who investigated the machining performance of the wire micro-EDM process by machining a high-aspect-ratio micro scale part into a variety of metals.

In the research conducted by K. Takahata, et. al., LiGA process (steps 1-5 in Fig. 1.5) was firstly used to fabricate an array of nickel electrodes for the micro-EDM. The electrodes were negative-type gear pattern of 200 $\mu$ m outside diameter with a structural height of 300 $\mu$ m as shown in Fig. 1.6.

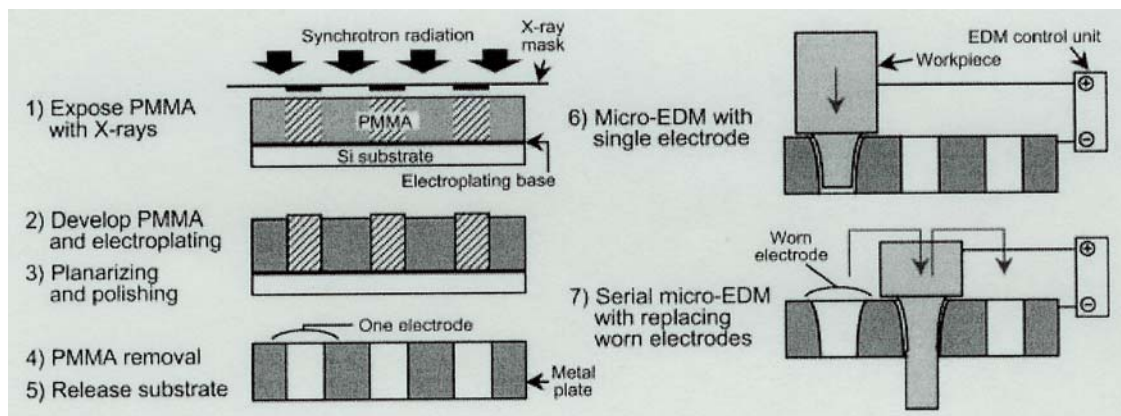


**Fig. 1.5 Flow of the fabrication process combining LiGA (1-5) and micro-EDM (step 6-7) <sup>24</sup>**

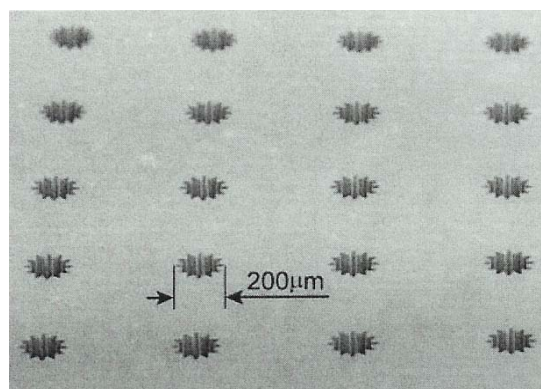


**Fig. 1.6 Array of negative-type nickel electrodes fabricated by the LiGA process <sup>24</sup>**



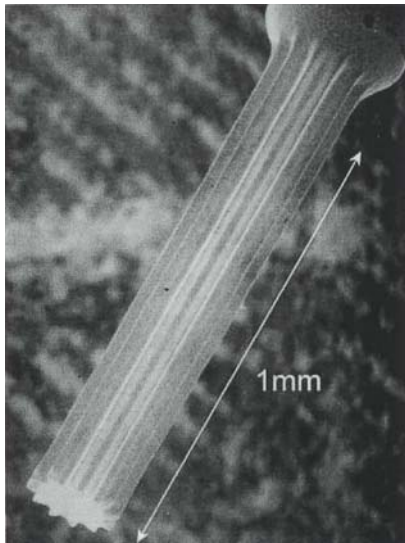


**Fig. 1.7 1mm long WC-Co microstructure with gear pattern**<sup>24</sup>

the serial micro-EDM is shown in Fig. 1.7. The variation of the outside diameter of the 1mm long structure along its length was measured to about 4 $\mu$ m.

Electrodes wear conditions were observed through SEM. The initial shape of the electrode is shown on the left side of Fig. 1.8. It is deformed by wear as shown on the right side of Fig. 1.8 when the WC-Co workpiece with a diameter of 300 $\mu$ m is fed into the electrode for about 400 $\mu$ m with discharging. Though Micro-EDM using LiGA fabricated Ni electrodes can fabricate high-aspect-ratio microstructures out of hard metal or alloy, when mass production is concerned, the electrodes wear is going to be a big issue, which needs to be handled properly.

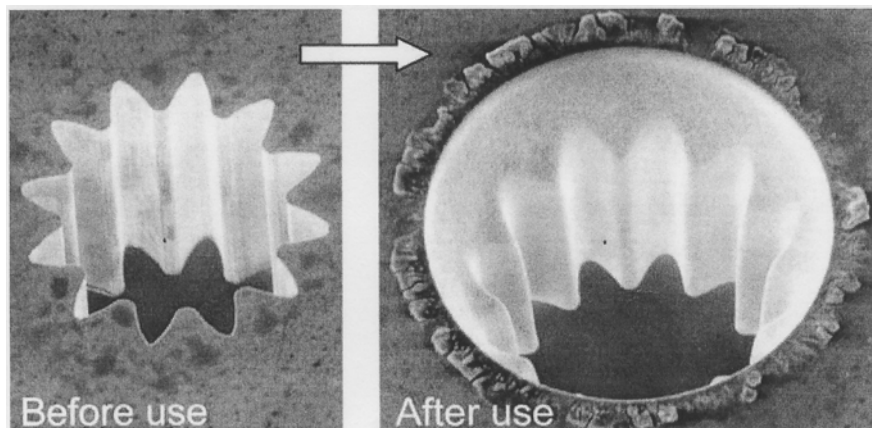


**Fig. 1.8 Initial shape of the patterned negative-type electrode and deformed one after use**<sup>24</sup>

## V. Ultraprecision Micromilling

At the macroscale, the milling process is very versatile and capable of creating three-dimensional features and structures. Adaptation of this process at the microscale (hence named micromilling) could lead to rapid and direct fabrication of micromolds and masks to aid in the development of microcomponents<sup>25 26</sup> or some other applications such as ultra-precision milling of diffraction grating on tiny parts<sup>27</sup>, micromilling millimeter long trenches in metallic alloys<sup>28</sup>, and micromilling of metallic materials<sup>29</sup>. The micromilling tools are commercially available in diameters larger than 50 $\mu\text{m}$  and custom-built tools as small as 22 $\mu\text{m}$  can be fabricated by the focused ion beam (FIB) machining process. As an example, Fig. 1.9 and Fig. 1.10 show respectively the method for fabricating micromilling tool by FIB machining and a 2-fluted micromilling tool made with FIB machining.

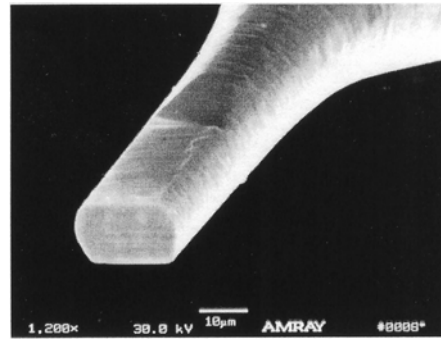
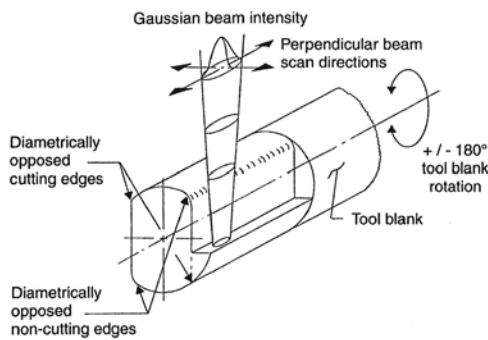


**Fig. 1.9 Method for fabricating micromilling tool by focused ion beam machining<sup>25</sup>** **Fig. 1.10 2-fluted micromilling tool made with FIB machining<sup>25</sup>**

The FIB process uses a tungsten needle which has a point radius in the submicron range. The sharp point is wetted with gallium metal which is liquid near room temperature. An extraction voltage is used to create a very intense electric field at the tip of the pointed needle. This causes field ionization of the gallium. The ejected gallium ions are then accelerated, and focused to a submicron diameter spot, and steered on to the work piece by eight-pole electrostatic field. The kinetic energy of the gallium ions causes the ejection of atoms from the workpiece in a sputtering process.

Different micromilling tools have been designed according to their specific applications. The micromilling tool shown in Fig. 1.10 uses two parallel flats fabricated as shown in Fig. 1.9. As the flat was cut with the FIB process, the intersection of the flat with the rounded tool blank exposed to the entire beam cross-section resulted in a well rounded edge. However, this edge and the flat cut acted as a knife-edge and remove one half of the Gaussian ion beam. The remaining beam continued toward the trailing edge of the face and produced a very sharp intersection at the face with the round tool blank. This sharp intersection became one of the two cutting edges. After the first flat was machined, the tool was rotated 180° and the process was repeated thus creating two sharp cutting edges which were diametrically opposed. This design does not provide any clearance behind the cutting edge and allows the rounded tool blank to burnish the walls the milled

features. Accurate placement of facets on tools and a proper stage rotation sequence between ion sputter steps can make micro-end mills of different geometries. This includes creation of well-aligned, nonplanar, cutting and too-end clearance facets.

In general, control over small feature size is made possible by computer numerically controlled (CNC) ultraprecision machines. These instruments have 5nm positional accuracy in different directions and specially designed tool holders that minimize error. CNC ultraprecision machines have been used to create microfeatures while maintaining submicron tolerance over a span of millimeters<sup>30</sup>. Trenches of several millimeters length fabricated by ultraprecision micromilling have been shown to have vertical sidewalls and small bottom surface roughness. A good matching of tool diameter to trench width is found for several tested materials including PMMA, 6061 Al, 4340 steel and brass<sup>28</sup>.

Fig. 1.11 shows one example of the machined trenches with a depth of  $\sim 62\mu\text{m}$  in PMMA by micromilling. Fig. 1.11(a) and 1.11(b) show respectively a portion of an exponential spiral pattern with stepped and straight walls and a portion of the spiral pattern with two straight walls. Measurements carried out with a WYKO Roughness/Step Tester and measurements of SEM demonstrate the ability of the process to faithfully duplicate the tool geometry into the milled trench with sharp external corners. The sharpness of the interior corner is limited by the diameter of the milling tool. The

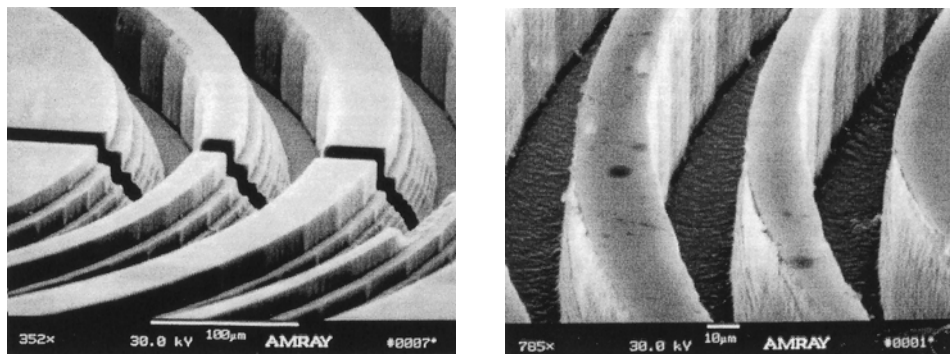


**Fig. 1.11 (a) A portion of micromilled spiral trenches with stepped and straight walls; (b) A portion of trenches with two straight walls as thin as  $8\mu\text{m}$** <sup>26</sup>

bottom the trench had a typical root-mean-square (rms) roughness of 100-130nm along the direction of the trench. The rms roughness across the width of the trench was typically less and in the range of 80-110nm. This difference is because of the feed of the tool along the trench which pushes material out in front of the bottom of the milling tool because a distinct cutting edge is not present there.

Micromilling is a very versatile technique for fabricating micro-scale feature as far as 3D microstructures is concerned, especially when complicated feature geometry is needed. Wider material range including metallic materials and metal alloys can be machined. However, there are several issues need to be stated when mass fabrication is considered. Tool wearing is one issue. The tool has strong effect on the quality of the machined parts. The progressing wearing of the cutting edge influences the geometry and the surface roughness. The relatively large cutting force causes the buckling of the micromilling tool with very small inertia. High temperature and high pressure promote

the formation of the built up edge. The failure of the cutting tool always means breakage. As a result of the wear of the cutting edge, cutting force increases continuously, which causes tool breaking. Tool wear was always asymmetrical. Consequently, one of the cutting edges machines more intensively and the other one only deforms the material or just graze it. Burr occurrence during the micromilling is another issue. Usually, burr occurrence is higher the smaller the feed velocity. In most cases the burr cannot be tolerated and must be removed or avoided in the milling process. It is almost impossible to avoid the burr occurrence. It may be minimized only by select smaller milling tools, which will create another issue. The smaller the micromilling tool is selected, the smaller the size of burrs, but the more time will be consumed for a specific project. Usually, micromilling is suitable for machining small and medium lot sizes for performing real 3D geometries.

## High Temperature Micromolding of Metals

### I. Motivation for Metal Micromolding

Microfabrication technologies are being intensely investigated for constructing devices for electrical, biochemical, and mechanical engineering applications. Fabrication of high aspect ratio microscale structures (HARMS) with the LiGA technique allows novel mechanical devices with enhanced performance, such as high-efficiency micro heat exchangers<sup>31</sup> (as shown in Fig. 1.12 (a)) and temperature controlled mechanical seals<sup>32</sup> (as shown in Fig. 1.12 (b)), to be conceptualized. Beyond device concepts, incorporation of materials suitable for the intended device application is of paramount importance for actual device realization. For example, micro heat exchangers made of high thermal conductivity/low mass density metals such as aluminum is key to realizing the higher heat transfer per unit weight resulting from the reduced device length scale.

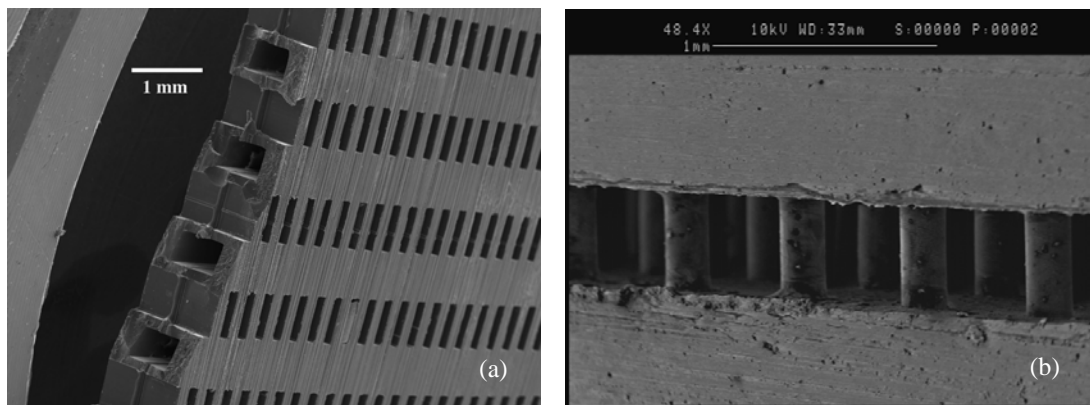


**Fig. 1.12 (a) Prototype of a cross-flow micro heat Exchanger<sup>31</sup>; (b) Prototype of temperature controlled micro seal structures<sup>32</sup>**

In the previous session, several microfabrication techniques for microscale metal structures were discussed, each with some application in a specific area with a limited material selection range. Careful observation of the processes involved in each technique

shows that electroplating of lost plastic mold, microcasting, and microinjection molding have more complicated manufacturing processes, which cause the microfabrication to be more time-consuming from the mass production point of view and sometimes higher cost. Micro EDM and micromilling are more direct machining techniques. However, with micro EDM, if wire-EDM is used to machine microparts, the process itself is time consuming; if LiGA fabricated mold used as the electrode to enhance efficiency, the electrode wear will make micro EDM process more costly, and frequently changing the electrode will cause errors in the feature geometry by misalignment. So with micromilling, efficiency, burr occurrence and surface roughness of the micromachined parts remain the issues needed to be handled. Therefore, a more direct, less time-consuming and cost-effective microfabrication technique needs to be developed for mass production of metallic microscale structures, especially negative-type structures.

To develop LiGA-like technologies into an economically viable process of mass production of high-aspect-ratio microscale metal structures, the obvious idea is to use the LiGA fabricated metal microstructure as the mold insert to directly fabricate metal structures by compression micromolding. Compression micromolding was firstly used for polymer material, usually termed hot embossing in that context. Hot embossing of polymer based materials is a well-developed technique. Plastic components for microsystems are produced economically by hot embossing. In addition, molded plastic microstructures can be used also as lost micromolds in making microstructures out of metal or ceramics. Though intensive studies have been conducted on hot embossing of plastics material by many researchers, there is a paucity of information in the literature about metal micromolding. Molding behavior such as the molding force, extraction force during demolding needs to be studied to facilitate future applications of the metal micromolding technique. So far, even with hot embossing of plastics with currently available molding instrument, extraction force during demolding remains unknown. Mechanics and tribochemistry of compression metal micromolding also need to be studied to achieve a better understanding of metal micromolding

## **II. Issues Concerning Metal Micromolding**

The process of microscale compression molding of metals, which in general occurs at higher temperatures as compared to molding polymers, requires the consideration of two issues. At the molding temperature, the yield strength of the material making up the insert bulk has to be sufficiently high to endure the stresses needed for molding. In addition, the chemical/mechanical properties of the near-surface regions of the insert must be adequate to allow repeated molding cycles without damage to the insert and the molded metal part. These issues form the challenges that the present study aims to address.

Mechanical properties of the insert bulk need to be considered, because as-electrodeposited metallic HARMs are micro-/nano- crystalline in structure and undergo significant grain growth at elevated temperatures. Yield strength of electrodeposited Ni microparts tends to decrease significantly to ~140MPa, less than 40% of the as-deposited value, when they are annealed to 400°C or higher<sup>33</sup>. With decreasing yield strengths at increasing temperatures, the choice of molding temperature needs to reflect a compromise between the requirement of sufficiently high yield strength of the insert,

which ensures no plastic deformation of the insert bulk, and the requirement of sufficiently low yield strength of the molded metal, which facilitates generation of microscale features by plastic flow without the need for excessive force. Currently, little quantitative data regarding forces required for microscale compression molding of metals exist in the literature.

During molding of a given metal, the chemical/mechanical interactions experienced by the insert depend critically on the chemical/mechanical/tribological properties of its near-surface region. If the mechanical properties of the insert bulk are sufficient, the key to successful high temperature micromolding of reactive metals is to alter the chemical/mechanical interactions between the insert and the molded metal.

### **A. Surface Engineering of the Mold Insert**

Engineering HARMS-covered surfaces by coatings must satisfy two criteria. First, the coating needs to be synthesized with desired mechanical, tribological, and chemical properties and it must adhere strongly to the surface. Second, the coating needs to cover topologically complex HARMS-covered surface in a conformal fashion. Plasma assisted vapor deposition of amorphous hydrocarbon (a-C:H) and metal-containing hydrocarbon (Me-C:H) thin films have been studied for over a decade<sup>34</sup>. The microstructure of a-C:H thin films incorporating more than a few atomic percent of carbide-forming metals, such as W or Ti, has been shown to consist of nanocrystalline metal carbide clusters embedded in an a-C:H matrix (MeC/a-C:H)<sup>35 36</sup>. In the Ti-C:H system, precipitation of nanocrystalline TiC clusters occurs at Ti compositions > 2.5 at.% Ti, and these Ti-C:H thin films are TiC/a-C:H nanocomposites<sup>37</sup>. Me-C:H thin films possess moderately high hardness, low coefficient of friction, and low wear rate<sup>38</sup>, and have been shown to be beneficial when applied to macro-scale mechanical components<sup>39</sup>. Recently, a low-pressure, high-density, inductively coupled plasma (ICP) assisted hybrid chemical/physical vapor deposition (CVD/PVD) technique has been used to deposit a-C:H and Ti-C:H thin films over a wide range of compositions<sup>40</sup>. Using Ti-C:H coating by ICP assisted hybrid CVD/PVD technique to modify the near surface properties of the mold insert, two question needs to be answered: one is whether this coating system and coating technique is suitable for conformal coating HARMS-covered surface; the other one is which coating composition will results in the desired mechanical property and tribological characteristics of the coating for molding process, meaning a need of a systematic study of the mechanical properties and tribological characteristics of Ti-C:H coatings as a function of coating composition.

### **B. Molding Behavior**

A qualitative difference in molding behavior exists depending on whether or not the insert and the molded metal have a thermodynamic driving force to mix. At present, electrodeposited Ni is the most common material choice for the insert bulk<sup>41</sup>. Regarding the chemical/mechanical interactions between the Ni insert and the molded metal, Pb and Zn (or Al) exemplify two extreme situations. In one instance, Pb and Ni are immiscible in both the solid and the liquid state<sup>42</sup>. In the other instance, Zn (or Al) and Ni have a strong driving force to form intermetallic compounds. Similarity and Differences in the molding

behavior of different metals needs to be uncovered. During molding a given metal, measurement of the molding force and extraction force is important for analyzing the molding stress. If contact stresses during micromolding exceed the yield strength of the Ni insert at the molding temperature, plastic deformation of the insert is expected, which will lead to insert deformation and loss of shape definition. Despite these concerns, little information on the required stresses for high-temperature microscale compression molding of metals and subsequent insert extraction is available in the current literature.

### **C. Mechanics of Metal Micromolding**

The metal micromolding process is a process in which the molded metal undergoes gradual but extreme plastic deformation. In order to achieve a full understanding of the metal micromolding, three issues related to the mechanics of metal micromolding need to be studied. The first one is how the deformation during molding correlates with the molding stress. The second one is how the maximum molding stress when the full molding is achieved correlates with the bulk properties (for example, the yield stress or the ultimate tensile stress) of the molded metal. The remaining one is how is the influence of the mold insert geometry on the maximum molding stress and the molded features. With these questions answered, the research can be used as guidance for future metal micromolding.

### **Summary**

Currently developed and underdeveloped microfabrication techniques, especially the techniques for manufacturing metal microstructures, have been reviewed and discussed. Each of these techniques has applications in a specific area with a limited material selection range. More importantly, a new technique of microfabrication of metal microstructures – compression molding of metals has been proposed and the related issues have been discussed in detail. Potential applications of metal micromolding have also been discussed.

### **References**

- 1 Walter Lang, Reflexions on the Future of Microsystems, Sensors and Actuators, A Physical, 72 (1999) pp. 1-15
- 2 Marc Madou, Fundamentals of Microfabrication, CRC Press LCC, (1997) pp. 2
- 3 R. A. Lawes, A. S. Holmes, and F. N. Goodall, The Formation of Moulds for 3D Microstructures Using Excimer Laser Ablation, Microsystem Technol. 3(1), (1996) pp.17-19
- 4 Jun Li and G. K. Ananthasuresh, A quality study on the excimer laser micromachining of electro-thermal-compliant micro devices, J. Micromech. Microeng., 11 (1), (2001) pp. 38-47

- 5 G. Stix, Micro Machinations: Trends in Micromechanics, Scientific American, 267(5), (1992) pp.72-80
- 6 E. W. Becker, W. Ehrfeld, P. Hagmann, A. Manner, and D. Munchmeyer, Fabrication of Microstructures with Extreme Structural Heights by Synchrotron Radiation Lithography, Galvanoforming and Plastic Moulding (LiGA Process), Microelectron. Eng., 4, (1986) pp.35-56
- 7 M. Hecke, W. Bacher, and K. D. Müller, Hot Embossing - The Molding Technique for Plastic Microstructures, Microsystem Technol., 4(3), (1998) pp.122-124
- 8 R. Ruprecht, T. Benzler, T. Hanemann, K. Müller, J. Konys, V. Piottter, G. Schanz, L. Schmidt, A. Thies, H. Wöllmer, and J. Haußelt, Various Replication Techniques for Manufacturing Three-Dimensional Metal Microstructures, Microsystem Technol., 4(1), (1997) pp. 28-31
- 9 G. Baumeister, K. Mueller, R. Ruprecht, and J. Hausselt, Production of Metallic High Aspect Ratio Microstructures by Microcasting, Microsystem Technol., 8, (2002) pp.105-108
- 10 V. Piottter, T. Benzler, T. Hanemann, H. Wöllmer, R. Ruprecht and J. Haußelt, Innovative Molding Technologies for Fabrication of Components for Microsystems. Symp Design, Test and Microfabrication of MEMS and MOEMS, Paris, France, SPIE, 3680, (1999) pp. 456-463
- 11 V. Piottter, K. Mueller, K. Plewa, R. Ruprecht, and J. Hausselt, Performance and Simulation of Thermoplastic Micro Injection Molding, Microsystem Technol., 8, (2002) pp. 387-390
- 12 K. Sawada, S. Odaka, T. Kawai, Y. Takeuchi, and T. Sata, Manufacturing of Diffraction Grating on Tiny Parts by Means of Ultraprecision Milling, Microsystem Technol., 5, (1999) pp. 157-160
- 13 K. Takahata, N. Shibaike, and H. Guckel, High-Aspect-Ratio WC-Co Microstructure Produced by the Combination of LIGA and Micro-EDM, Microsystem Technol., 6(5) (2000) pp. 175-178
- 14 G. L. Benavides, L. F. Bieg, M. P. Saavedra, and E. A. Bryce, High Aspect Ratio Meso-scale Parts Enabled by Wire Micro-EDM, Microsystem Technol., 8(6) (2002) pp.395-401
- 15 V. Piottter, T. Hanemann, R. Ruprecht, and J. Haußelt, Injection Molding And Related Techniques for Fabrication of Microstructures, Microsystem Technol., 4, (1997) pp. 129-133



- 16 A. Thies, V. Piötter, J. H. Hausselt, and O. F. Hagen, A New Method For Mass fabrication of Mettalic Microstructures, *Microsystem Technol.*, 4, (1998) pp. 110-112
- 17 V. Piötter, T. Hanemann, R. Ruprecht, and J. Haußelt, Injection Molding And Related Techniques for Fabrication of Microstructures, *Microsystem Technol.*, 4, (1997) pp. 129-133
- 18 A. Thies, V. Piötter, J. H. Hausselt, and O. F. Hagen, A New Method For Mass fabrication of Mettalic Microstructures, *Microsystem Technol.*, 4, (1998) pp. 110-112
- 19 G. Baumeister, K. Mueller, R. Ruprecht, and J. Hausselt, Production of Mettalic High Aspect Ratio Microstructures by Microcasting, *Microsystem Technol.*, 8, (2002) pp.105-108
- 20 T. Shimizu, Y. Murakoshi, T. Sano, R. Maeda, and S. Sugiyama, Fabrication of Micro-parts by High Aspect Ratio Structuring and Metal Injection Molding Using the Supercritical Debinding Method, *Microsystem Technol.*, 9, (1998) pp.90-92
- 21 Z. Y. Liu, N. H. Loh, S. B. Tor, Y. Murakoshi, R. Maeda, K. A. Khor, and T. Shimiodzu, Injection Molding of 316L Stainless Steel Microstructures, *Microsystem Technol.* 9, (2003) pp.507-510
- 22 E. Bud Guitrau, *The EDM handbook*, Hanser Gardner Publications, (1997) pp.19
- 23 T. Masaki, K. Kawata, and T. Masuzawa, Micro Electro-Discharge Maching and Its Applications, *Pro. IEEE*, (1990) pp.21-26
- 24 K. Takahata, N. Shibaike, and H. Guckel, High-Aspect-Ratio WC-Co Microstructures Produced by the Combination of LiGA and Micro-EDM, *Microsytem Technol.* 6, (2000) pp. 175-178
- 25 C. R. Friedrich and M. J. Vasile, Development of the Micromilling Process for High-Aspect-Ratio Microstructures, *J. of MEMS*, 5(1), (1996) pp.33-38
- 26 C. R. Friedrich, P. J. Coane, and M. J. Vasile, Micromilling Development and Applications for Microfabrication, *Microelectronic Engr.* 35 (1-4), (1997) pp. 367-372
- 27 K. Sawada, S. Odaka, T. Kawai, Y. Takeuchi, and T. Sata, Manufacturing of Diffraction Grating on Tiny Parts by Means of Ultraprecision Milling, *Microsystem Technol.*, 5, (1999) pp. 157-160
- 28 D. P. Adams, M. J. Vasile, G. Benavides and A. N. Campbell, Micromilling of Metal alloys with Focused Ion Beam-Fabricated tools, *Precision Engr.—J. of the Int. Soc. For Precision Engr. And Nanotechnol.*, 25 (2), (2001) pp.107-113

- 29 M. Takacs, B. Vero, and I. Meszaros, Micromilling of Metallic Materials, *J. of Materials Processing Technology*, 138(1-3), (2003) pp. 152-155
- 30 M. J. Vasile, C. R. Friedrich, B. Kikkeri, and R. McEllannon, Micrometer-scale Maching: Tool Fabrication and Initial Results, *Precision Engineering*, 19 (2/3), (1996) pp. 180-186
- 31 C. Harris, M. Despa, K. W. Kelly, Design and Fabrication of a Cross Flow Micro Heat Exchanger, *IEEE J. MEMS*. 9, (2000) pp.502-508
- 32 L. S. Stephens, K. W. Kelly, D. Kountouris, J. McLean, A pin fin microheat sink for cooling macroscale conformal surfaces under the influence of thrust and frictional forces, *IEEE J. MEMS*, 10 (2), (2001) pp. 222-231
- 33 H. S. Cho, K. J. Hemker, K. Lian, J. Goettert, G. Dirras, Measured mechanical properties of LIGA Ni structures, *Sensors and Actuators A*, 103 (1-2), (2003) pp. 59-63
- 34 C. P. Klages, R. Memming, Microstructure and Physical Properties of Metal-Containing Hydrogenated Carbon Films, *Mater. Sci. Forum* 52/53, (1990) pp. 609-644
- 35 K. Bewilogua, H. Dimigen, PREPARATION OF W-C-H COATINGS BY REACTIVE MAGNETRON SPUTTERING, *Surf. Coat. Technol.* 61 (1-3), (1993) pp. 144-150
- 36 W. J. Meng, T. J. Curtis, L. E. Rehn, P. M. Baldo, Plasma-assisted deposition and characterization of Ti-containing diamond-like carbon coatings, *J. Appl. Phys.* 83 (11), (1998) pp.6076-6081
- 37 W. J. Meng, R. C. Tittsworth, J. C. Jiang, B. Feng, D. M. Cao, K. Winkler, V. Palshin, Ti atomic bonding environment in Ti-containing hydrocarbon coatings, *J. Appl. Phys.*, 88 (5), (2000) pp.2415-2422
- 38 K. Homlberg, A. Matthews, *Coating Tribology, Properties, Techniques and Applications in Surface Engineering*, Elsevier, Amsterdam (1994)
- 39 R. Wei, P. J. Wilbur, F. M. Kustas, A ROLLING-CONTACT FATIGUE STUDY OF HARD CARBON COATED M-50 STEEL, *J. Tribology-Transactions of ASME*, 114 (2), (1992) pp. 298-303
- 40 W. J. Meng, E. I. Meletis, L. E. Rehn, P. M. Baldo, Inductively-coupled plasma assisted deposition and mechanical properties of metal-free and Ti-containing hydrocarbon coatings, *J. Appl. Phys.* 87 (6), (2000) pp. 2840-2848

- 41 W. Bacher, K. Bade, B. Matthis, M. Saumer, R. Schwarz, Fabrication of LIGA mold inserts, *Microsystem Technol.*, 4(3), (1998)pp. 117-119
- 42 T. B. Massalski (ed.), *Binary Alloy Phase Diagrams*, American Society of Metals, Metals Park, Ohio (1986)

## CHAPTER 2. FRICTION AND WEAR CHARACTERISTICS OF TITANIUM CONTAINING AMORPHOUS HYDROCARBON CERAMIC NANOCOMPOSITE COATINGS \*

### Introduction

Nanostructured materials have received intense recent scrutiny <sup>1</sup>. In addition to bulk nanostructured metals and ceramics <sup>2</sup>, nanostructured thin films and surface coatings have received much current attention <sup>3</sup>. Metal-containing hydrocarbon (Me-C:H) surface coatings have been intensely studied for over a decade <sup>4 5</sup>. Recent interests in these hydrocarbon-based coatings have been stimulated by studies showing that the contact fatigue life of mechanical components increases with these coatings applied to the component surface <sup>6</sup>. The attractiveness of Me-C:H coatings stems partly from the observation that their mechanical properties, such as the Young's modulus (E) and the hardness (H), vary systematically with coating composition, thus offering the potential of engineering a coating to suite a particular application <sup>7 8</sup>. In amorphous hydrocarbon (a-C:H) coatings incorporating significant amounts of carbide-forming metals, for example W or Ti with compositions greater than a few atomic percent, the coating microstructure has been shown to consist of nanocrystalline metal carbide clusters embedded in an a-C:H matrix. In the titanium-containing amorphous hydrocarbon (Ti-C:H) coating system, the dissolution limit of Ti atoms within the a-C:H matrix has been determined to be below 2.5 at.% Ti. Above 2.5 at.% Ti, precipitation of nanocrystalline TiC clusters occurs, and Ti-C:H coatings are TiC/a-C:H thin film nanocomposites <sup>9</sup>. For ceramic nanocomposite surface coatings, although coating microstructure and mechanical properties, such as E and H, have been studied to some detail <sup>10</sup>, little information is present in the literature about how the nanometer scaled microstructure and mechanical properties of these nanostructured ceramic coatings correlate with their macroscopic tribological characteristics. This lack of nano – macro scale correlation is a reflection of the current deficiencies in our understanding of the fundamental deformation and fracture behaviors of nanostructured ceramic thin film materials.

This chapter presents an experimental study of this correlation in the Ti-C:H coating system. The macro-scale coating friction and wear characteristics are examined by performing unlubricated sliding of Ti-C:H coatings against WC-Co balls in a ball-on-disk configuration. Consistent with previous studies, the average E and H of Ti-C:H coatings exhibit smooth and systematic variations as the Ti composition increases. In contrast, we observe jumps in the friction coefficient and wear rate of Ti-C:H coatings sliding against WC-Co over a relatively narrow Ti composition range. Our results indicate an almost binary friction and wear behavior of Ti-C:H coatings with respect to the Ti composition, a-C:H like at lower compositions and TiC like at higher compositions.

### Experimental

Deposition of Ti-C:H coatings was carried out in an ultra-high-vacuum inductively coupled plasma (ICP) assisted hybrid chemical vapor deposition (CVD)/physical vapor

---

\* Reprinted from Applied Physics Letters with the permission of AIP

deposition (PVD) tool at Louisiana State University (LSU). The base pressure of the deposition tool is  $\sim 3 \times 10^{-9}$  Torr. The hybrid CVD/PVD tool combines a radio-frequency ICP with balanced magnetron sputter sources, and can be operated in a plasma assisted CVD mode (no magnetrons) or a magnetron sputtering PVD mode (no ICP). Further details on the hybrid CVD/PVD tool and the Ti-C:H coating deposition procedures have been reported previously<sup>11 12 13</sup>. Two-inch diameter Si(100) wafers were used as substrates. The entire coating structure consisted of a sputter deposited pure Ti interlayer next to the Si substrate, followed by a Ti-C:H coatings layer. Deposition of the Ti-C:H coating layer was carried out immediately following the Ti interlayer deposition in the hybrid mode, where two magnetron sources sputter two pure Ti cathodes (99.99+%) in an Ar(99.999+%) / C<sub>2</sub>H<sub>2</sub>(99.99+%) ICP plasma. For all depositions, the total ICP input power and the input Ar/C<sub>2</sub>H<sub>2</sub> flow rate were fixed at 1000W and 10/1, respectively. The total pressure during deposition was fixed at  $\sim 1.7$  mTorr. Ti composition of the Ti-C:H coating layer was varied by varying the Ti cathode currents. For all depositions, the substrate was biased at -50V. No intentional substrate heating or cooling was applied. A series of Ti-C:H/Ti/Si specimens were deposited with increasing Ti compositions in the Ti-C:H layer and with identical nominal Ti interlayer thickness. Based on cross-sectional scanning electron microscopy (SEM) and transmission electron microscopy (TEM), the thicknesses of the Ti interlayer are  $\sim 75$  nm, and the Ti-C:H coating layer thickness ranged from 350 to 650 nm.

Coating composition was measured by combining Rutherford Backscattering Spectrometry (RBS) and hydrogen elastic recoil detection (ERD) measurements carried out at the Ion Beam Analysis Facility of the Argonne National Laboratory. Hydrogen composition measurements by ERD were checked against a previous characterized Ti-C:H specimen. TEM examination of Ti-C:H/Ti/Si specimens was carried out on a JEOL JEM 2010 microscope at the Materials Characterization Center of LSU. The microscope was operated at 200 kV. All coating specimens were examined in cross-section, details have been reported elsewhere<sup>14</sup>.

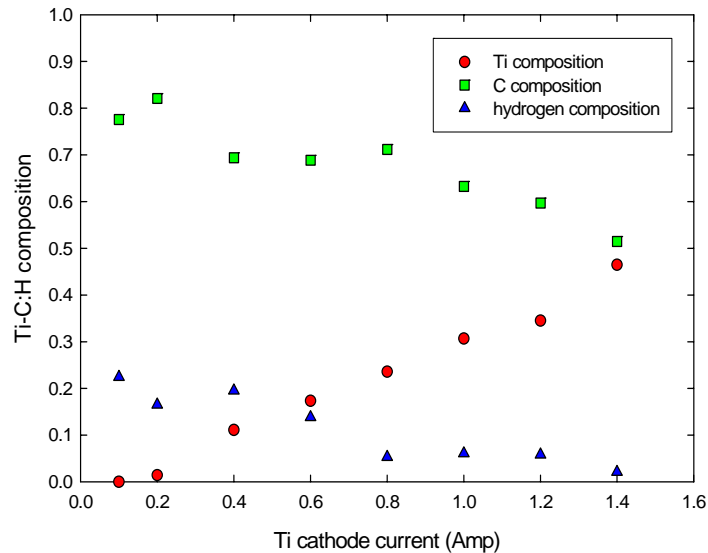
Instrumented nanoindentation was carried out on a Hysitron Triboscope interfaced to a Digital Instrument Dimension 3100 atomic force microscope (AFM). A Berkovich diamond indenter was used. The Oliver/Pharr analysis procedure was followed to extract elastic modulus and hardness from experimental load – displacement curves. Indenter area function calibration in the contact depth ( $h_c$ ) range of 20 – 225 nm was accomplished with a fused SiO<sub>2</sub> standard, assuming contact depth independent modulus<sup>15</sup>. The indenter contact area at  $h_c \sim 100$  nm was  $\sim 3 \times 10^5$  nm<sup>2</sup> according to the indenter shape function calibration. Indentation of Ti-C:H/Ti/Si specimens was carried out as a function of load, and multiple indentations at each load were performed. The values of the indentation modulus  $E_{ind} = E/(1-\nu^2)$ , where  $\nu$  is the Poisson's ratio, and  $H$  measured at  $h_c < 60$  nm were taken as being representative of the average mechanical properties of the Ti-C:H coating layer. In addition to nanoindentation measurements, the coupling of the indentation transducer to the atomic force microscope (AFM) allows surface profiles to be examined quantitatively in the contact AFM mode with the Berkovich indenter tip.

Friction and wear characteristics of Ti-C:H coatings were characterized by ball-on-disc testing on a CETR UMT-2 universal micro-tribometer. Unlubricated sliding tests were carried out at room temperature in air, where the relative humidity was  $40 \pm 20\%$ . Commercial WC-Co balls, 4 mm in diameter, were used for the tests. A normal load of

1N was used for all tests, with an estimated nominal Hertzian contact pressure of  $\sim 1$  GPa<sup>16</sup>. Linear sliding velocity between the WC-Co ball and the coating ranged between 6 – 8 m/min. Ball-on-disk testing of Ti-C:H/Ti/Si specimens was accomplished by gluing the backside of the Si substrate to a steel disk before testing. Coatings were tested for a minimum of 20 min. Profile of the wear track generated by the sliding WC-Co ball on the coating was measured after testing on a Tencor  $\alpha 500$  stylus profilometer. Integrated area of the wear track was computed from the wear track profile, from which the wear volume was obtained. The average wear rate of the coating was taken as the total wear volume divided by the product of the ball normal load and total distance traveled<sup>17</sup>.

## Results and Discussion

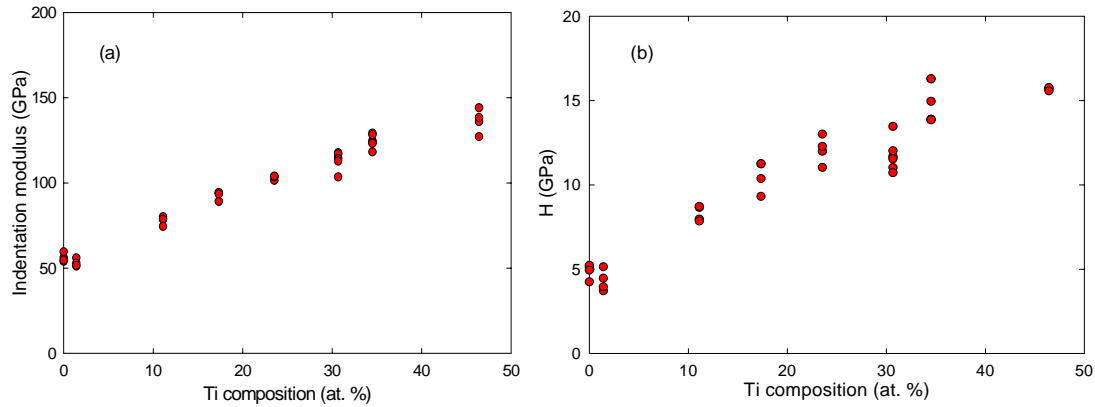
Fig. 2.1 shows average compositions in atomic number fractions of the Ti-C:H coating layers of the series of Ti-C:H/Ti/Si(100) specimens as a function of Ti cathode current. Ti, C, and hydrogen compositions were determined by combining RBS results, which yield the C to Ti ratio, and ERD results, which yield the hydrogen fraction with respect to the standard Ti-C:H specimen with known hydrogen content. The Ti composition in the Ti-C:H coating layer increases approximately linearly with the Ti cathode current. At the low Ti cathode current of 0.1 Amp, the Ti composition in the Ti-C:H coating layer is below the RBS detection limit and the coating is approximately pure a-C:H. In this case, the hydrogen to carbon ratio is  $\sim 0.29$ , consistent with previous studies on a-C:H thin films [ref. 13]. As the Ti composition in the Ti-C:H coating layer increases, the hydrogen composition decreases. At the highest Ti composition of 46.4 at. %, the hydrogen composition is only 2.2 at. %. Previous small angle X-ray scattering (SAXS) and high-resolution TEM characterization of Ti-C:H coatings showed that the volume fraction of nanocrystalline TiC clusters embedded in the a-C:H matrix increases



**Fig. 2.1 Composition of a series of Ti-C:H coatings deposited by ICP assisted hybrid CVD/PVD as a function of the Ti cathode current. For all depositions, the two Ti cathodes were operated at equal currents**

as the Ti composition increases, and suggests that the TiC clusters do not incorporate hydrogen<sup>18</sup>. Hydrogen inclusion into the Ti-C:H coatings therefore occurs through incorporation into the a-C:H matrix. As the TiC volume fraction increases, the overall hydrogen composition is thus expected to decrease. The observed decrease in the average hydrogen composition as the Ti composition increases, as shown in Figure 2.1, is consistent with this picture.

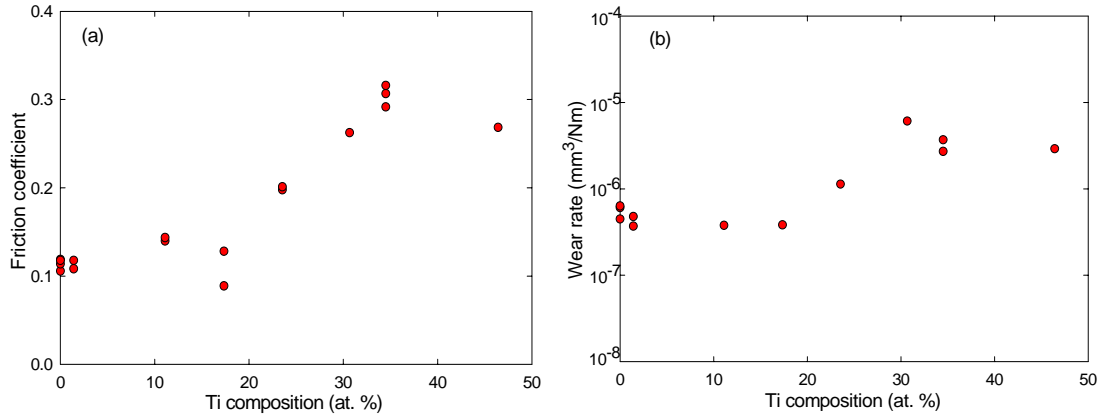
Fig. 2.2(a) and (b) show respectively  $E_{ind}$  and  $H$  of the series of Ti-C:H coatings as a function of the Ti composition. As the Ti composition increases from ~ 0 at. % to > 45 at. %, both  $E_{ind}$  and  $H$  show a systematic variation with Ti composition, increasing from ~ 50 GPa and ~ 5 GPa to ~ 140 GPa and ~ 15 GPa, respectively. Over the entire range of Ti compositions, the hardness to modulus ratio  $H/E_{ind}$  is approximately a constant ~ 0.1. These experimental observations are consistent with previous studies of the Ti-C:H coating system, and show a smooth variation of the modulus and hardness of TiC/a-C:H nanocomposites as a function of the Ti composition despite their microstructure with three dimensional compositional and structural modulations on the nanometer scale.



**Fig. 2.2 Average (a) indentation modulus  $E/(1-\nu^2)$ , and (b) hardness  $H$ , of the series of Ti-C:H coatings as a function of the Ti composition. Data points at the same Ti composition denote repeat measurements on the same specimen**

Fig. 2.3(a) shows unlubricated friction coefficients of the series of Ti-C:H coatings sliding against WC-Co as a function of the Ti composition. All friction coefficients reported are the average values over a twenty minute testing period. Data points at the same Ti composition represent a different sliding test with the same Ti-C:H coating/WC-Co ball pair. Each sliding test was conducted with a pristine spot on the WC-Co ball and an as-deposited area on the Ti-C:H coating. At Ti compositions below 20 at. %, the friction coefficients stayed relatively constant ~ 0.1. This low friction coefficient is characteristic of hard carbon based coating materials. At Ti compositions above 30 at. %, the friction coefficients are again relatively constant, and ranged between 0.25 and 0.3. A friction coefficient in this range is typical for unlubricated sliding between ceramic materials such as carbides and nitrides<sup>19</sup>. In contrast to Figure 2.2, which shows smooth variations of  $E_{ind}$  and  $H$  as a function of the Ti composition, Figure 2.3 shows that the friction behavior of the Ti-C:H coatings as a function of the Ti composition exhibits an

approximately constant low friction region and an approximately constant higher friction region, with a relatively sharp transition from the lower friction behavior to the higher friction behavior occurring within the Ti composition range of 20 to 30 at. %.



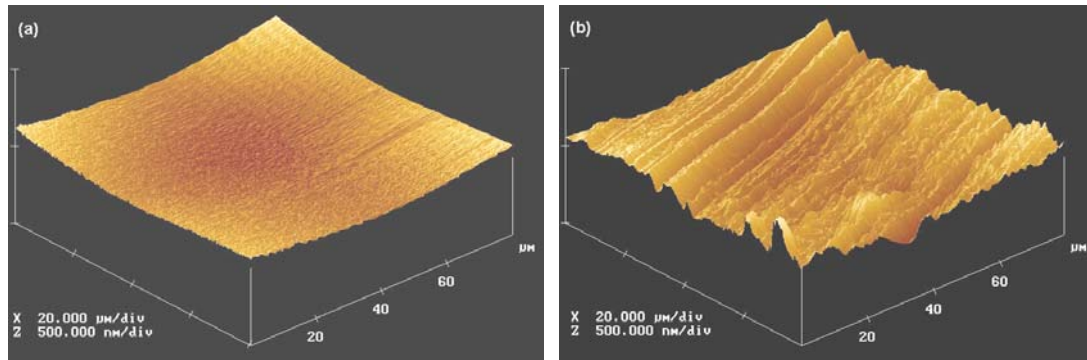
**Fig. 2.3 Average friction coefficient (a) and wear rate (b) of the series of Ti-C:H coatings during unlubricated sliding against WC-Co as a function of the Ti composition. Data points at the same Ti composition denote results of separate sliding tests with the same coating/ball pair**

Fig. 2.3(b) shows average wear rates of the series of Ti-C:H coatings sliding against WC-Co as a function of the Ti composition. Data points at the same Ti composition represent a different sliding test with the same Ti-C:H coating/WC-Co ball pair, using a pristine spot on the WC-Co ball and an as-deposited area on the Ti-C:H coating. At Ti compositions below 20 at. %, the coating wear rates stayed relatively constant,  $\sim 5 \times 10^{-7}$  mm<sup>3</sup>/Nm. These observed wear rates are typical for Me-C:H coatings<sup>20</sup>. At Ti compositions above 30 at. %, the coating wear rates are again relatively constant,  $\sim 4 \times 10^{-6}$  mm<sup>3</sup>/Nm, exhibiting however an order of magnitude increase in wear as compared to coatings with lower Ti composition. The average coating wear rate mimics the behavior of the friction coefficient, exhibiting an approximately constant low wear region and an approximately constant higher wear region, with a relatively sharp transition from the lower wear behavior to the higher wear behavior occurring within the Ti composition range of 20 to 30 at. %.

Figures 2.2 and 2.3(b) show that the wear rate of Ti-C:H coatings exhibits a pronounced increase as the Ti composition increases from 20 to over 30 at. %, even though the coating hardness increases from  $\sim 10$  GPa to  $\sim 15$  GPa in the same composition range. These observations are in contradiction to the well known Archard wear equation, which states that the wear rate should be inversely proportional to the hardness of the softer surface of the contacting pair, in this case that of the Ti-C:H coating [ref. 19]. Differences in the wear track profiles of the Ti-C:H coatings were noticed during stylus profilometry measurements. Wear tracks of the Ti-C:H coatings exhibiting low wear were smooth, whereas those of the Ti-C:H coatings exhibiting higher wear possessed sharp spikes within the wear track.



Fig. 2.4(a) and 4(b) show two AFM images obtained from within the wear tracks of two Ti-C:H specimens. The Ti compositions of the two Ti-C:H specimens are 1.42 and 34.5 at.%, respectively. Shown clearly in Figure 4, the wear track of the lower Ti composition coating, with an average wear rate of  $\sim 4.2 \times 10^{-7} \text{ mm}^3/\text{Nm}$ , is very smooth. In contrast, the wear track of the higher Ti composition coating, with an average wear rate of  $\sim 3.2 \times 10^{-6} \text{ mm}^3/\text{Nm}$ , contains numerous micrometer and sub-micrometer scaled facets and micrometer scaled trenches. Additional experiments showed smooth wear tracks for the low wear coatings and rough wear tracks for the higher wear coatings.



**Fig. 2.4** Contact AFM images obtained within two wear tracks on two Ti-C:H coatings due to unlubricated sliding against WC-Co balls. The Ti compositions of the Ti-C:H coatings are (a) 1.42 at. %, (b) 34.5 at. %, respectively

Observations shown in Figure 2.4 and similar ones strongly suggest that wear of Ti-C:H coatings as the Ti composition varies involves different mechanisms, and that one wear mechanism operates predominantly in the low friction/low wear region with Ti composition  $< 20$  at. % and another operates predominantly in the higher friction/higher wear region with Ti composition  $> 30$  at. %. Previous friction and wear studies on hard hydrocarbon based coatings generally show that the low friction/low wear behavior is related to the formation of a graphitic layer in the wear track, which provides a form of self-lubrication during sliding<sup>21</sup>. The presently measured friction coefficients and wear rates of Ti-C:H coatings with Ti compositions  $< 20$  at. % are consistent with numerous previous measurements on Me-C:H coatings [ref. 20]. In contrast, the observed wear track morphology of Ti-C:H coatings with Ti compositions  $> 30$  at. % suggests that wear of these coatings involves micrometer and/or nanometer scale coating fracture, which is absent in the low friction/low wear region. The increased coating wear as the Ti composition increases is therefore the result of a different wear mechanism operating as the nanocrystalline TiC cluster fraction increases.

The evolution of the size of nanocrystalline TiC clusters contained within Ti-C:H coatings have been studied by SAXS [ref. 18]. At Ti compositions  $< 15$  at. %, TiC clusters exhibit a monomodal size distribution, with mean cluster size  $\sim 2$  nm. At Ti compositions  $> 18$  at. %, the TiC cluster size evolves into a bimodal distribution, with smaller and larger sized clusters present simultaneously. The smaller TiC cluster size is approximately constant  $\sim 2$  nm, independent of the Ti composition. The larger TiC

clusters are  $\sim 7$  nm in size at Ti compositions of  $> 20$  at. %, and grow in volume fraction as the Ti composition increases. At Ti composition  $\sim 20$  at. %, the total TiC cluster volume fraction is  $\sim 30$  %. It is believed that the development of larger sized TiC clusters at higher Ti compositions is due to coalescence of uniform TiC clusters,  $\sim 2$  nm in size, as the TiC cluster nucleation density increases with increasing Ti composition. At higher TiC cluster volume fractions, larger TiC clusters develop as an increasing number of smaller-sized clusters coalesce together. Cross-sectional high-resolution TEM examination of the Ti-C:H coating with a Ti composition of 46.4 at. % showed that the entire coating layer consists of TiC grains, with little sign of the presence of a-C:H. The current situation is reminiscent of the site percolation model, in which very large clusters develop as the fraction of filled sites increases toward the percolation threshold<sup>22</sup>. Our data suggest that, as the TiC cluster volume fraction increases and larger TiC clusters develop, the Ti-C:H coating wear mechanism goes from the self-lubricated wear characteristic of hard carbon based materials to micrometer/nanometer scale fracture. According to the present data, this mechanism remains operative as the TiC volume fraction approaches 1.

As the Ti composition increases above 20 at. %, Figures 2.3(a) and 2.3(b) show a concomitant increase in the friction coefficient and the wear rate. At Ti compositions above 30 at. %, the macroscopic friction and wear characteristics of Ti-C:H coatings appear to be TiC like. It is intriguing to contemplate the true contact conditions during sliding. As the Ti composition increases, the average TiC cluster size may increase such that, within each micro-asperity contact area, WC-Co is “effectively” contacting TiC. The detailed conditions dictating each micro-asperity contact to be “a-C:H like” or “TiC like” remains to be clarified. As the nanoindentation technique becomes better understood, the average modulus and hardness of nanostructured ceramic coatings are measured with increasing confidence. However, the coating fracture behavior is at present rarely studied, especially in relation to coating structure and composition<sup>23</sup>. The present data suggest that the fracture behavior of nanocomposite coatings, in addition to their modulus and hardness, needs to be examined in order to better understand the macroscopic friction and wear characteristics of nanostructured ceramic coatings.

## Conclusion

In summary, we have performed a detailed examination of the macroscopic friction and wear characteristics of TiC/a-C:H nanocomposite coatings as a function of the Ti composition. Our results indicate an almost binary friction and wear characteristics of TiC/a-C:H nanocomposites with respect to the Ti composition, a-C:H like at Ti compositions  $< 20$  at. %, TiC like at Ti compositions  $> 30$  at. %. Our data suggest that the coating wear mechanism changes to one involving micro/nano scale fracture as the TiC cluster volume fraction increases.

## References

- 1 A. S. Edelstein, R. C. Cammarata (eds.), *Nanomaterials: Synthesis, Properties, and Applications*, Institute of Physics Publishing, Bristol (1996)

- 2 R. W. Siegel, Nanostructures of metals and ceramics, in *Nanomaterials: Synthesis, Properties, and Applications*, edited by A. S. Edelstein and R. C. Cammarata, Institute of Physics Publishing, Bristol (1996)
- 3 See, for example, contributions to the 27<sup>th</sup> International Conference on Metallurgical Coatings and Thin Films, edited by B. D. Sartwell, C. Mitterer, K. J. Wahl, A. Pique, *Surf. Coat. Technol.* 133/134 (2000)
- 4 C. P. Klages, R. Memming, Microstructure and physical properties of metal-containing hydrogenated carbon films, *Mater. Sci. Forum* 52/53, (1990) pp. 609-644
- 5 K. Bewilogua, H. Dimigen, Preparation of W-C:H coatings by reactive magnetron sputtering, *Surf. Coat. Technol.* 61(1-3), (1993) pp. 144-150
- 6 R. Wei, P. J. Wilbur, F. M. Kustas, A rolling contact fatigue study of hard carbon coated M-50 steel, *J. Tribology-Transactions of ASME*, 114(2), (1992) pp. 298-303
- 7 W. J. Meng, T. J. Curtis, L. E. Rehn, P. M. Baldo, Plasma-assisted deposition and characterization of Ti-containing diamond-like carbon coatings, *J. Appl. Phys.* 83 (11), (1998) pp.6076-6081
- 8 W. J. Meng, B. A. Gillispie, Mechanical properties of Ti-containing and W-containing diamond-like carbon coatings, *J. Appl. Phys.* 84 (8), (1998) pp. 4314-4321
- 9 W. J. Meng, R. C. Tittsworth, J. C. Jiang, B. Feng, D. M. Cao, K. Winkler, V. Palshin, Ti atomic bonding environment in Ti-containing hydrocarbon coatings, *J. Appl. Phys.*, 88 (5), (2000) pp.2415-2422
- 10 W. J. Meng, R. C. Tittsworth, L. E. Rehn, Mechanical properties and microstructure of TiC/amorphous hydrocarbon nanocomposite coatings, *Thin Solid Films* 377/378, (2000) pp. 222-232
- 11 W. J. Meng, T. J. Curtis, Inductively coupled plasma assisted physical vapor deposition of titanium nitride coatings, *J. Electronic Materials*, 26 (11), (1997) pp. 1297-1302
- 12 W. J. Meng, T. J. Curtis, L. E. Rehn, P. M. Baldo, Temperature dependence of inductively coupled plasma assisted deposition of titanium nitride coatings, *Surf. Coat. Technol.* 120/121, (1999) pp. 206-212
- 13 W. J. Meng, E. I. Meletis, L. E. Rehn, P. M. Baldo, Inductively-coupled plasma assisted deposition and mechanical properties of metal-free and Ti-containing hydrocarbon coatings, *J. Appl. Phys.* 87 (6), (2000) pp. 2840-2848

- 14 D. M. Cao, J. C. Jiang, B. Feng, W. J. Meng, Microstructure of TiC/amorphous hydrocarbon nanocomposite coatings, *Microscopy and Microanalysis* 6 (Supplement 2), 440, Microscopy Society of America (2000)
- 15 W. C. Oliver, G. M. Pharr, An improved technique for determining hardness and elastic modulus using load and displacement sensing indentation experiments, *J. Mater. Res.* 7(6), (1992) pp. 1564-1583
- 16 K. L. Johnson, *Contact Mechanics*, Cambridge University Press, Cambridge (1985)
- 17 S. J. Harris, A. M. Weiner, W. J. Meng, Tribology of metal-containing diamond-like carbon coatings, *Wear*, 211(2), (1997) pp. 208-217
- 18 D. E. Alexander, D. M. Cao, W. J. Meng, J. C. Jiang, S. Seifert, G. L. Doll, Microstructural characterization of titanium carbide/amorphous hydrocarbon nanocomposite coatings by small angle X-ray scattering and transmission electron microscopy, D.M.Cao M.S Thesis, Louisiana State University, Mechanical Engineering Department, (2001)
- 19 I. M. Hutchings, *Tribology: Friction and Wear of Engineering Materials*, CRC Press, Boca Raton (1992)
- 20 K. Homlberg, A. Matthews, *Coating Tribology, Properties, Techniques and Applications in Surface Engineering*, Elsevier, Amsterdam (1994)
- 21 R. Wei, P. J. Wilbur, M. J. Liston, G. Lux, Rolling contact fatigue wear characteristics of diamond-like hydrocarbon coatings on steel, *Wear* 162/164 (A), (1993) pp. 558-568
- 22 R. Zallen, *The physics of amorphous solids*, Wiley, New York (1983); for the simple cubic lattice, the site percolation threshold is 31 %
- 23 J. S. Wang, Y. Sugimura, A. G. Evans, W. K. Tredway, The mechanical performance of DLC films on steel substrates, *Thin Solid Films* 325(1/2), (1998) pp. 163-174

## CHAPTER 3. TRIBOLOGICAL CHARACTERIZATION OF Ti-C:H COATINGS BY RAMAN SPECTROSCOPY AND ATOMIC FORCE MICROSCOPY

### Introduction

Metal free amorphous hydrocarbon (a-C:H) coatings have been extensively studied over the past several decades due to their unique combination of mechanical properties and tribological behavior such as high hardness and elastic modulus, excellent wear resistance and low coefficient of friction as well as other properties such as chemical inertness and high electrical resistivity. At present, metal-containing hydrocarbon (Me-C:H) coatings are receiving attention owing partly to their better adhesion to metallic substrates<sup>1</sup> as well as the potential to tune coating properties through changes in metal composition. Deposition and mechanical properties such as hardness and Young's modulus of Me-C:H coatings have been studied to some detail<sup>2,3,4,5</sup>. Preliminary results on the friction and wear characteristics of Ti-C:H coatings have also been reported in our previous study<sup>6</sup>. By depositing Ti-C:H coatings on silicon substrates in an inductively coupled plasma assisted hybrid chemical/physical vapor deposition (CVD/PVD) system, the microstructure of Ti-C:H coating has been shown to change as a function of Ti composition. At Ti compositions greater than 2.5 at. %, the microstructure consists of TiC clusters embedded in an a-C:H matrix and the average cluster size increases with increasing Ti composition. At Ti compositions below 2.5 at. %, the entire structure is amorphous. The Young's modulus (E) and hardness (H) of Ti-C:H coatings exhibit smooth variations as the Ti composition increases. During unlubricated sliding of Ti-C:H coating against WC-Co balls, both the friction coefficient and coating wear rate exhibit a relatively abrupt transition over a relatively narrow Ti composition range, indicating bimodal friction and wear behaviors for the Ti-C:H coatings: a-C:H like at Ti compositions below 20 at. % and TiC like at Ti compositions above 30 at. %. According to the previous studies performed by Wei, et al.<sup>7</sup>, Liu et al.<sup>8</sup>, and Varma et al.<sup>9</sup>, the low friction/low wear behavior of hard hydrocarbon based coatings is believed to be related to the formation of a graphite-like layer in the wear track, which serves as a lubricant during sliding. However, detailed information about the formation of the graphite-like layer and its influences on the friction and wear behavior of Ti-C:H remains to be explored. Although the surface morphology of the coating wear track was examined in the previous study, question like how the surface morphology of the coating and the counterpart evolves so as to influence the friction and wear behavior during sliding was not addressed.

This chapter aims to provide some explanation about the bimodal friction and wear behavior of Ti-C:H coatings by presenting an experimental study of the graphitization phenomena during sliding against steel balls in an unlubricated condition by Raman Spectroscopy and atomic force microscopy (AFM) examinations of coating surface morphology, wear tracks, and wear scars on the counterparts.

### Experimental

The coatings studied in this article were prepared in an Inductively-Coupled-Plasma (ICP) assisted hybrid CVD/ PVD system<sup>10</sup>, further details can be found somewhere<sup>11,12</sup>.

Base pressure for all depositions was around  $2.0 \times 10^{-8}$  Torr. Substrates used for the coatings are 2-inch diameter 52100 steel coupons, polished with silicon carbide abrasive papers and polycrystalline diamond suspensions down to  $1 \mu\text{m}$ . Deposition procedure for each coating began with a 5 min etching in an inductively coupled Ar plasma with an input power of 1000W and a substrate bias voltage of  $-100\text{V}$ . Ar flow rate was fixed at 50 sccm. Pressure in the chamber was about 1.7 mTorr. Then a Ti interlayer was deposited for 15 minutes under the same pressure with the ICP turned off and the substrate biased to  $-50\text{V}$ . Deposition of Ti/a-C:H coating was carried out in an Ar/C<sub>2</sub>H<sub>2</sub> mixture right after the interlayer deposition. During deposition, ICP input power was kept at 1000W, substrate bias voltage  $-50\text{V}$  and ratio of Ar to C<sub>2</sub>H<sub>2</sub> fixed at 10:1. Ti composition in the coatings was varied through changing the Ti gun current from 0.2A to 1.4A. Detailed information on the deposition condition for Ti-C:H coating of each specimen was tabulated in table 3.1. Composition variation of Ti/a-C:H coatings as a function of Ti cathode current is shown in Fig. 3.1<sup>13</sup>.

**Table 3.1. Deposition Condition for Ti-C:H Coatings**

Specimen	Ti Cathode Current (A)	Ar Flow Rate (sccm)	C2H2 Flow Rate (sccm)	Substrate Bias Voltage (V)	Ti-C:H Deposition Time (min)
w11301	0.2	50	5	-50	25
w11101	0.3	50	5	-50	25
w10701	0.4	50	5	-50	25
w10901	0.6	50	5	-50	25
w10601	0.8	50	5	-50	25
w10801	1.0	50	5	-50	25
w11201	1.3	50	5	-50	25
w11001	1.4	50	5	-50	25

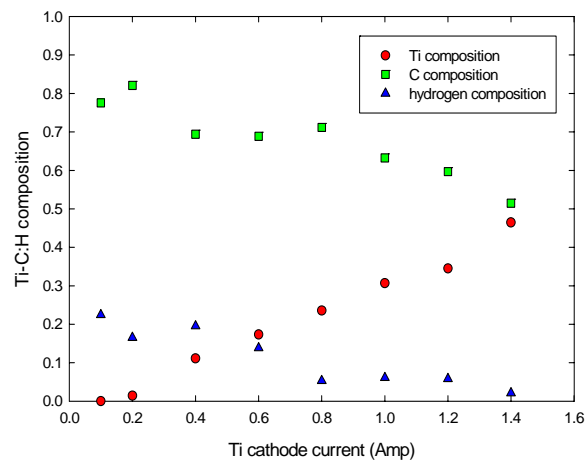


**Fig. 3.1 Composition of a series of Ti-C:H coatings deposited by ICP assisted hybrid CVD/PVD as a function of the Ti cathode current. For all depositions, the two Ti cathodes were operated at equal currents<sup>13</sup>**

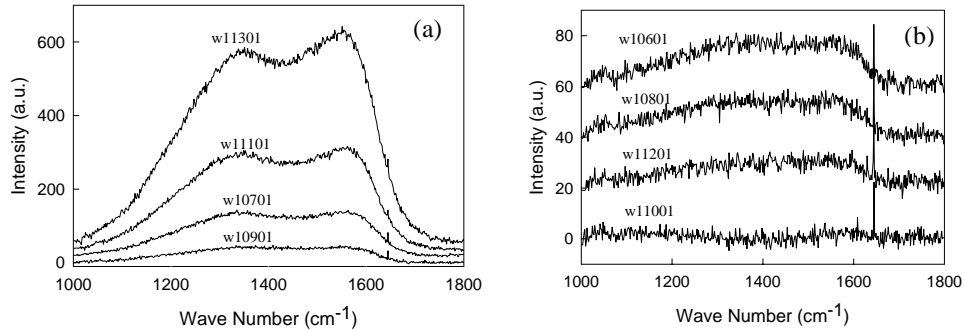
The Raman Scattering measurements were carried out on a Micro Raman Instrument with a He-Ne laser supplying the excitation wavelength of 628.5nm and focused to a spot of 20 $\mu$ m in diameter. The laser power was 20 mW. To avoid laser heating effects, a filter was used during spectra collection to reduce the laser power to 2mW. Two operating modes were used in the measurements, one of which is 600grat/mm with a lower spectral resolution and wider spectral range from 250 to 2500  $\text{cm}^{-1}$ ; the other of which was 1800 grat/mm with a higher resolution but a narrower spectral range from 1000 to 1800  $\text{cm}^{-1}$ . Spectra collected from the former mode were intended to observe the slope changes of different spectra and those from the latter mode were used to facilitate peak fitting.

Wear testing on the coatings was carried out in a ball-on-disk configuration with a CSEM High Temperature Tribometer. Counter parts used for the wear testing were 52100 steel balls with a diameter of 4mm and surface roughness of about 62nm. All wear testing were performed in air with a relative humidity of 25% and at an ambient temperature of 20°C under unlubricated conditions. Normal load was fixed at 2N and sliding speed was 20cm/min. Sliding distance varied from 0.6m to 10,050m depending on the intended information needed in the study. The images of the steel balls before and after wear testing were observed through an optical microscope and recorded with a CCD camera. Diameters of the wear scars on the balls were measured through a computerized translation stage to an accuracy of 5 $\mu$ m.

The AFM measurements were performed with a commercial microscope (Quesant Instrument Qscope<sup>TM</sup> 788).

## Results and Discussion

Fig. 3.2 (a) and (b) shows the evolution of the Raman spectra of the as-deposited coatings versus Ti cathode current. The intensity of the Raman features changes as a function of Ti cathode current and decreases as Ti cathode current increases from 0.2 A to 1.4A. The strongest scattering was observed from the specimen with the lowest Ti composition. The Raman spectrum of the specimen with the highest Ti composition is essentially featureless. To understand the Raman spectral features, a fitting procedure based on deconvolution of the experimental spectra by Gaussian curves, including background subtraction by means of a polynomial adjustment was utilized. To obtain a good fit, it was necessary to use four Gaussians instead of two.



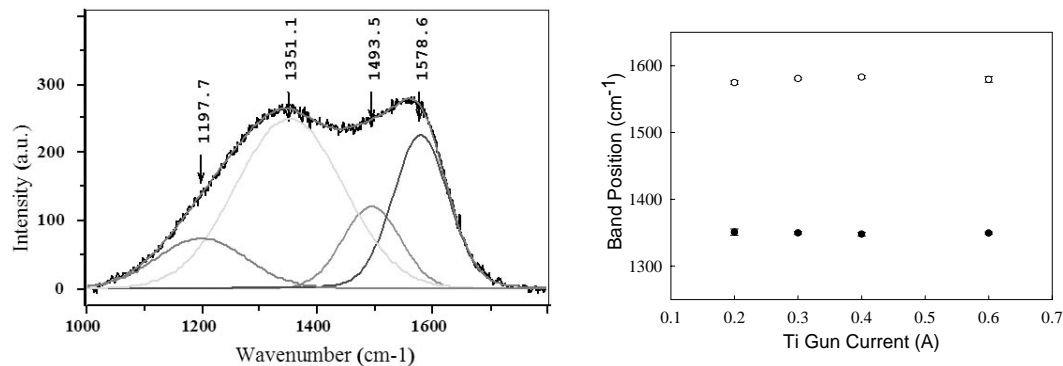
**Fig. 3.2 Evolution of Raman spectra of the as-deposited coatings**

Fig. 3.3 shows the result of typical fitting of the raw Raman spectra. The interpretation of the fitted Raman features according to previous studies is shown in table 3.2. Two dominant peaks centered at  $1350\text{ cm}^{-1}$  and  $1580\text{ cm}^{-1}$  respectively were observed from the as deposited coatings with lower Ti compositions (Fig. 3.2(a)). These are the commonly observed D and G peaks of disordered carbon.

**Table 3.2 Interpretation of the observed Raman features** <sup>14</sup>

Raman Feature ( $\text{cm}^{-1}$ )	Possible Interpretation
1180	Nanocrystalline diamond, hexagonal diamond, or $\text{sp}^3$ -rich phase
1305	Hexagonal diamond
1332	Cubic diamond
1350	D peak of nanocrystalline graphite or disordered carbon containing aromatic ring structures, related to the “breathing” motion of carbon atoms or condensed benzene rings
1490	Semicircle ring stretch vibration of condensed benzene rings or in the
1575	G peak of graphite, nanocrystalline graphite, or disordered carbon, related to stretching vibration of $\text{sp}^2$ coordinated carbon

Fig. 3.4 shows the positions of the dominant Raman peaks from the as-deposited coatings with lower Ti compositions. The existence of the D-peak is related to the existence of aromatic carbon rings within the amorphous hydrocarbon matrix. The presence of the G-peak arises from the stretch vibrations of  $\text{sp}^2$  bonded carbon <sup>15</sup>.



**Fig. 3.3 Results of typical fitting of Raman spectra. The spectra is from the Ti-C:H coating deposited at the Ti cathode current of 0.3A**

**Fig. 3.4 Fitting results of the dominant Raman peak positions from the as-deposited coatings with lower Ti compositions**

Similarities and differences between the Raman spectra collected from the coatings and from the corresponding balls used in wear testing are demonstrated in Fig. 3.5. Figure 3.5 (a) is representative of typical Raman spectra from coatings deposited at lower Ti cathode currents. Spectrum b is collected from the as-deposited coating deposited at a Ti cathode current of 0.3A. Spectrum c shows typical Raman features collected from the film layer formed inside one wear track after a sliding test to a distance of about 880m. Curves a and d show respectively two typical Raman spectra of wear scar debris at



different locations on the corresponding ball used in the sliding test. The observed Raman features in all four spectra are typical of a-C:H<sup>16</sup>.

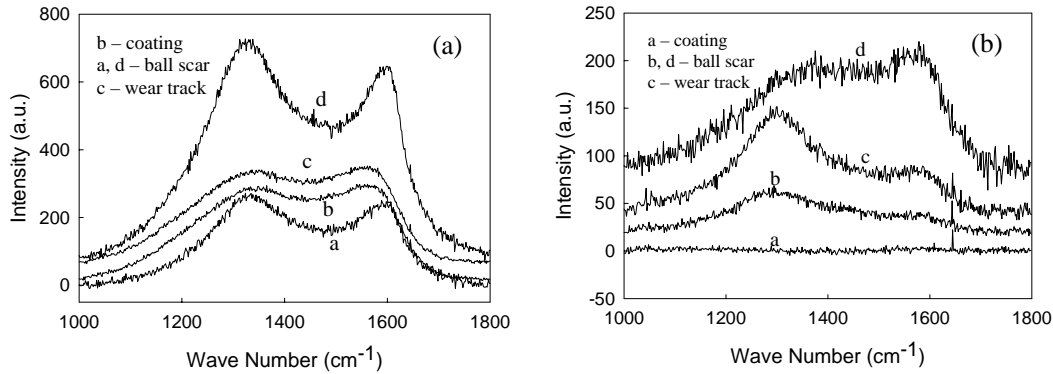


**Fig. 3.5 Raman scattering spectra collected from as-deposited coatings, inside of wear tracks, and on the surfaces of worn balls: Ti-C:H coating deposited with a Ti cathode current of 0.3A (a) and 1.0A (b)**

Figure 3.5(b) shows an analogous set of Raman spectra related to coatings deposited at higher Ti cathode currents. Spectrum a is collected from the as-deposited coating deposited at a Ti cathode current of 1.0A. Spectrum c shows typical Raman features collected from the film layer formed inside one wear track after a sliding test to the same distance of about 880m. Curves b and d show respectively two typical Raman spectra collected from wear scar debris at different locations on the corresponding ball used in the sliding test. Spectrum a shows that the a-C:H Raman signature is absent in the as-deposited coating, consistent with the coating being predominantly B1-TiC, which is first-order Raman inactive due to its centrosymmetric crystal structure<sup>17</sup>. The presence of the a-C:H like Raman signature in traces c, a and d in Fig. 3.5(a) and traces c, b and d in Fig. 3.5(b) indicates that disordered carbonaceous materials develop within the wear track after prolonged sliding contact with the steel ball and that some of the material transferred to the steel balls during continuous sliding. This transferred material may contribute to decreasing the observed friction coefficient. The increased sharpness of the D and G peaks in spectra a and d of Fig. 3.5 (a) may reflect a decrease in bond disorder and an increased dominance of short and medium range graphitic order in the transfer materials on the ball as compared with the as deposited coating<sup>18</sup>.

To better understand the friction and wear behavior of Ti-C:H coating, Raman spectra were collected from several spots inside the wear tracks of a series of coatings deposited at Ti cathode currents ranging from 0.2A to 1.4A, and from the wear scars on the corresponding steel balls used in the sliding tests. All the sliding tests were conducted under the same conditions, with a sliding speed of about 20cm/min and a total sliding distance of about 880m. Following the fitting procedure illustrated in Fig. 3.3, the Raman peak positions for each spectrum were determined and the fitting results are shown in Fig. 3.6. Figure 3.6(a) shows the Raman peak positions for spectra collected from inside the coating wear tracks. Similar to what is shown in Fig. 3.3, each spectrum has two dominant Raman bands, one of which is located at a higher wave number, the other of which is located at a lower wave number. Very small error bars on the data points

indicate that repeated fitting made little change on the band positions. From Fig. 3.6(a), it can be seen that Raman band positions for spectra collected from inside the wear tracks on the coatings deposited at lower Ti cathode currents are approximately the same: each spectrum has a band positioned around  $1575\text{ cm}^{-1}$  and a band positioned around  $1350\text{ cm}^{-1}$ . Both bands are believed to be related to the existence of graphite-like materials in the wear tracks.

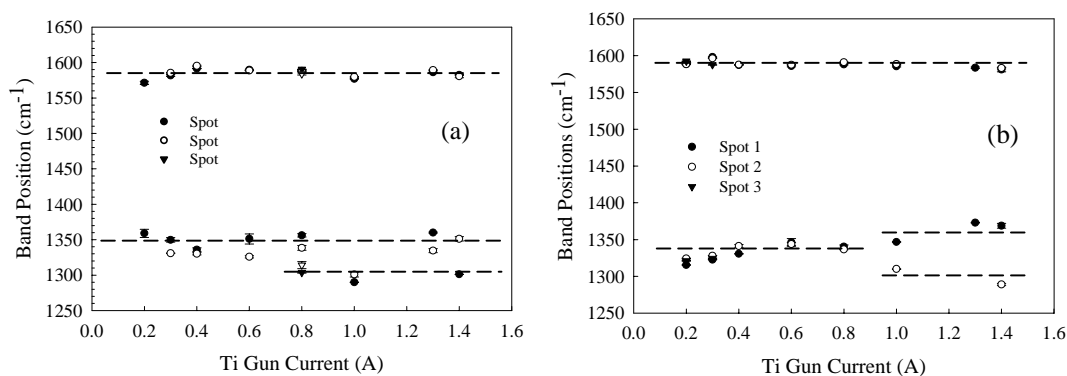


**Fig. 3.6 Fitting results for the dominant Raman peak positions from the wear tracks (a) and the corresponding steel balls used in the wear testing (b). The series of Ti-C:H coatings were deposited with Ti gun currents ranging from 0.2A to 1.4A**

In contrast, inside the wear tracks of the coatings deposited at high Ti cathode currents, while some of the collected spectra are similar to those collected from coatings with low Ti compositions, additional spectra were observed. These additional Raman spectra exhibit a band positioned around  $1575\text{ cm}^{-1}$  and another band positioned around the lower energy of  $1310\text{ cm}^{-1}$ . This band is believed to have its origin from some diamond-like materials. The existence of this diamond-like material in the coating wear tracks due to sliding may contribute to the increased friction coefficients and abrasive rates of the coatings with higher Ti composition. Similar Raman spectra were obtained from the corresponding steel balls after sliding, the results of fitting these spectra are shown in Fig 3.6(b). Figure 3.6(b) again indicates the development of carbonaceous transfer film on the mating balls during sliding contact with the Ti-C:H coatings.

Fig. 3.7 shows two typical traces of friction coefficients of Ti-C:H coatings sliding against steel balls in the ball-on-disk configuration under unlubricated conditions. Figure 3.7(a) shows one during sliding on a coating deposited at the Ti cathode current of 0.2A. The curve exhibits a gradual reduction in the friction coefficient initially and maintains a stable friction value of about 0.13 thereafter. This friction reduction corresponds to the formation of a transfer layer due to sliding, demonstrated previously with Raman spectroscopy, and a smoothening of surface asperities, which increases the contact area and results in a decrease of the actual contact stress. Figure 3.7(b) shows the friction coefficient during sliding on a coating deposited at the Ti cathode current of 1.4A. In contrast to data shown in Fig. 3.7(a), this curve shows much increased irregularity during the entire sliding period. Strong oscillations in the friction coefficients were observed from the beginning to the end with an average value of about 0.3. Differences between these two curves may be partially explained through the difference in transfer films

formed, as indicated in Fig. 3.5 and Fig. 3.6. Data shown in both figures suggest that, on coatings deposited at higher Ti cathode currents, some diamond-like materials form in addition to the graphite-like materials which forms due to sliding on all Ti-C:H coatings. The presence of the additional diamond-like materials may contribute to the increase of the average friction coefficient and the oscillations in the traces of friction coefficient versus sliding distance.

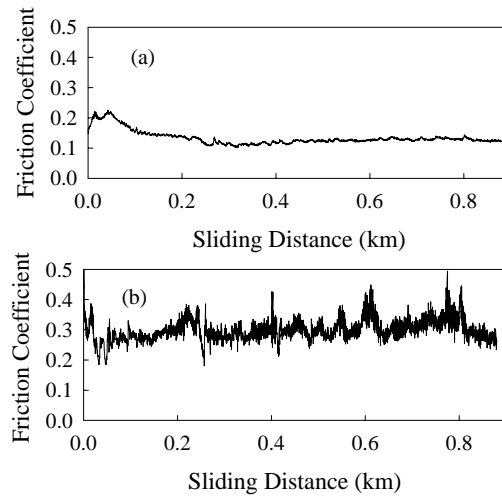


**Fig. 3.7 Typical traces of friction coefficients of Ti-C:H coatings sliding against steel balls with the ball-on disk mode under unlubricated sliding conditions: (a) coating coated with a Ti gun current of 0.2A; (b) coating coated with a Ti gun current of 1.4A**

Fig. 3.8 shows the friction coefficients of Ti-C:H coatings as a function of Ti cathode current during unlubricated sliding against steel balls. Figure 3.8(a) shows the average friction coefficient from a series of sliding tests to a distance of 6.4m, corresponding to running about 100 laps on the ball-on-disk setup. Figure 3.8(b) shows the results from a series of sliding tests to a distance of 880m, corresponding to running about 10,000 Laps. In both figures, average friction coefficients ranged from 0.13 on the low end to 0.27 on

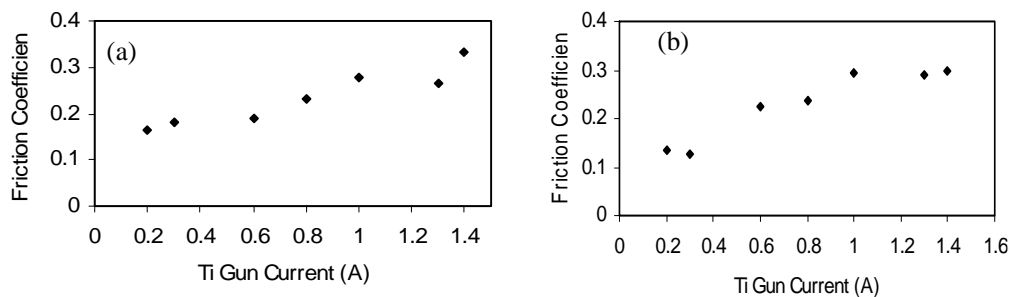


**Fig. 3.8 Friction coefficients of Ti-C:H coatings as a function of Ti cathode current during unlubricated sliding against steel balls with a sliding distance of (a) 6.4m running about 100 laps and (b) 880m running about 10,000 Laps**

the high end. The transition from low to high friction coefficient occurs at Ti cathode currents ranging from 0.3A to 0.6A. The present result, showing increasing friction coefficients with increasing Ti composition within the coating, confirms previous observations<sup>13</sup>. Difference between the two figures indicates that friction coefficients corresponding to coatings deposited at lower Ti cathode currents decrease as the sliding distance increases, while those corresponding to coatings deposited at higher Ti cathode currents seem to be less dependent on the sliding distance. The sensitivity of friction coefficient to the sliding distance again suggests the role transfer films plays in determining the friction behavior.

Figures 3.9(a) shows the abrasion rate of one Ti-C:H coating deposited at Ti cathode current of 0.2A as a function of the number of sliding laps during a series of ball-on-disk sliding tests. Figure 3.9(b) shows the rate of abrasion of the steel ball during unlubricated sliding against Ti-C:H coatings as a function of the Ti cathode current used for coating deposition. All abrasion results shown in Fig. 3.9(b) were obtained at a total sliding distance of about 880m, corresponding to running about 10,000 laps. The abrasion rate was calculated by the volume of material worn off the steel ball after one sliding test divided by the normal load and the total sliding distance. The ball abrasion rate, shown in Fig. 3.9(a), exhibits a power law dependence on the numbers of sliding laps. This observation is consistent with a previous study, and was attributed to a gradual loss of sharper surface asperities as the sliding test continues<sup>19</sup>. The dependence of the abrasion rate on the Ti composition of the coating (or the Ti cathode current used during deposition), shown in Fig. 3.9(b), also displays a transition from a low abrasion region with an average value of  $\sim 3 \times 10^{-7} \text{ mm}^3/\text{N}\cdot\text{m}$  to a high abrasion region with an average value of  $\sim 6 \times 10^{-6} \text{ mm}^3/\text{N}\cdot\text{m}$  as the Ti cathode current increases from 0.6A to 1.0A. Combining with result shown in Fig. 3.8(b), it is seen that Ti-C:H coatings have a low friction/low abrasion region, when the Ti cathode currents are below 0.3A, and a high friction/high abrasion region, when the Ti cathode currents are above 0.6A.

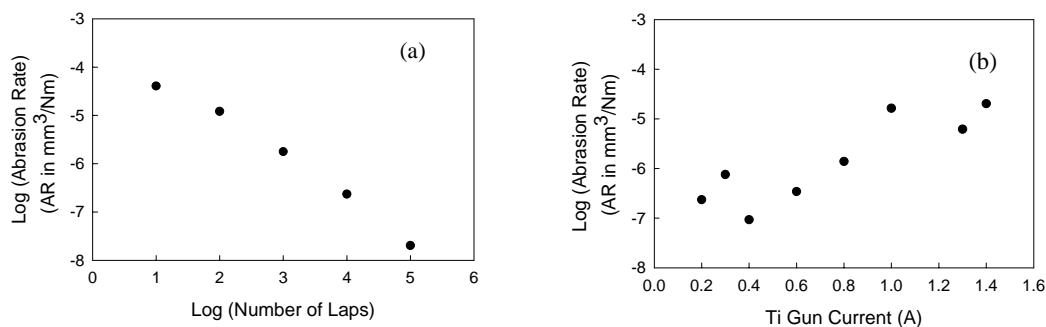


**Fig. 3.9 (a) Steel ball abrasion rate of one Ti-C:H coating deposited with a Ti cathode current of 0.2A as a function of the number of sliding laps; (b) Abrasion rates of Ti-C:H coatings as a function of the Ti cathode current used for coating deposition. Abrasion rates were obtained from unlubricated sliding tests with a sliding distance of  $\sim 880\text{m}$ , corresponding to running  $\sim 10,000$  laps**

Fig. 3.10(a) and (b) show typical surface morphologies, as measured by AFM, of Ti-C:H coatings deposited on steel coupons at Ti cathode current of 0.3A and 1.4A, respectively. The surface undulations seen in both figures are typical of Ti-C:H coatings.

The average roughness ( $R_a$ ) of a series of Ti-C:H coatings deposited on 52100 steel coupons has been determined from AFM images. As the Ti cathode current during coating deposition varies from 0.2 to 1.4 A,  $R_a$  of as-deposited Ti-C:H coatings is  $\sim 20$  nm, approximately independent of the Ti composition.

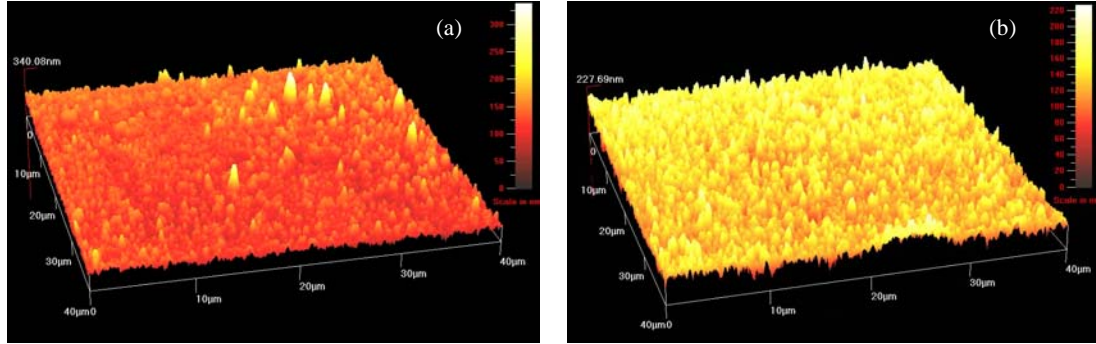


**Fig. 3.10** Typical surface morphologies as seen by AFM of as-deposited Ti-C:H coatings: (a) coating deposited at a Ti cathode current of 0.3A; (b) coating deposited at a Ti cathode current of 1.4A

Fig. 3.11(a) and (b) show respectively the surface morphologies inside the wear tracks of two coatings after sliding tests to the same distance of  $\sim 880$ m. The two coatings were deposited respectively at the Ti cathode currents of 0.3A and 1.4A, whose as-deposited surfaces are shown respectively in Fig. 3.10(a) and 3.10(b). The wear track on the coating deposited at the lower Ti cathode current, as shown in Fig. 3.11(a), with an

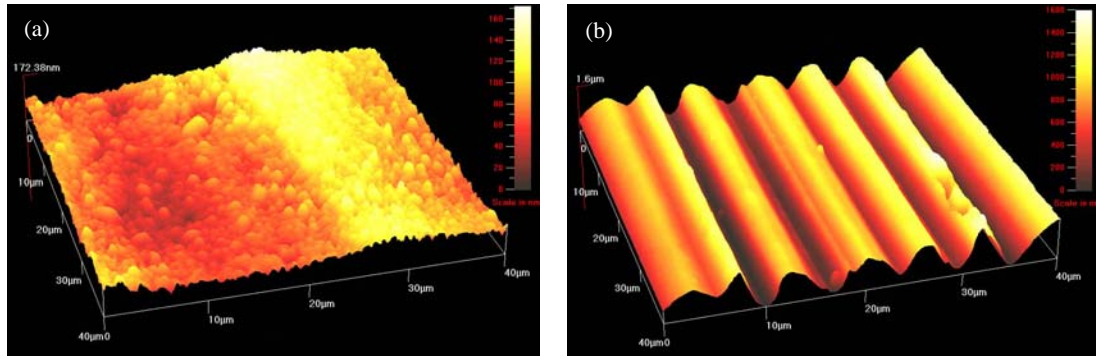


**Fig. 3.11** Typical surface morphologies as seen by AFM inside the wear tracks on Ti-C:H coatings deposited at Ti cathode current of 0.3A (a) and 1.4A (b). The morphologies shown were developed after sliding  $\sim 880$ m against a steel ball

average friction coefficient of 0.13 and a ball abrasion rate of  $7.5 \times 10^{-7} \text{ mm}^3/\text{N}\cdot\text{m}$ , is quite smooth. Surface roughness is measured to be  $\sim 48$ nm. In contrast, the wear track on the coating deposited at the higher Ti cathode current, shown in Fig. 3.11(b), shows microscale grooves parallel to the sliding direction. The surface roughness is measured to be  $\sim 243$ nm. The measured friction coefficient is  $\sim 0.3$ , which is 2.3 times of that in the

first case. The ball abrasion rate is  $\sim 2.0 \times 10^{-5} \text{ mm}^3/\text{N}\cdot\text{m}$ , which is 40 times of that in the first case.

Figures 3.12(a) and (b) show optical micrographs of the wear scars on the two 52100 steel balls after sliding against the two Ti-C:H coatings shown in Fig. 3.10 and Fig. 3.11, respectively. As shown in Figure 3.12(a), sliding contact with the Ti-C:H coating with the lower Ti composition led to the formation of a transfer film which covers almost the entire wear scar on the mating steel ball. In contrast, Figure 3.12(b) shows that the

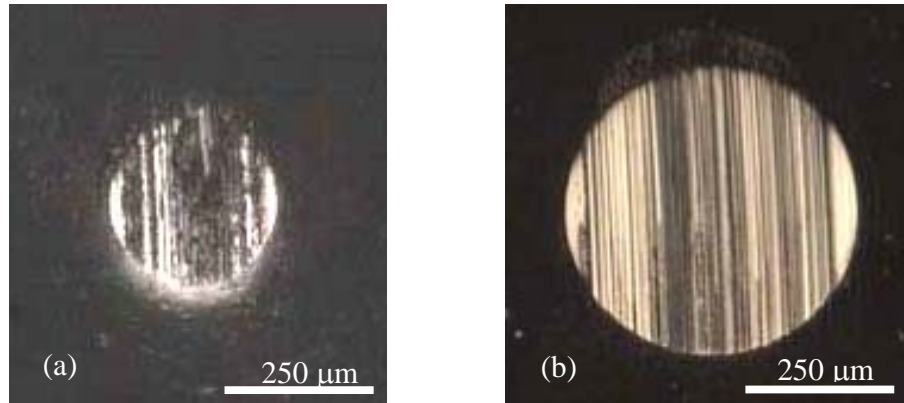


**Fig. 3.12 Optical micrographs of 52100 steel balls after unlubricated sliding against Ti-C:H coatings for a total distance of 880 m: (a) image of ball wear scar against a Ti-C:H coating deposited on a 52100 steel coupon at a Ti cathode current of 0.3 A; (b) image of ball wear scar against a Ti-C:H coating deposited on a 52100 steel coupon at a Ti cathode current of 1.4 A**

transfer film resulting from sliding contact with the Ti-C:H coating with the higher Ti composition covers the wear scar on the mating steel ball sparingly. Micro-Raman spectra obtained from the transfer film regions on the steel ball shows a-C:H like signatures. Figure 3.12 shows that the Ti composition of the Ti-C:H coatings affects transfer film formation on the mating steel balls during unlubricated sliding and the difference in transfer film formation is at least partly responsible for the observed difference in friction coefficient as the Ti composition of the coating changes. From the difference in the size of the wear scar shown in Figure 3.12, it can also be discerned that the abrasiveness of Ti-C:H coatings increases with increasing Ti composition.

## Conclusion

Friction and abrasion of Ti-C:H coatings have been studied as a function of the Ti composition by using 52100 steel balls sliding against the coatings in an unlubricated ball-on-disk configuration. Both friction coefficient and abrasion rate of steel ball vary as a function of Ti cathode current, and have a low friction/low abrasion region at lower Ti cathode currents and a high friction/high abrasion region at higher Ti cathode currents.

While graphite-like transfer films are developed both in the coating wear tracks and on the mating steel balls at all Ti compositions, indication of diamond-like carbonaceous material formation in the coating wear tracks and on the corresponding steel balls is

suggested by the Raman evidence when the Ti-C:H coatings are deposited at higher Ti cathode currents. The formation of these diamond-like material due to sliding may be one contributing factor to the observed bimodal friction and abrasion characteristics of Ti-C:H coatings.

In addition, transfer film coverage of the mating steel balls is observed to vary with the coating composition. While transfer films developed during sliding contacts with Ti-C:H coatings of lower Ti compositions cover almost the entire wear scar on the mating steel ball, transfer films resulting from sliding contact with Ti-C:H coatings with higher Ti compositions covers the wear scar on the mating steel ball sparingly. This variability in transfer film formation may be another contributing factor to the bimodal friction and abrasion characteristics of Ti-C:H coatings.

Little difference exists in the surface morphologies of as-deposited coating in the entire Ti composition range examined. In contrast, after unlubricated sliding tests, surface morphologies in the coating wear track are observed to vary depending on the coating composition. At lower Ti cathode currents, coating wear tracks are relatively smooth, while rough wear tracks consisting of microscale grooves are observed at higher Ti cathode currents.

## References

- 1 C. P. Klages, R. Memming, Microstructure and physical properties of metal-containing hydrogenated carbon films, *Mater. Sci. Forum*, 52/53, (1990) pp.609-644
- 2 W. J. Meng, T. J. Curtis, L. E. Rehn, and P. M. Baldo, Plasma-Assisted Deposition and Characterization of Ti-Containing Diamondlike Carbon Coatings, *J. Appl. Phys.*, 83 (11), (1998) pp. 6076-6081
- 3 W. J. Meng, T. J. Curtis, L. E. Rehn, and P. M. Baldo, Mechanical Properties of Ti-Containing and W-Containing Diamond-like Carbon Coatings, *J. Appl. Phys.*, 84 (8), (1998) pp. 4314-4321
- 4 W. J. Meng, R. C. Tittsworth, J. C. Jiang, B. Feng, and D. M. Cao, Ti Atomic Bonding Environment in Ti-Containing Hydrocarbon Coatings, *J. Appl. Phys.* 88, (2000) pp. 2415-2422
- 5 W. J. Meng, R. C. Tittsworth, and L. E. Rehn, Mechanical Properties and Microstructure of TiC/Amorphous Hydrocarbon Nanocomposite Coatings, *Thin Solid Films*, 377-378, (2000) pp. 222-232
- 6 D. M. Cao, B. Feng, W. J. Meng, L. E. Rehn, P. M. Baldo, and . M. Khonsari, Friction and Wear Characteristics of Ceramic Nanocomposite Coatings: Titanium Carbide/Amorphous Hydrocarbon, *Appl. Phys. Lett.*, 79 (3), (2001) pp. 329-331
- 7 R. Wei, P. J. Wilbur, M. J. Liston and G. Lux, Rolling-contact-fatigue wear characteristics of diamond-like hydrocarbon coatings on steels, *Wear*, 162/164, (1993) pp. 558-568

- 8 Y. Liu, and E. I. Meletis, Evidence of graphitization of diamond-like carbon films during sliding wear, *J. Mater. Sci.*, 32 (13), (1997) pp. 3491-3495
- 9 A. Varma, V. Palshin, E. I. Meletis, and C. Fountzoulas, Tribological behaviour of Si-DLC coatings, *Surf. Engr.*, 15 (4), (1999) pp. 301-306
- 10 W. J. Meng, and T. J. Curtis, Inductively coupled plasma assisted physical vapor deposition of titanium nitride coatings, *J. Elecron. Mater.*, 26 (11), (1997) pp. 1297-1302
- 11 W. J. Meng, T. J. Curtis, L. E. Rehn, and P. M. Baldo, Temperature dependence of inductively coupled plasma assisted growth of TiN thin films, *Surf. Coat. Technol.* 120/121, (1999) pp. 206-212
- 12 W. J. Meng, E. I. Meletis, L. E. Rehn and P. M. Baldo, Inductively coupled plasma assisted deposition and mechanical properties of metal-free and Ti-containing hydrocarbon coatings, *J. Appl. Phys.* 87 (6), (2000) pp. 2840-2848
- 13 D. M. Cao, B. Feng, W. J. Meng, L. E. Rehn, P. M. Baldo and M. M. Khonsari, Friction and Wear Characteristics of Ceramic Nanocomposite Coatings: Titanium Carbide/Amorphous Hydrocarbon, *Appl. Phys. Lett.* 79 (3), (2001) pp. 329-331
- 14 J. Schwan, S. Ulrich, V. Batori, H. Ehrhardt and S. R. P. Silva, Raman spectroscopy on amorphous carbon films, *J. Appl. Phys.*, 80 (1), (1996) pp. 440-447
- 15 A. C. Ferrari, J. Robertson, Interpretation of Raman spectra of disordered and amorphous carbon, *Phys. Rev. B* 61, (2000) pp.14095-14107
- 16 E. Mounier, F. Bertin, M. Adamik, Y. Pauleau, P. B. Barna, Effect of the substrate temperature on the physical characteristics of amorphous carbon films deposited by dc magnetron sputtering, *Diamond Relat. Mater.* 5 (12), (1996) pp. 1509-1515
- 17 H. Poulet, J. P. Mathieu, *Vibration Spectra and Symmetry of Crystals*, Gordon and Breach, New York (1976)
- 18 J. Roberson and E. O'Reilly, Electronic and atomic structure of amorphous carbon, *Physical Review B, Condensed Matter and Materials Physics.* 35, (1987) pp. 2946-2957
- 19 S. J. Harris and A. M. Weiner, Scaling relationships for the abrasion of steel by diamondlike carbon coatings, *Wear*, 223 (1-2), (1998) pp. 31-36



## CHAPTER 4. CONFORMAL COATING OF Ti-C:H NANOCOMPOSITES OVER LIGA FABRICATED HIGH-ASPECT-RATIO MICROSCALE STRUCTURES AND ITS MEMS APPLICATIONS \*

### Introduction

Microelectromechanical system (MEMS) devices, both passive and active, are targeted for applications in harsh environments such as high temperatures, corrosive media, or severe mechanical contact. With regard to active devices, micro-devices involving moving parts in contact, such as gear trains or combustion chambers with piston-cylinder devices, require component surfaces to possess adequate oxidation/corrosion resistance, appropriate tribological characteristics, and good high temperature stability. This chapter will focus on LiGA-fabricated (Lithographie, Galvanoformung, Abformung)<sup>12</sup> passive devices, examples of which include cross flow micro heat exchangers<sup>34</sup>, mechanical seals with micro heat exchangers embedded under the active sealing surface<sup>5</sup>, or catalytic converters with micro pores. The three-step LiGA microfabrication process consists of X-ray lithography, electrodeposition, and molding. The mold inserts that result at the completion of the electrodeposition step have features with vertical sidewalls. These inserts are routinely used to compression mold or injection mold high-aspect-ratio micro-scale structures (HARMS) with heights exceeding 1 mm and with height-to-width ratios exceeding 10. The molding step makes possible, at least in theory, economic mass production of polymeric, metallic or ceramic components, although molding of polymeric HARMS has been by far the most successfully implemented<sup>67</sup>.

The passive applications listed above all involve flow of a fluid through banks of micro channels with lengths of 1-2 mm and length/diameter ratios of 2-10 to increase the efficiency of heat or mass transfer. For these applications, the importance of integrated circuit (IC) processing compatibility, which is often an integral component of MEMS design architecture, is much reduced relative to robust mechanical/chemical performance. In many situations, far more important are the near-surface properties of the component, such as corrosion or wear resistance, which may not be adequately provided by the bulk material from which the component is fabricated. In these cases, appropriate conformal coatings on topologically complex surfaces may be required. Fig. 4.1 shows a cross flow micro heat exchanger that has recently been fabricated and is currently being tested as a micro boiler. When used as a boiler, hot combustion gases pass through the plane of the heat exchanger via thousands of parallel channels converting water to steam as it passes within the plane of the boiler. In this application, corrosion resistance and high temperature stability are of importance, especially on the hot gas side, and the surface properties of the electrodeposited Ni from which the heat exchanger are made become unacceptable. A conformal coating that protects the complex gas-side surface of the boiler could greatly enhance the performance/life of the boiler.

Another example where properties of the near-surface region are critical is the molding of HARMS, especially metallic HARMS. An electrodeposited Ni mold is shown in Fig. 4.2(a). Such molds have been used to mold polymeric structures such as the one

---

\* Reprinted from Thin Solid Films with the permission of Elsevier

shown in Fig. 4.2(b). At present, attempts to mold similar metallic structures have not been successful. One reason for this difficulty lies in the fact that the injected or embossed metal reacts and bonds with the electrodeposited mold insert. This, coupled with the disadvantage that LIGA mold inserts do not provide a taper for easy part release, explains the present difficulties in molding metallic HARMS. Modifying the near-surface region of the mold insert with a coating that can eliminate the formation of a strong bond between the insert and the molded metal part and facilitate part release.

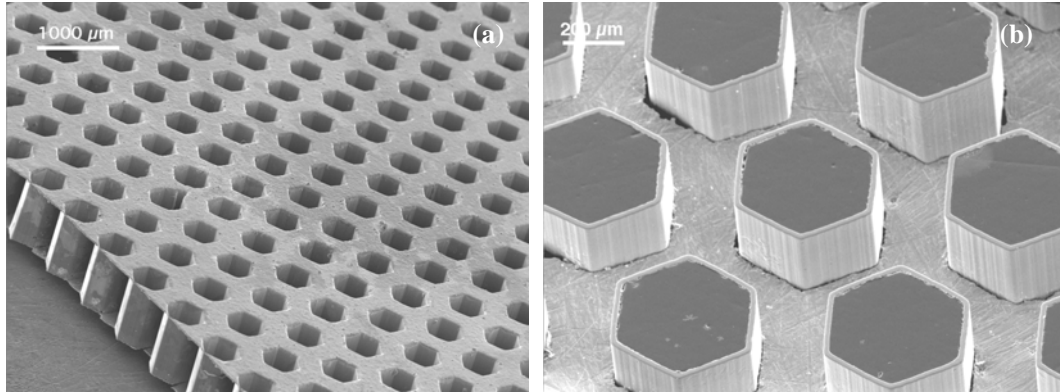


**Fig. 4.1 A LIGA fabricated Ni cross flow micro heat exchanger: (a) a magnified view of the heat exchanger, (b) a cut away view of the heat exchanger showing internal channel geometry <sup>4</sup>**

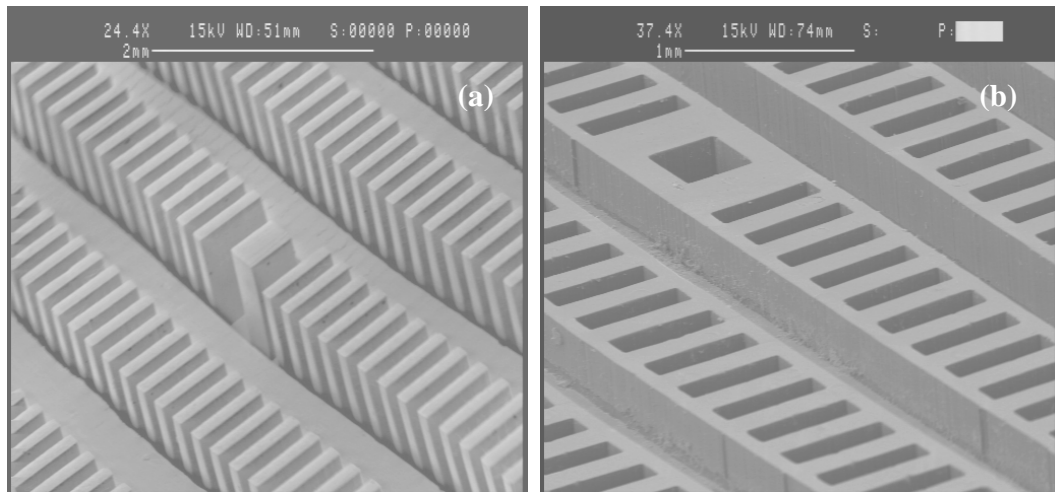


**Fig. 4.2 Molding of micro-scale structures: (a) an electrodeposited Ni micro mold insert, (b) a molded polymer part from the Ni mold insert <sup>3</sup>**

Engineering HARMS-covered surfaces by coatings must satisfy two criteria. First, the coating needs to be synthesized with desired mechanical, tribological, and chemical properties and it must adhere strongly to the surface. Second, the coating needs to cover topologically complex HARMS-covered surface in a conformal fashion. In this paper, we investigate applying Ti-containing hydrocarbon (Ti-C:H) coatings to LiGA-fabricated Ni

HARMS. Ti-C:H coatings have been shown to be pseudo-binary nanocomposites consisting of nanocrystalline B1-TiC embedded within an amorphous hydrocarbon (a-C:H) matrix<sup>8</sup>. The elastic modulus and hardness of these coatings vary systematically with the Ti composition over a wide and useful range<sup>9</sup>. When Ti-C:H coatings contact WC-Co in unlubricated sliding, the friction coefficient and the coating wear rate are much lower than those for a Ni/WC-Co contacting pair. In addition, the coating composition significantly influences the friction coefficient and coating wear rate<sup>10</sup>. We present preliminary results on conformal deposition of Ti-C:H coatings on electrodeposited Ni HARMS by plasma-assisted vapor phase deposition. In addition, we report on tribological characteristics of Ti-C:H coatings on macro-scale flat surfaces in unlubricated sliding contact as a function of the Ti composition.

## Experimental

Electrodeposited Ni HARMS were fabricated with the LiGA technique using the combined facilities of the Micro-systems Engineering Team ( $\mu$ SET) and the electron synchrotron facility of the Center for Advanced Microstructures and Devices (CAMD) at Louisiana State University. The X-ray masks were fabricated by  $\mu$ SET and consist of Au absorber structures supported by a 200  $\mu$ m thick graphite membrane. Polymethyl methacrylate (PMMA) sheets on 304 stainless steel substrates were exposed to X-ray from the synchrotron running at 1.3 GeV. Ni electrodeposition into developed PMMA cavities on stainless steel substrates was carried out in a Ni sulfamate solution. After electrodeposition, the structures were soaked in acetone to remove the residual PMMA, cleaned in acetone and methanol, and used as substrates for coating deposition. Further details on X-ray mask fabrication, PMMA sheet exposure and development, and Ni electrodeposition have been described elsewhere<sup>11</sup>.

Deposition of Ti-C:H coatings was carried out in an inductively coupled plasma (ICP) assisted hybrid chemical/physical vapor deposition (CVD/PVD) tool, which combines a 13.56 MHz ICP with balanced magnetron sputter sources. Cleaned Ni HARMS substrates were loaded into the deposition tool through a load lock. Base pressure prior to coating deposition was  $\sim 2 \times 10^{-8}$  Torr. The deposition sequence consisted of plasma etching of substrate surfaces in a pure Ar ICP at a substrate bias voltage of  $-100$  V, pure Ti interlayer deposition, and Ti-C:H deposition. The deposition of a pure Ti interlayer promotes coating/substrate adhesion, and was carried out by sputter deposition with the ICP shut off. Ti-C:H deposition was carried out in the hybrid CVD/PVD mode, in which two facing magnetron sources sputtered two pure Ti cathodes (99.99+%) in an Ar(99.999+%/C<sub>2</sub>H<sub>2</sub>(99.99+%) ICP at a total pressure  $\sim 1.7$  mTorr. The substrate bias voltage during Ti interlayer and Ti-C:H deposition was  $-50$  V. For all depositions, the two Ti cathodes were operated at equal currents and the substrates were rotated continuously in the center of the deposition zone at  $\sim 12$  revolutions/min. At a fixed ratio of Ar and C<sub>2</sub>H<sub>2</sub> input flow rates and a fixed ICP input power, the Ti composition of the Ti-C:H coating was varied by varying the Ti cathode currents. The hybrid CVD/PVD tool and Ti-C:H deposition procedures have been described in more detail elsewhere<sup>12 13 14</sup>. No intentional substrate heating or cooling was applied during the entire deposition process.

Electron probe microanalysis (EPMA) on a JEOL 733 microprobe was used to qualitatively evaluate the compositional variations of Ti-C:H thin films as a function of

position along electrodeposited Ni HARMs. An incident electron beam energy of 6 keV was used. Ti, C, and Ni k-ratios were obtained with a pure Ti, diamond, and a pure Ni specimen as the standard, respectively<sup>15</sup>. Auger electron spectroscopy and Auger sputter depth profiles of Ti-C:H coatings deposited onto electrodeposited Ni HARMs were obtained using a Physical Electronics PHI 680 scanning Auger nanoprobe as a function of position along the HARMs features, which quantitatively determines the compositional variations of Ti-C:H thin films as a function of position along electrodeposited Ni HARMs. Data were acquired using a 10 kV, 10 nA electron beam. Auger spectra were recorded in the N(E) mode and were derivatized using a 5-point moving average derivative filter. Peak-to-peak intensities were adjusted using vendor supplied sensitivity factors and normalized to 100 atomic percent. The carbon line was further treated using a linear least squares fitting routine. Data were fitted to an ensemble average of data from the center of the amorphous carbon film. Auger sputter depth profiles were obtained by sputtering the specimen using a 5 kV Ar<sup>+</sup> beam. Sputter time was translated into sputter depth using data obtained from a 315A thick SiO<sub>2</sub> on Si standard. Scanning electron microscopy (SEM) examinations were carried out on a JEOL 840A microscope.

## Results and Discussion

The potential of conformal Ti-C:H deposition over LIGA fabricated Ni HARMs is illustrated in Fig. 4.3 and Fig. 4.4.

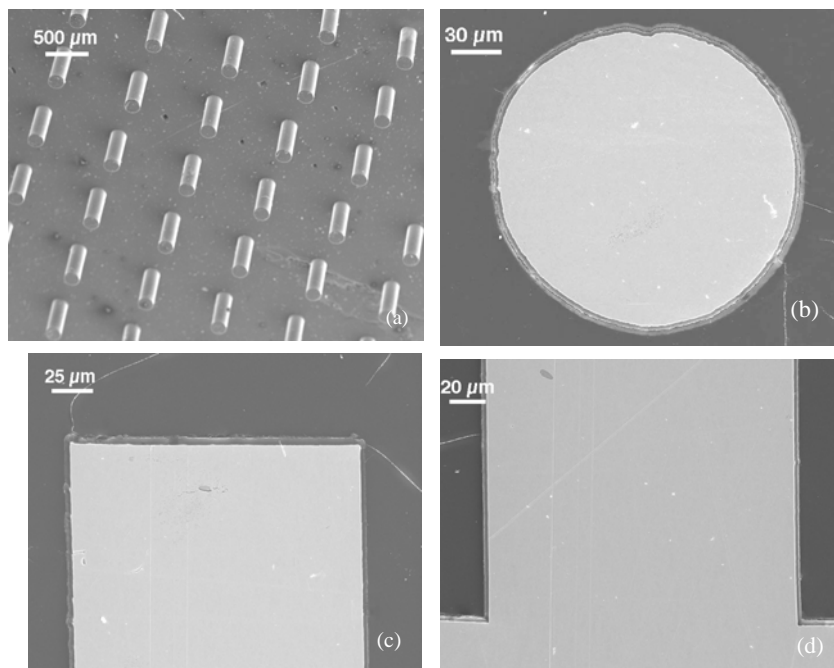


**Fig. 4.3 SEM micrographs of a square array of cylindrical Ni microposts after Ti-C:H deposition: (a) low magnification view; (b) cross-section perpendicular to post; (c) cross-section near the post top parallel to post, (d) cross-section near the post/substrate transition parallel to post**

Fig. 4.3(a) shows a SEM micrograph of a square array of cylindrical Ni microposts, on which a Ti-C:H film was deposited. The microposts are  $\sim 550 \mu\text{m}$  in height,  $\sim 180 \mu\text{m}$  in diameter, with a post-to-post spacing of  $\sim 915 \mu\text{m}$ . Fig. 4.3(b) shows a cross-sectional SEM micrograph of a micropost. The cross section is perpendicular to the post direction. A Ti-C:H film,  $\sim 3 \mu\text{m}$  in thickness, is deposited uniformly around the entire micropost perimeter, conforming to the surface geometry. Fig. 4.3(c) shows a cross-sectional SEM micrograph of the top portion of a micropost, with the cross section parallel to the post direction. Conformal Ti-C:H deposition is again evident, with post corners well covered. Fig. 4.4(d) shows another parallel cross-sectional SEM micrograph of the bottom portion of a micropost. Ti-C:H deposition has covered the entire post, including the post/substrate transition areas which form sharp corners.

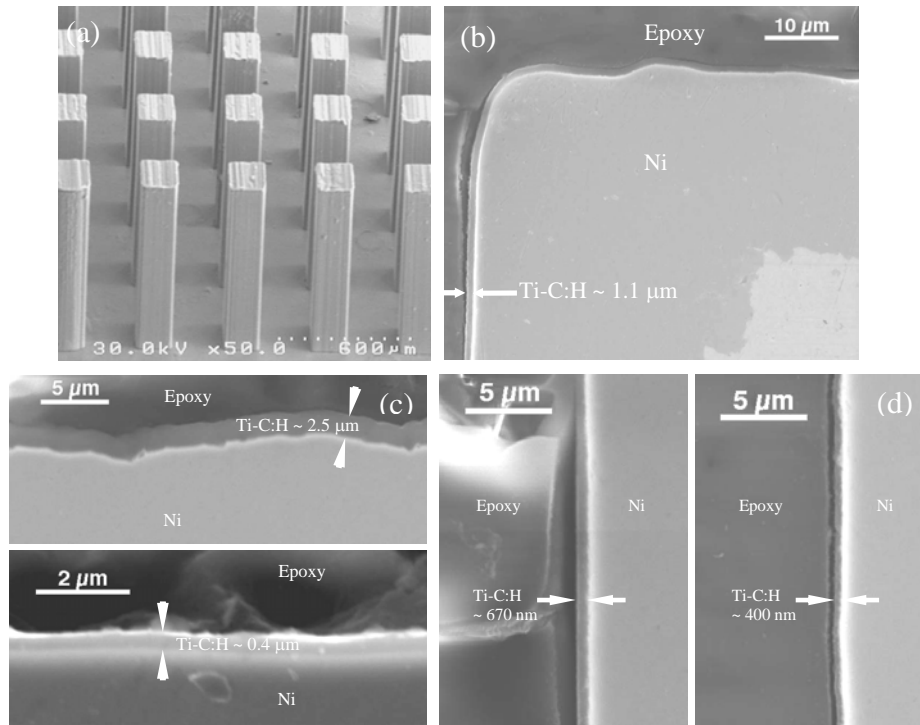


**Fig. 4.4 SEM images of Ti-C:H/Ti coated Ni HARMs: (a) a Ti-C:H/Ti coated field of square Ni microposts; (b) a cross-sectional image perpendicular to a post near the top of the post; (c) cross-sectional images parallel to a post showing respectively the coating on the top of the post and the bottom of the substrate between posts; (d) cross-sectional images parallel to a post showing respectively the coating on the post sidewall between the top and the middle and between the middle and the bottom**

Fig. 4.4(a) shows a field of square Ni microposts also coated with Ti-C:H with a different geometry as compared with those shown in Fig. 4.3. The microposts are  $150 \mu\text{m} \times 150 \mu\text{m}$  in cross section,  $1000 \mu\text{m}$  in height, and  $220 \mu\text{m}$  in post-to-post spacing, yielding a height to post spacing ratio of 4.5. Fig. 4.4(b) shows a cross-sectional SEM image perpendicular to one post near the top, clearly showing conformal deposition

around one corner of the post. Fig. 4.4(c) shows two cross-sectional SEM images parallel to one post, showing the coating on top of the post and on the bottom of the substrate between protruding posts. The coating thickness is  $\sim 2.5 \mu\text{m}$  on the top, and decreases significantly to  $\sim 0.4 \mu\text{m}$  on the bottom substrate surface between posts. A significant decrease in coating thickness on the post sidewalls is also observed. Fig. 4.4(d) shows two cross-sectional SEM images parallel to one post, showing the sidewall coating thickness decreases from  $\sim 0.67 \mu\text{m}$  between the top and the middle of the post to  $\sim 0.40 \mu\text{m}$  between the middle and the bottom of the post. Fig. 4.3 and Fig 4.4 shows that, with the present Ti-C:H deposition process, coating coverage over such HARMs-covered surfaces is conformal, but not uniform when the height to spacing ration of the microstructure is high.

Freestanding Ti-C:H microtubes were fabricated out of the Ti-C:H covered cylindrical microposts. After Ti-C:H deposition, the field of microposts was encapsulated in PMMA and mechanically polished perpendicular to the post direction until the Ti-C:H cap on each micropost was removed. The PMMA encapsulation was then dissolved in acetone, and the micropost structures were electrochemically polished in a solution of 57% $\text{H}_2\text{SO}_4$ /43% $\text{H}_2\text{O}$  (by volume) at room temperature. The electrochemical polishing was carried out in a galvanostatic mode with a current density of  $0.5 \text{ A/cm}^2$ . A total polishing time of 200 min was used. Because Ti-C:H is resistant to such as electrochemical attack, Ni was preferentially removed by electropolishing, leaving a Ti-C:H microtube structure. The pure Ti interlayer was also removed by the electropolishing process. Fig. 4.5(a) shows a SEM micrograph of a freestanding Ti-C:H microtube, whose height is  $\sim 280 \mu\text{m}$  after mechanical polishing. Some Ni remains at the tube bottom. A small crack in the microtube located at the top rim can be observed, resulting probably from damage during mechanical polishing. That this crack does not lead to disintegration of the microtube, even after the Ni substrate was removed, attests to the structural integrity of the Ti-C:H film. Fig. 4.5(b) shows the morphology of the Ti-C:H microtube external surface. The micrometer/sub-micrometer scale surface undulations are typical of plasma deposited hydrocarbon films. The Ti-C:H microtube shown in Fig. 4.5(a) has a height-to-wall thickness ratio of  $\sim 90$ . Such micro-scale structures with extremely high aspect ratios would be difficult to fabricate with the standard LIGA technique.

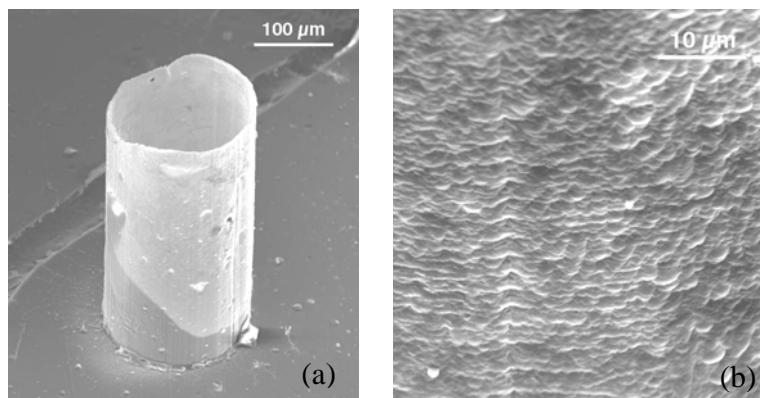


**Fig. 4.5 SEM micrographs of a freestanding Ti-C:H microtube: (a) overview of one microtube; (b) morphology of the microtube external surface**

The conformal Ti-C:H deposition by the hybrid CVD/PVD process onto Ni HARMs was further investigated with EPMA and AES combined with SEM by simultaneous deposition onto a set of Ni HARMs substrates with varying geometries.

Fig. 4.6(a) and (b) show respectively two SEM micrographs of a square array of cylindrical microposts and a linear array of rectangular microposts, on which a Ti-C:H film was deposited during the same run. The cylindrical microposts are  $\sim 520 \mu\text{m}$  in height,  $\sim 100 \mu\text{m}$  in diameter, with a post-to-post spacing of  $\sim 200 \mu\text{m}$ . The rectangular microposts are  $\sim 520 \mu\text{m}$  in height,  $\sim 10000 \mu\text{m}$  in width, and  $\sim 100 \mu\text{m}$  in thickness. The microposts shown in Figures 4.6(a) and 4.6(b) are from the middle of two entire arrays, which were dissected in half after the Ti-C:H deposition.

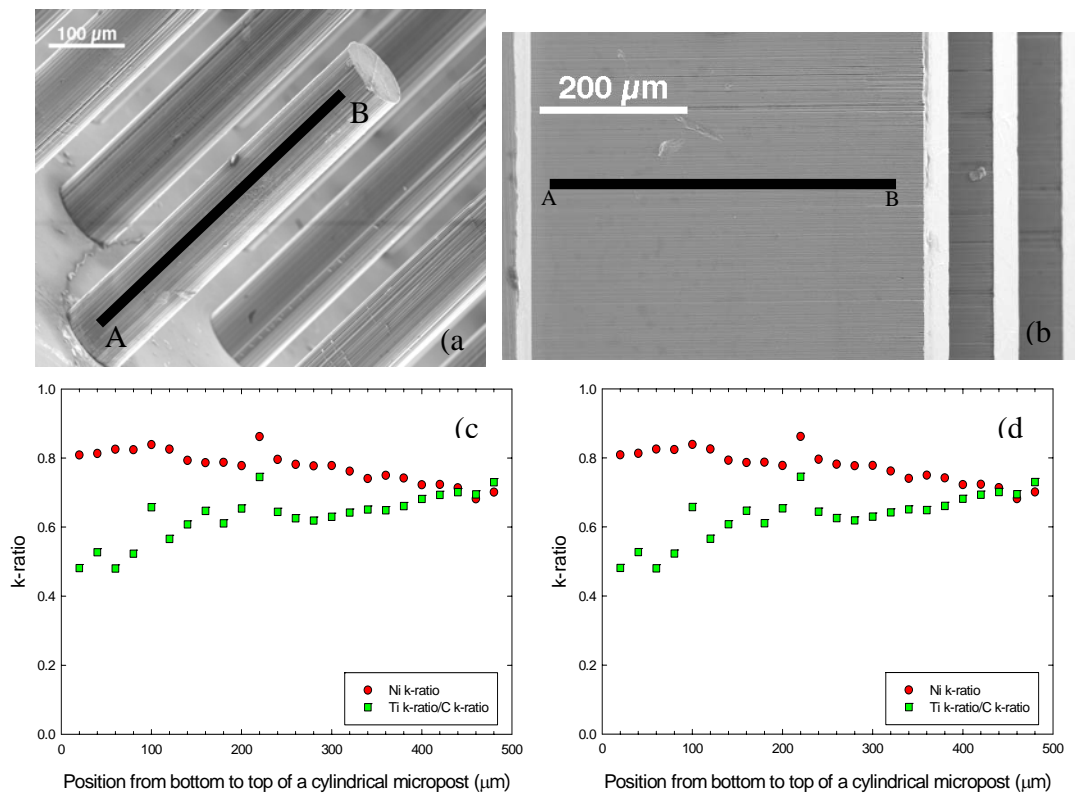


**Fig. 4.6 Compositional characterization of Ti-C:H covered Ni microposts: (a) a SEM micrograph of the cylindrical microposts; (b) a SEM micrograph of the rectangular microposts. EPMA measured Ni k-ratio and ratio of Ti k-ratio to C k-ratio as a function of position along the cylindrical micropost (c), and the rectangular micropost (d). In (a) and (b), A and B mark the 20  $\mu\text{m}$  and 480  $\mu\text{m}$  positions in (c) and (d), respectively**

Fig. 4.6(c) and (d) show respectively EPMA measured Ni k-ratio and the ratio of Ti k-ratio to C k-ratio as a function of position from bottom to top along the cylindrical micropost and rectangular micropost. The presence of Ti and C signals along the entire micropost sidewalls shows complete Ti-C:H coverage. On both microposts, a gradual decrease in the Ni k-ratio and a gradual increase in the ratio of Ti k-ratio to C k-ratio is

observed as the top of the post is approached. The increase in the ratio of Ti k-ratio to C k-ratio indicates that the total amount of Ti increases along the length of the micropost toward the top. The decrease in the Ni k-ratio as the top of the micropost is approached could result from increased Ti absorption, and/or an increase in the Ti-C:H/Ti film thickness. The smaller Ni k-ratio shown in Fig. 4.6(c) indicates that a thicker film was deposited onto the cylindrical micropost.

Whether deposition of Ti-C:H thin films onto electrodeposited Ni HARMs would lead to changes in the substrate surface morphology was investigated. Fig. 4.7(a) shows a SEM micrograph of a portion of the rectangular micropost field before Ti-C:H deposition. The striations along the micropost sidewalls resulted from imperfections in the graphite membrane X-ray mask. Fig. 4.7(b) shows a SEM micrograph of the micropost sidewall after Ti-C:H deposition. It is evident that the gross striations existed prior to deposition were replicated. Additional micrometer/sub-micrometer surface undulations are introduced due to Ti-C:H deposition, as shown in Fig. 4.5(b).

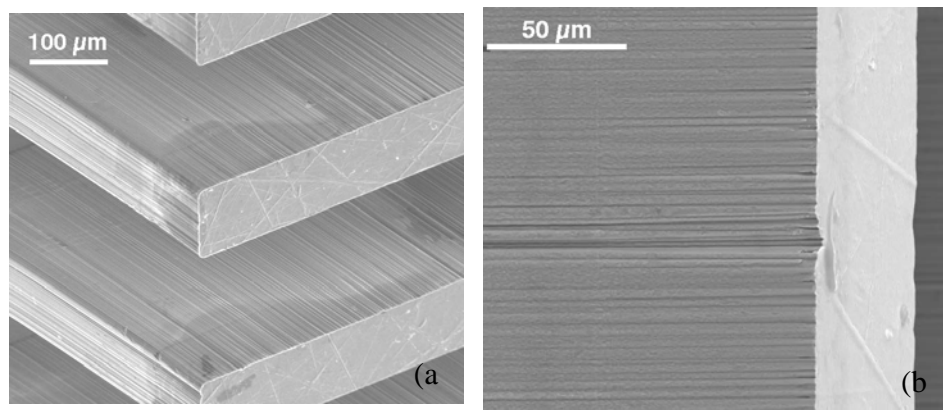


**Fig. 4.7 SEM micrographs of rectangular Ni microposts: (a) before Ti-C:H deposition, (b) after Ti-C:H deposition**

After Ti-C:H deposition, scanning Auger depth profiling was carried out on the top of rectangular and cylindrical microposts, on the bottom of the substrate between microposts, and on the micropost sidewalls close to the top, middle, and bottom, respectively. To obtain these spatially selective composition – depth profiles, ion beam sputtering of the post top and bottom between posts was carried out using a 1 mm × 1 mm raster and a sputter rate of 190 Å/min. Ion beam sputtering of the post sidewall was carried out using a 2 mm × 2 mm raster and a sputter rate of 50 Å/min. Auger spectra were acquired using an electron beam rastered over a 25 μm × 25 μm area after each ion beam sputtering step. Depth profiles on the micropost sidewall were obtained in a single ion beam sputtering experiment. Care was taken to ensure that the Auger analysis areas were in the center of the sputter crater.

Fig. 4.8 shows composition – depth profiles of the Ti-C:H coating deposited on one rectangular micropost as a function of location. The micropost is from the middle of a field with a post-to-post spacing of 400 μm. Fig. 4.5(a) shows composition – depth profiles on the top of the post and on the bottom between posts. The Ti-C:H layers appear to be uniform in composition, ~ 25 at. % Ti. The data show distinct Ti interlayers



between the Ni substrate and the Ti-C:H layers. Based on the increase of the Ni signal, the total coating thicknesses on the top and bottom are respectively 1.95 and 1.25  $\mu\text{m}$ , again showing a significant decrease in coating thickness from the top of the post to the bottom between posts. Coatings on the top and bottom between posts appear to be contamination free, with oxygen level close to the background ( $\sim 3$  at. %). Fig. 4.8(b) shows composition – depth profiles on the post sidewall. Based on the Ni signal increase, the total coating thicknesses near the top, middle, and bottom of the sidewall are 0.88, 0.62, and 0.50  $\mu\text{m}$ , respectively. As compared to the top and bottom between posts, coating thickness along the rectangular micropost sidewall is significantly smaller. As a function of location, coating thickness along the sidewall decreases towards the bottom. The coating/Ni interfaces also appear to be broader. The increased substrate sidewall roughness would contribute to this apparent interface broadening. Whether a distinct Ti interlayer exists on the sidewall as compared to the top and bottom between posts remains to be determined with probes of higher spatial resolution. The Ti composition of the Ti-C:H layer on the sidewall is slightly lower than that on the top and bottom between posts,  $\sim 21$  at. %, but shows no significant variation as a function of location along the sidewall. Data in Fig. 8(b) also show significant oxygen level within the Ti-C:H layers ( $> 10$  at. %). The oxygen level decreases with increasing depth into the coating.

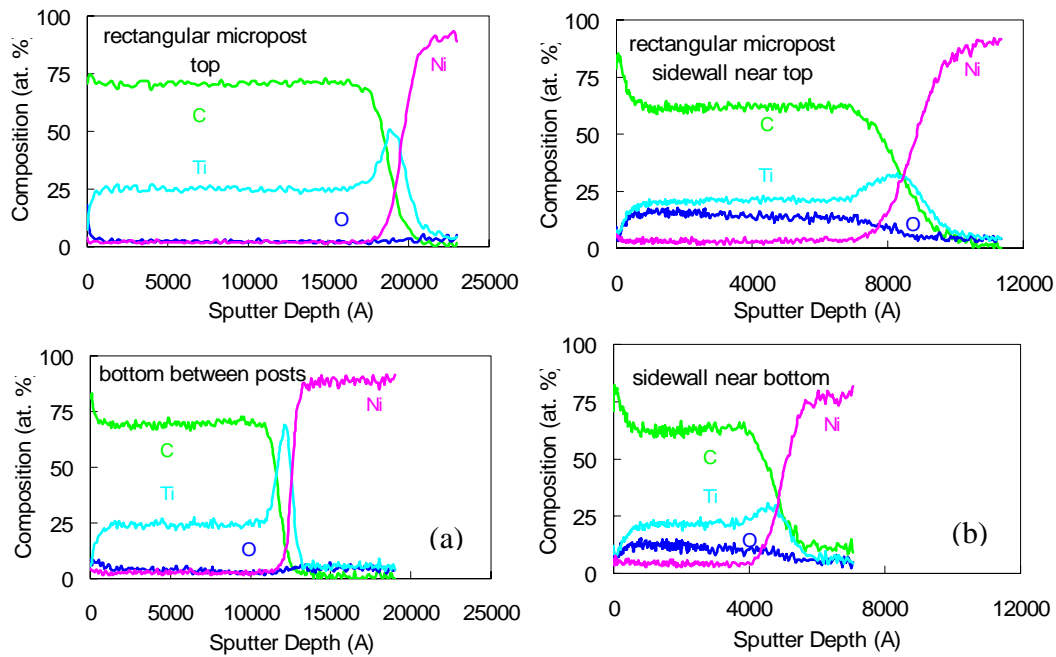


**Fig. 4.8 Composition – depth profiles of Ti-C:H/Ti deposited over a Ni rectangular micropost: (a) on the top of the post and on the bottom of the substrate between posts, (b) on the micropost sidewall near the top and the bottom**

Ti-C:H deposition occurred in the hybrid CVD/PVD mode. Fluxes of sputtered atomic Ti and hydrocarbon ions/radicals within the Ar/C<sub>2</sub>H<sub>2</sub> ICP arrive at the substrate surface and combine to form Ti-C:H. Argon ions also bombard the substrate surface

during Ti-C:H formation. At the deposition pressure of  $\sim 1.7$  mTorr, gas phase transport of sputtered Ti atoms is expected to be largely ballistic. Shadowing is therefore expected to decrease the Ti atom flux on the sidewall of the rectangular micropost towards the bottom. The fact that the Ti composition of Ti-C:H along the sidewall remains rather constant as a function of location suggests that the hydrocarbon flux responsible for deposition also decrease on the sidewall towards the bottom, which in turn suggests that the local plasma density decreases. Further plasma density and plasma potential measurements are needed to address these issues. The significant oxygen level within the Ti-C:H layers on the sidewall cannot be due to an external vacuum leak, since significant oxygen levels would then be expected in the Ti-C:H layers on the top and bottom between posts. The variation of oxygen level with depth is also inconsistent with an external vacuum leak. The reason for the presence of a significant amount of oxygen in the Ti-C:H layer on sidewalls remains unexplained at present.

Fig. 4.9 shows composition – depth profiles of the Ti-C:H coating deposited on one cylindrical micropost as a function of location. The micropost is from the middle of a field, again with a post-to-post spacing of 400  $\mu\text{m}$ . Based on the Ni signal increase, the total coating thicknesses on the top of the post, on the bottom between posts, and on the side wall near the top, middle, and bottom are 2.14, 1.76, 1.00, 1.07, and 0.98  $\mu\text{m}$ , respectively. With the more open substrate geometry, the coating thickness difference between the top and bottom between posts, as well as at different locations along the sidewall, is not as pronounced as in the rectangular micropost case. In particular, the sidewall coating thickness appears to be uniform, although still considerably smaller than the top and bottom coating thickness. Auger depth profiling again reveals no oxygen contamination within the coating on top and bottom, and a significant oxygen level of  $> 10$  at. % on the sidewall. The increase in coating/Ni interface broadening and the apparent lack of a well-defined Ti interlayer on the sidewall are similar to the observations made on the rectangular micropost. The Ti composition is approximately constant on top, bottom, and post sidewall,  $\sim 25$  at. %.

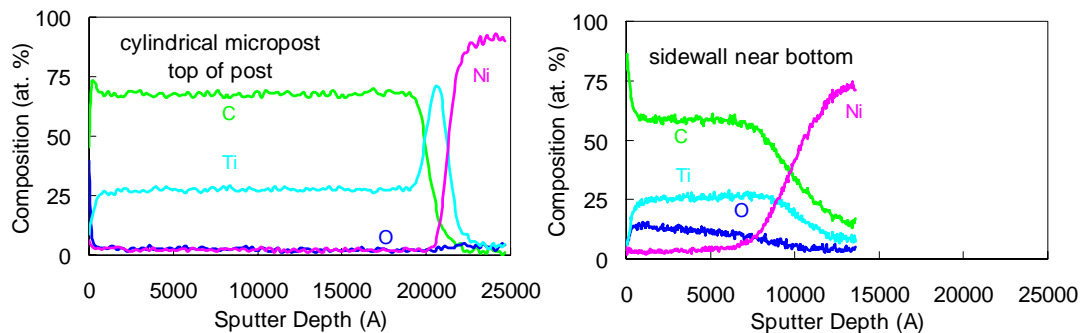


**Fig. 4.9 Composition – depth profiles of Ti-C:H/Ti deposited over a Ni cylindrical micropost: on the top of the post and on the post sidewall near the bottom**

Although the results presented demonstrates the potential of the ICP assisted CVD/PVD process and the Ti-C:H coating materials for HARMs based microsystem applications, much work remains. At present, the dominant gas phase species responsible for Ti-C:H deposition are not known. Understanding the dominant gas phase species and

their relationship to plasma parameters would contribute to developing better deposition procedures for more uniform coating coverage on HARMs. The possibility of supplying Ti from the gas phase by employing a Ti-containing gaseous precursor remains to be explored in the future. The issue of coating adhesion is critical for many of the envisioned applications involving micro-scale contact, and the understanding of which remains a scientific and technological challenge to be conquered.

## Summary

Preliminary results on conformal deposition of Ti-C:H thin films over LIGA fabricated Ni HARMs are reported. It is demonstrated that Ti-C:H coatings deposited by the ICP assisted hybrid CVD/PVD process over Ni HARMs with  $\sim 1000\ \mu\text{m}$  in height and  $\sim 220\ \mu\text{m}$  in mutual spacing are conformal, but not uniform. Coating composition appears to be relatively constant as a function of location along the micro-features. The structural integrity of the Ti-C:H films allowed freestanding, extremely high aspect-ratio structures to be built out of vapor deposited nanostructured ceramics. Applications involving HARMs based microsystems with engineered surfaces are currently being pursued.

## References

- 1 E. W. Becker, W. Ehrfeld, P. Hagmann, A. Manner, and D. Munchmeyer, Fabrication of Microstructures with Extreme Structural Heights by Synchrotron Radiation Lithography, Galvanoforming and Plastic Moulding (LiGA Process), *Microelectron. Eng.*, 4, (1986) pp.35-56
- 2 Maner, S. Harsh, W. Ehrfeld, *Plating and Surface Finishing*, pp 60-65, March 1988
- 3 C. Harris, M. Despa, K. W. Kelly, Design and Fabrication of a Cross Flow Micro Heat Exchanger, *IEEE J. MEMS.* 9, (2000) pp.502-508
- 4 C. Harris, K. W. Kelly, T. Wang, A. McCandless, Shari Motakef, Fabrication, Modeling, and Testing of Micro-Cross-Flow Heat Exchangers, *IEEE J. MEMS*, 11 (6), (2002) pp. 726-735
- 5 L. S. Stephens, K. W. Kelly, D. Kountouris, J. McLean, A pin fin microheat sink for cooling macroscale conformal surfaces under the influence of thrust and frictional forces, *IEEE J. MEMS*, 10 (2), (2001) pp. 222-231
- 6 R. Ruprecht, W. Bacher, J. Haublet, V. Piottter, *Proc. SPIE Micromachining and Fabrication Process Technology*, Vol. 2639, 146 (1995)
- 7 M. Despa, K. W. Kelly, J. Collier, Injection molding of polymeric LIGA HARMs, *Microsystem Technol.* 6(2), (1999) pp. 60-66

- 8 W. J. Meng, R. C. Tittsworth, J. C. Jiang, B. Feng, D. M. Cao, K. Winkler, V. Palshin, Ti atomic bonding environment in Ti-containing hydrocarbon coatings, *J. Appl. Phys.*, 88 (5), (2000) pp.2415-2422
- 9 W. J. Meng, R. C. Tittsworth, L. E. Rehn, Mechanical properties and microstructure of TiC/amorphous hydrocarbon nanocomposite coatings, *Thin Solid Films* 377/378, (2000) pp. 222-232
- 10 D. M. Cao, B. Feng, W. J. Meng, L. E. Rehn, P. M. Baldo, M. M. Khonsari, Friction and Wear Characteristics of Ceramic Nanocomposite Coatings: Titanium Carbide/Amorphous Hydrocarbon, *Appl. Phys. Lett.* 79 (3), (2001) pp. 329-331
- 11 D. M. Cao, T. Wang, B. Feng, W. J. Meng, K. W. Kelly, Amorphous hydrocarbon based thin films for high-aspect-ratio MEMS applications, *Thin Solid Films* 398/399, (2001) pp. 553-559
- 12 W. J. Meng, T. J. Curtis, Inductively coupled plasma assisted physical vapor deposition of titanium nitride coatings, *J. Electronic Materials*, 26 (11), (1997) pp. 1297-1302
- 13 W. J. Meng, T. J. Curtis, L. E. Rehn, P. M. Baldo, Temperature dependence of inductively coupled plasma assisted deposition of titanium nitride coatings, *Surf. Coat. Technol.* 120/121, (1999) pp. 206-212
- 14 W. J. Meng, E. I. Meletis, L. E. Rehn, P. M. Baldo, Inductively-coupled plasma assisted deposition and mechanical properties of metal-free and Ti-containing hydrocarbon coatings, *J. Appl. Phys.* 87 (6), (2000) pp. 2840-2848
- 15 S. J. B. Reed, *Electron microprobe analysis*, Cambridge University Press (1993)

## CHAPTER 5. COMPRESSION MOLDING OF Pb AND Zn WITH LiGA FABRICATED MICROSCALE MOLD INSERTS \*

### Introduction

Microfabrication technologies are being intensely investigated for constructing devices for electrical, biochemical, and mechanical engineering applications. Fabrication of high aspect ratio microscale structures (HARMS) with the LiGA (Lithographie, Galvanoformung, Abformung) technique, based on deep X-ray lithography and electrodeposition<sup>1,2</sup>, allows novel mechanical devices with enhanced performance, such as high-efficiency micro heat exchangers<sup>3</sup> and temperature controlled mechanical seals<sup>4</sup>, to be conceptualized. Beyond device concepts, incorporation of materials suitable for the intended device application is of paramount importance for actual device realization. For example, micro heat exchangers made of high thermal conductivity/low mass density metals such as aluminum is key to realizing the higher heat transfer per unit weight resulting from the reduced device length scale.

In the LiGA process, high energy X-ray radiation is used to perform deep lithography on resists, either polymethyl methacrylate (PMMA) or epoxy based SU-8, up to a few mm in thickness. Once the exposed resist layer is developed, electrodeposition of metals and alloys into the resist structure followed by chemical dissolution of the remaining resist yields either the final HARMS product or a metallic microscale mold insert. The mold insert can subsequently be used to mass produce secondary HARMS by compression molding<sup>5</sup>. The deep X-ray lithography step of LiGA requires resist exposure through patterned masks to high energy/high intensity X-rays typically available only from a synchrotron source. The high cost of synchrotron operation contributes dominantly to the high cost of direct LIGA fabricated HARMS and mold inserts, making the molding (Abformung) step of LIGA the key to economical production of HARMS based micro devices. Currently, replication of *metallic* HARMS by compression molding with LIGA fabricated inserts is not possible. This inability to mass replicate metallic HARMS limits the realization of micro heat exchangers and many other HARMS based mechanical devices.

One major obstacle to compression molding of metals is the chemical/mechanical interactions between the hot metal and the insert, which result in bonding and lead to damage of the insert, the molded metallic part, or both. In macroscale molding, lubricants are air sprayed onto the insert surfaces prior to molding<sup>6</sup>. For micromolding, because of the small linear dimensions (~200  $\mu\text{m}$ ) and high aspect ratios (>4) of the inserts, repeatable and uniform application of sprayed lubricants onto insert surfaces is difficult to achieve. A different approach is to modify the near-surface chemical/mechanical/tribological properties of the insert to alter the chemical/mechanical interactions between the hot metal and the insert surface, allowing easy and repeated insert/part separation.

Using a high-density inductively coupled plasma (ICP) assisted hybrid chemical/physical vapor deposition (CVD/PVD) technique, we have previously deposited Ti-containing hydrocarbon (Ti-C:H) coatings conformally onto LiGA fabricated HARMS<sup>7</sup>. As a prototypical example of two-phase ceramic nanocomposites, Ti-C:H coatings

---

\* Reprinted from Microsystem Technologies with the permission of Springer-Verlag

consist of nanocrystalline B1-TiC clusters embedded in an amorphous hydrocarbon (a-C:H) matrix<sup>8</sup>. The mechanical and tribological properties of Ti-C:H coatings, characterized by moderate hardness and low friction, depend systematically on the coating composition<sup>9</sup>. The coating microstructure undergoes a percolation-type transition, where it evolves from one with isolated TiC nanocrystals embedded in an a-C:H matrix to one with coalescing TiC nanocrystalline clusters percolating through the matrix and isolated a-C:H regions as the Ti composition increases<sup>10</sup>. The surface chemical properties are therefore expected to change as the coating composition changes. The ability to tune the chemical/mechanical/tribological properties of ceramic nanocomposite coatings makes them promising candidates for engineering surfaces of LIGA fabricated inserts for compression molding of metals.

In this chapter, the performance of Pb and Zn micromolding with LIGA fabricated microscale mold inserts is critically examined. We report similarities and differences in molding performance between uncoated Ni inserts and Ni inserts conformally coated with Ti-C:H coatings. Our preliminary results indicate that altering the insert near-surface chemical/mechanical/tribological properties is an effective approach for micromolding of reactive metals.

## Experimental

Ni microscale mold inserts, consisting of fields of cylindrical microposts 500  $\mu\text{m}$  in height and 100  $\mu\text{m}$  in diameter, were fabricated with the LIGA technique using the electron synchrotron at the Louisiana State University Center for Advanced Microstructures and Devices (LSU CAMD) and the electrodeposition facilities at Mezzo Systems Inc. Further details about the X-ray mask fabrication, X-ray exposure, PMMA pattern development, and Ni electrodeposition have been reported previously<sup>7</sup>. Residual PMMA was dissolved in acetone after Ni electrodeposition. All Ni inserts were cleaned in acetone and methanol prior to being used to compression mold Pb or Zn plates in the uncoated condition or to being used as substrates for Ti-C:H coating deposition.

Deposition of Ti-C:H coatings was carried out in an ICP assisted hybrid CVD/ PVD tool, which combines a 13.56 MHz ICP with balanced magnetron sputter sources. Further details on the hybrid tool have been reported previously<sup>11 12</sup>. The base pressure prior to Ti-C:H deposition was  $\sim 2.5 \times 10^{-8}$  Torr. The deposition sequence consists of a substrate surface etch, a Ti interlayer deposition, and a Ti-C:H layer deposition. Substrate etch occurred in a pure Ar ICP at a total pressure of  $\sim 1.7$  mTorr, a total ICP input power of 1000W, a substrate bias of  $-100\text{V}$ , and an etch duration of 10 minutes. The Ti interlayer deposition was carried out by sputter deposition for 15 minutes in pure Ar at a total pressure of  $\sim 1.7$  mTorr and a fixed Ti cathode current of 1.0 A. Ti-C:H deposition was carried out for 20 minutes in the hybrid CVD/PVD mode at a fixed ratio of Ar and  $\text{C}_2\text{H}_2$  gas input flow rates of 50/30, a total pressure of  $\sim 1.7$  mTorr, a fixed ICP input power of 1000W, and a Ti cathode current of 1.0A. The substrate bias during Ti interlayer and Ti-C:H deposition was  $-50\text{V}$ . Substrates were rotated continuously in the center of the deposition zone at  $\sim 12$  rpm during etching and depositions. No intentional substrate heating or cooling was applied during the entire deposition process.

Molding experiments were performed on a PHI Model TS-21-H-C(4A)-5 compression molding machine, shown schematically in Fig. 5.1(a). A molding chamber,

shown in Fig. 5.1(b), held the metal plate on the bottom half and the insert on the top half. An elastomer O-ring seal between the two halves of the molding chamber allowed it to be evacuated. Both the metal plate to be molded and the mold insert were heated prior to molding, whose temperatures were controlled through separate heaters/programmable temperature controllers. The molding chamber was placed between the two platens of the molding machine, which exerted a compression load on the molding chamber through a hydraulic oil system. Both 1/8 inch thick Pb plates and 3/16 inch thick Zn plates were molded with uncoated and Ti-C:H coated Ni inserts. The diameter of metal plates was 5.3 inches. The molding chamber was always evacuated to  $\sim 1$  Torr with a mechanical pump prior to molding. Identical temperature-time-force histories were used in molding experiments with uncoated and Ti-C:H coated inserts. In both Pb and Zn molding experiments, the insert and the metal plate were heated to  $300^{\circ}\text{C}$ , which is the maximum temperature reachable by the molding machine. Pb molding was performed at a total compression load of 650 lbs for 25 minutes. Demolding was carried out after cooling down to  $260^{\circ}\text{C}$  over a 5 minute period. Because of the significant strength of Zn at  $300^{\circ}\text{C}$ , load was gradually increased during Zn molding from 900 lbs to the maximum load capacity of 1400 lbs and the compression step lasted  $\sim 3$  hours. Shorter molding cycles did not produce sufficiently defined features on the Zn plate. Demolding was carried out immediately after the molding process without any intentional cooling. Due to the presence of guide pins and load springs on the molding chamber, the exact force exerted on the insert/plate pair during molding was unknown.

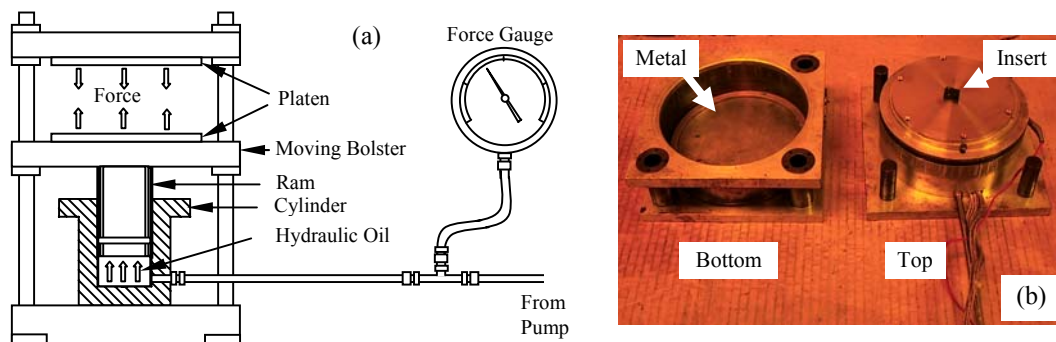
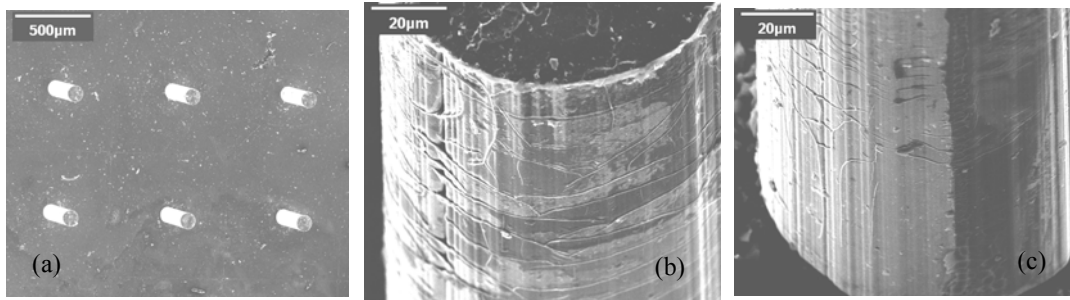


**Fig. 5.1 The PHI compression molding machine: (a) a schematic of the machine layout; (b) a photograph of the molding chamber with an insert mounted on the top half**

Scanning Electron Microscopy (SEM) examinations were carried out on a JEOL 840A microscope. Both the surfaces of the mold inserts and the molded features on the metal plates were examined. Cross sections were performed on the Ti-C:H coated Ni inserts, both perpendicular and parallel to the micropost direction. Cross sectional specimens were prepared by embedding the insert in epoxy, polishing with SiC papers of decreasing grit size from 240 to 800, and final polishing with  $1\mu\text{m}$  polycrystalline diamond suspension. Qualitative elemental analysis of the insert surface and the molded features on metal plates was performed with an X-ray energy dispersive spectrometer (EDS) attached to the SEM. EDS spectra were acquired using incident electron energy of 15 kV.

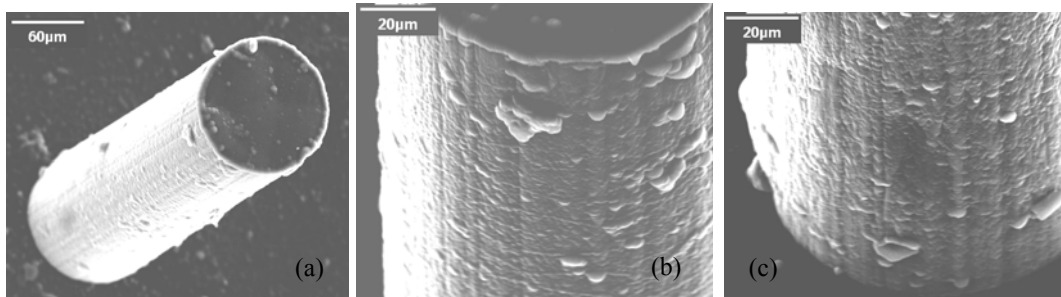
## Results and Discussion

Fig. 5.2(a) shows a low magnification SEM micrograph of a typical as-fabricated Ni insert, consisting of a field of cylindrical microposts, 500  $\mu\text{m}$  in height and 100  $\mu\text{m}$  in diameter. The post-to-post spacing of this particular insert is 700  $\mu\text{m}$ . Figures 5.2(b) and (c) show, at higher magnification, one micropost close to the top and bottom, respectively. The striations parallel to the post direction as well as the finer markings along the circumferential direction are typical of the LIGA fabrication process, and may reflect the surface relief features on the PMMA resist after X-ray exposure.



**Fig. 5.2 SEM micrographs of a Ni mold insert in the as-fabricated condition: (a) low-magnification view of a field of cylindrical microposts, (b) sidewall near the post top, (c) sidewall near the intersection of the post and the Ni base. The micropost diameter is 100  $\mu\text{m}$  and the post-to-post spacing is 700  $\mu\text{m}$**

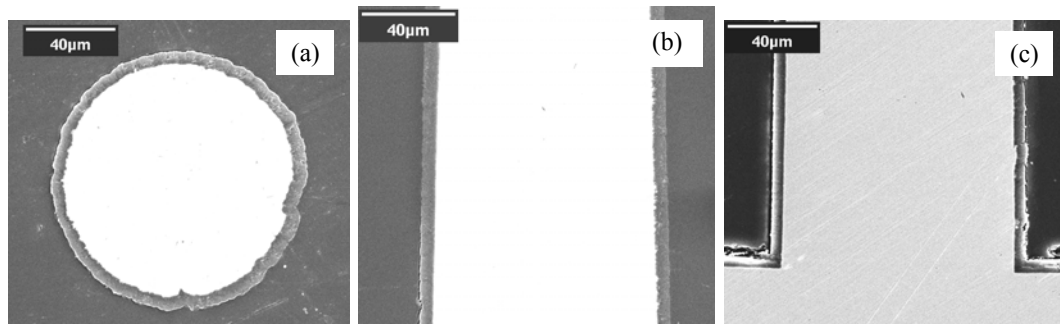
Fig. 5.3(a) shows one micropost on the insert after Ti-C:H deposition. Fig. 5.3(b) and (c) show respectively views of one micropost close to the top and bottom. While some remnant striations along the micropost direction are still visible, the finer markings along the post circumferential direction have disappeared due to Ti-C:H coverage. The surface morphology, consisting of nodules 10  $\mu\text{m}$  or less in size together with submicron undulations, is typical of plasma deposited Ti-C:H coatings<sup>7</sup>.



**Fig. 5.3 SEM micrographs of a Ti-C:H coated Ni mold insert in the as-coated condition: (a) low-magnification view of one micropost, (b) sidewall near the post top, (c) sidewall near the intersection of the post and the Ni base. The micropost diameter is 100  $\mu\text{m}$  and the post-to-post spacing is 700  $\mu\text{m}$**

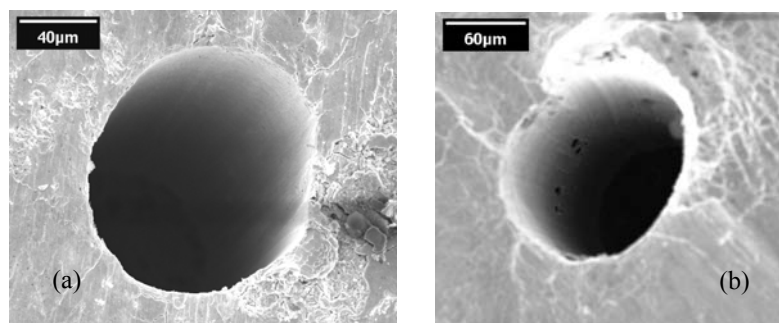


Fig. 5.4 shows cross-sectional SEM micrographs obtained from one micropost of the Ti-C:H coated insert. Cross sections perpendicular to the post, parallel to the post close to the middle section, and parallel to the post at the intersection between the post and the Ni base, shown respectively in Figures 4.4(a), 4.4(b), and 4.4(c), clearly demonstrate conformal Ti-C:H coverage of the microposts and the Ni base surface between the microposts, including the micropost/Ni base intersections.

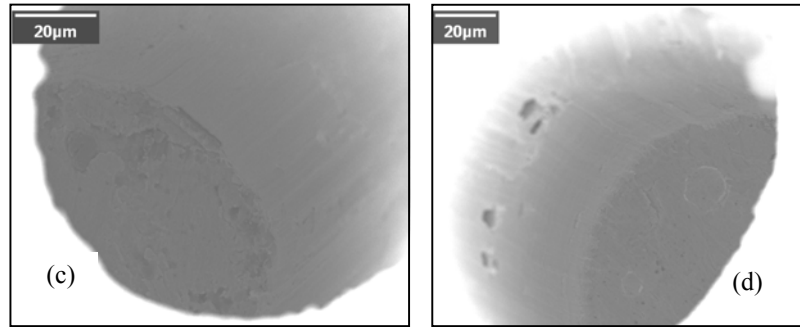


**Fig. 5.4 Cross-sectional SEM micrographs of Ti-C:H coated cylindrical microposts: (a) perpendicular to a micropost; (b) center section parallel to a micropost; (c) parallel to a micropost at the intersection between the post and the Ni base**

Microholes were created in the Pb plate by compression molding with uncoated and Ti-C:H coated Ni inserts. The uncoated and Ti-C:H coated inserts both consisted of fields of cylindrical microposts 100 µm in diameter and 500 µm in height. The post-to-post spacings for the uncoated and Ti-C:H coated inserts were 500 and 400 µm, respectively. Figures 5.5(a) and (b) show one microhole within a field of microholes on Pb plates molded with the uncoated insert and the Ti-C:H coated insert, respectively. Fig. 5.5(c) and (d) show views of the respective hole interiors, with relatively smooth sidewalls and sharp bottom to sidewall transitions. In both cases, full molding was achieved, with the depths of the microholes approximately equal to the height of the microposts on the insert.

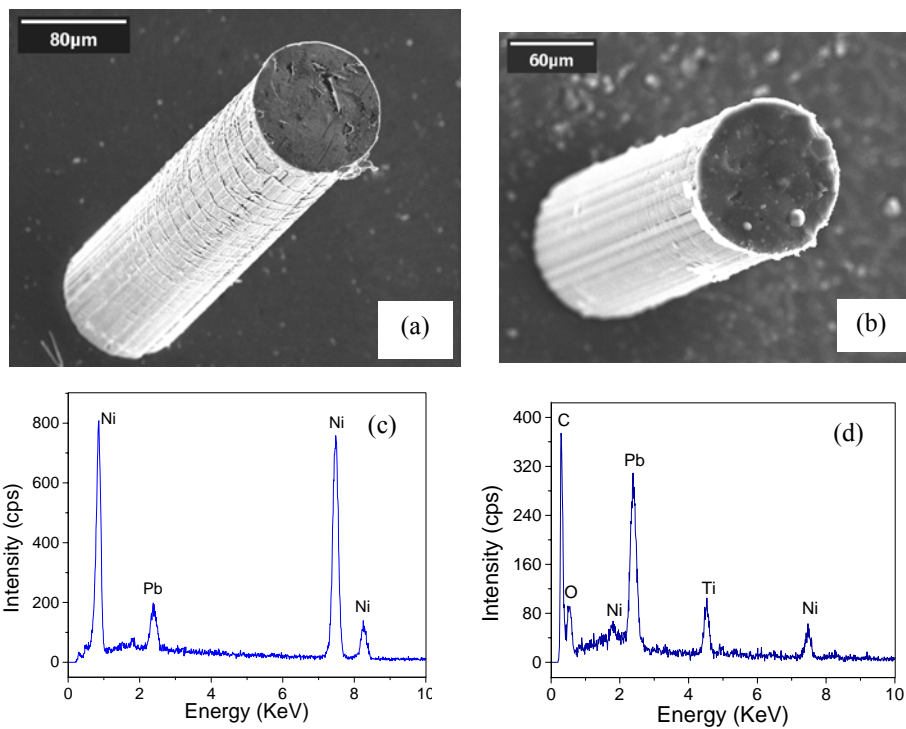


**Fig. 5.5 SEM micrographs of molded microholes in Pb: (a) one microhole molded by an uncoated Ni insert; (b) one microhole molded by a Ti-C:H coated Ni insert**



**Fig. 5.5 (Continued)** (c) the hole interior molded by the uncoated Ni insert, (d) the hole interior molded by the Ti-C:H coated Ni insert. The micropost diameters for both inserts were 100  $\mu\text{m}$ . The post-to-post spacing for the uncoated and Ti-C:H coated inserts was 500 and 400  $\mu\text{m}$ , respectively

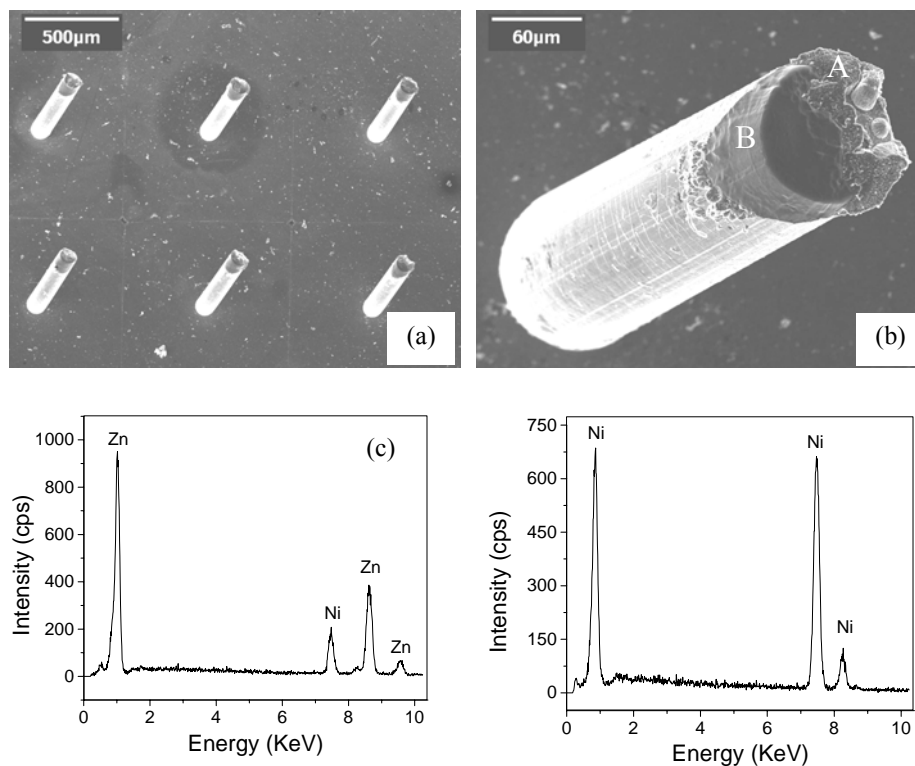
Fig. 5.6(a) and 5.6(b) show one typical micropost within a field of microposts on the uncoated insert and the Ti-C:H coated insert after Pb molding, respectively. In both cases, there is neither significant damage to nor significant Pb transfer on any of the microposts.



**Fig. 5.6** Condition of uncoated and Ti-C:H coated mold inserts after molding Pb: (a) a single micropost showing the sidewall and the top rim of an uncoated Ni insert, (b) a single micropost showing the sidewall and the top rim showing the sidewall and the top rim of a Ti-C:H coated Ni insert, (c) an EDS spectrum collected from the area close to the post top rim of the uncoated insert, (d) an EDS spectrum collected from the area close to the post top rim of the Ti-C:H coated insert

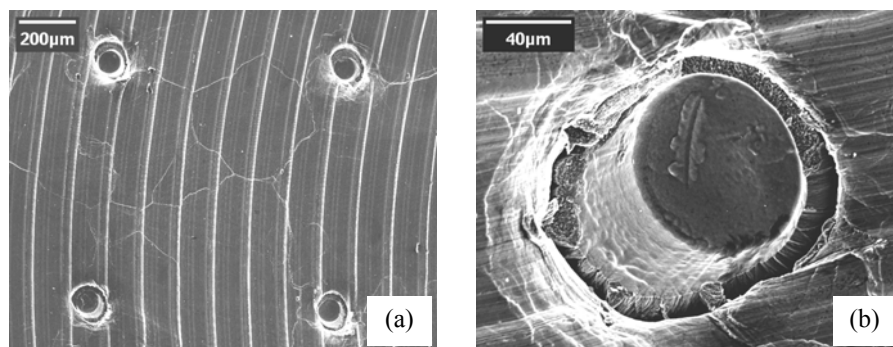
Fig. 5.6(c) and 5.6(d) show respectively an EDS spectrum acquired from an area close to the micropost top rim of the uncoated insert and the Ti-C:H coated insert, indicating some Pb pickup around the micropost top rim in both cases. Repeated molding cycles did not cause any noticeable change or degradation of the uncoated and the Ti-C:H coated inserts.

A contrasting situation is provided by Zn micromolding. Fig. 5.7(a) shows a low-magnification view of an array of microposts on an uncoated Ni insert after molding Zn. The micropost diameter is 100  $\mu\text{m}$  and the post-to-post spacing is 800  $\mu\text{m}$ . Fig. 5.7(b) shows a magnified view of one micropost, including the post sidewall and top rim regions. In contrast to Pb molding, significant material pickup (area A) and damage to the post top region (area B) were observed on *every* Ni micropost. Fig. 5.7(c) shows an EDS spectrum collected from area A shown in Fig. 5.7(b), indicating that the protrusion consists mostly of Zn. Fig. 5.7(d) shows an EDS spectrum from area B shown in Fig. 5.7(b), indicating no presence of Zn. It appears that area B was exposed Ni after a piece of the original Ni micropost was torn away during the demolding process, after it reacted with the Zn metal.



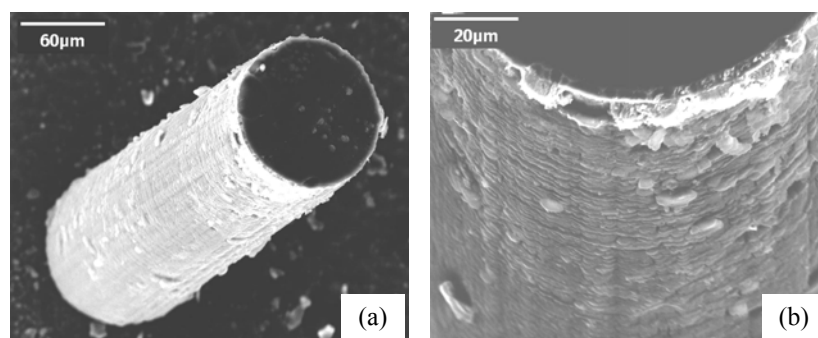
**Fig. 5.7 Condition of uncoated Ni insert after molding Zn: (a) a low-magnification view of an array of microposts, (b) a single micropost showing the micropost sidewall and top rim regions, (c) an EDS spectrum from area A on the micropost top showing Zn pickup, (d) an EDS spectrum from area B showing no Zn. The micropost diameter is 100  $\mu\text{m}$  and the post-to-post spacing is 800  $\mu\text{m}$**

Fig. 5.8(a) shows a low magnification view of several microholes in the Zn plate molded by the uncoated Ni insert. Fig. 5.8(b) shows the interior of one microhole. Due to the limited molding temperature and load, only partial molding was achieved. In contrast to the Pb case, molding of Zn with uncoated Ni inserts lead to the presence of significant disruptions on the microhole sidewall surface. These disruptions are believed to be related to the significant amount of Zn transfer to the top of the uncoated Ni microposts. Fig. 5.7 and 5.8 suggest that Zn reacted with the uncoated Ni microposts during the molding process, which lead to damage of micropost, significant Zn transfer on the micropost, and microhole sidewall disruptions. This shows that uncoated Ni inserts would not be sufficient for Zn molding since these problems would be exacerbated after repeated molding cycles.



**Fig. 5.8 SEM micrographs of microholes in Zn molded by the uncoated Ni insert: (a) a low-magnification view of several microholes; (b) a magnified view of the interior of one microhole showing sidewall disruptions**

Fig. 5.9(a) and (b) show one micropost on a Ti-C:H coated Ni mold insert after embossing Zn and a magnified view of the post top rim region, respectively. In contrast to Zn molding with the uncoated Ni insert, the Ti-C:H coated insert shows little damage to the post top region or Zn pickup. Fig. 5.9(c) shows a representative EDS spectrum from the majority of the micropost area, indicating no Zn transfer. Fig. 5.9(d) shows an EDS spectrum collected from the post top rim region, showing some Zn transfer. The



**Fig. 5.9 Condition of Ti-C:H coated Ni insert after molding Zn: (a) a SEM image of a single micropost; (b) micropost sidewall close to the top rim**

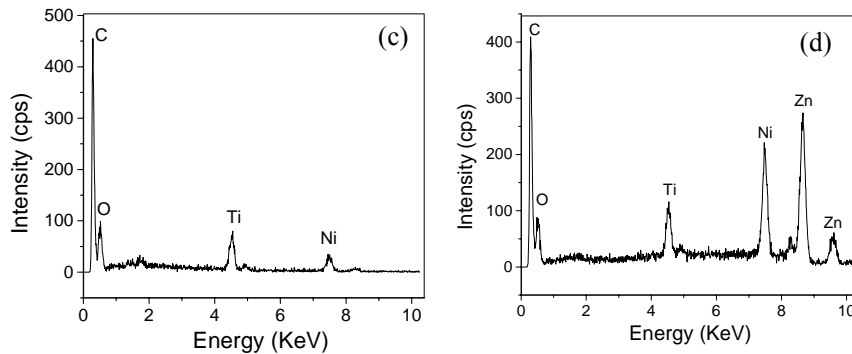


**Fig. 5.9 (Continued) (c) a representative EDS spectrum from the majority of the micropost area shows no Zn pickup; (d) an EDS spectrum collected from the post top rim region showing some Zn pickup**

presence of oxygen signal in the EDS spectra may signal some coating oxidation. Fig. 5.6 and 5.9 show that conditions of Ti-C:H coated Ni inserts after molding Pb and Zn are similar, with essentially no damage to the inserts and little material pickup.

Fig. 5.10(a) shows a low-magnification view of several microholes in Zn molded by the Ti-C:H coated insert. Fig. 5.10(b) shows the interior of one microhole, showing relatively smooth sidewalls. Again, only partial molding of Zn was achieved, due to the current limitations on temperature and compression load. Nevertheless, Fig. 5.9 and 5.10 indicate that Ti-C:H coated Ni mold inserts is effective for molding Zn, due to the fact that the Ti-C:H coating on the Ni microposts acts as a barrier to reactions between the Ni microposts and the Zn plate.

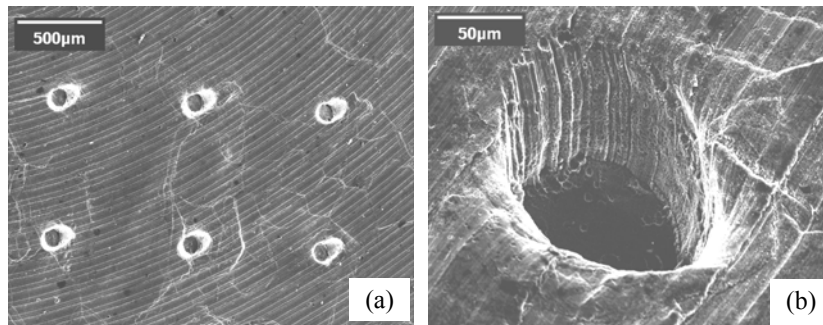


**Fig. 5.10 SEM micrographs of micro-holes in Zn molded by the Ti-C:H coated insert: (a) a low-magnification view of several microholes, (b) a magnified view of the interior of one microhole showing relatively smooth sidewalls**

Post-molding examinations shown in Fig. 5.5 and 5.6 indicate that, for Pb molding, uncoated and Ti-C:H coated inserts exhibit similar performance, both in terms of feature generation on the Pb plate and insert integrity after molding. Both uncoated and Ti-C:H coated inserts appear to separate readily from the Pb plate in the demolding step. EDS analysis illustrated that most of insert features were Pb free after a few molding cycles.

Similar examinations shown in Fig. 5.7 to 5.10 indicate that, for Zn molding, Ti-C:H coated inserts exhibit clearly improved performance. The absence of reaction between Pb and the uncoated Ni insert and the presence of significant reaction between Zn and the uncoated Ni insert can be readily understood considering that the heats of mixing of Ni-Pb and Ni-Zn alloys have been estimated to be +2 kJ/mol and -23 kJ/mol, respectively<sup>13</sup>. Pb and Ni are immiscible in both the solid and liquid states, while Zn and Ni form several intermetallic compounds in the solid state and are completely miscible in the liquid state<sup>14</sup>. The presence of the Ti-C:H coating on the Ni insert alters the Zn/insert chemical interaction, leading to the improved molding performance. In both Pb and Zn molding, material pickup observed around the micropost top rim regions was related to the presence of a slight lip resulting from the LIGA fabrication process, and can be eliminated with improved LIGA fabrication procedures.

For a soft metal such as Pb, in the absence of metal/insert chemical interaction, the present results indicate that surface modification of the Ni insert is not necessary to achieve Pb micromolding. In the case of Zn, where significant metal/insert chemical interactions exist, surface modification of the Ni insert is clearly needed to achieve Zn micromolding. In addition to altering the metal/insert chemical interactions, optimal temperature-time histories remain to be determined to improve molding performance. After repeated molding cycles, crack-like features appeared on the Ti-C:H coating in the Ni base area between microposts, presumably due to thermal expansion mismatch between Ti-C:H and the underlying Ni substrate. Failures of the coating/insert system, such as coating cracking, spalling, and wear, critically affect the lifetime of coated inserts. Detailed understanding of mechanisms controlling such failures is critical to the success of using coated inserts for micromolding of metals, and is a subject of intense currently interest.

## Summary

A comparative study of micromolding of Pb and Zn metals at 300 °C with uncoated and Ti-C:H coated Ni microscale mold inserts fabricated by the LIGA technique has been carried out. Molding performance has been characterized by detailed examinations of feature generation on the metal plates and inserts condition after molding. Current results show that successful Pb micromolding can be achieved with both uncoated Ni inserts and Ti-C:H coated Ni inserts, while Ti-C:H coated Ni inserts are necessary for Zn micromolding. The difference in molding performance can be understood by considering the difference between the thermodynamics of Ni-Pb and Ni-Zn systems, and show that altering the metal/insert chemical interactions is a key element for successful micromolding of reactive metals. The present study suggests that, with an improved temperature-time history, conformal deposition of Ti-C:H coatings onto Ni inserts will lead to full molding of Zn. Design and synthesis of suitable nanostructured ceramic coatings for surface engineering of LIGA fabricated microscale mold inserts require further understanding of the complex chemical/mechanical interactions between the insert and the molded metal, and is being actively pursued.

## References

- 1 E. W. Becker, W. Ehrfeld, P. Hagmann, A. Manner, and D. Munchmeyer, Fabrication of Microstructures with Extreme Structural Heights by Synchrotron Radiation Lithography, Galvanoforming and Plastic Moulding (LiGA Process), *Microelectron. Eng.*, 4, (1986) pp.35-56
- 2 Maner, S. Harsh, W. Ehrfeld, Plating and Surface Finishing, pp 60-65, March 1988
- 3 C. Harris, M. Despa, K. W. Kelly, Design and Fabrication of a Cross Flow Micro Heat Exchanger, *IEEE J. MEMS.* 9, (2000) pp.502-508
- 4 L. S. Stephens, K. W. Kelly, D. Kountouris, J. McLean, A pin fin microheat sink for cooling macroscale conformal surfaces under the influence of thrust and frictional forces, *IEEE J. MEMS*, 10 (2), (2001) pp. 222-231
- 5 L. Weber, W. Ehrfeld, H. Freimuth, M. Lacher, H. Lehr, B. Pech, *SPIE Proceeding, Micromachining and microfabrication Process Technology II*, Austin, Texas, U.S.A., (1996), pp. 156
- 6 S. Gopal, A. Lakare, R. Shivpuri, Soldering in die casting: Aluminum alloy and die steel interactions, *Die Casting Engineering*, 44(3), (2000) pp. 70-81
- 7 D. M. Cao, T. Wang, B. Feng, W. J. Meng, K. W. Kelly, Amorphous hydrocarbon based thin films for high-aspect-ratio MEMS application, *Thin Solid Films* 398/399, (2001) pp. 553-559
- 8 W. J. Meng, R. C. Tittsworth, J. C. Jiang, B. Feng, D. M. Cao, K. Winkler, V. Palshin, Ti atomic bonding environment in Ti-containing hydrocarbon coatings, *J. Appl. Phys.*, 88 (5), (2000) pp.2415-2422
- 9 D. M. Cao, B. Feng, W. J. Meng, L. E. Rehn, P. M. Baldo, M. M. Khonsari, Friction and Wear Characteristics of Ceramic Nanocomposite Coatings: Titanium Carbide/Amorphous Hydrocarbon, *Appl. Phys. Lett.* 79 (3), (2001) pp. 329-331
- 10 B. Feng, D. M. Cao, W. J. Meng, L. E. Rehn, P. M. Baldo, G. L. Doll, Probing for mechanical and tribological anomalies in the TiC/amorphous hydrocarbon nanocomposite coating system, *Thin Solid Films*, 398/399, (2001) pp. 210-216
- 11 W. J. Meng, T. J. Curtis, Inductively coupled plasma assisted physical vapor deposition of titanium nitride coatings, *J. Electronic Materials*, 26 (11), (1997) pp. 1297-1302
- 12 W. J. Meng, T. J. Curtis, L. E. Rehn, P. M. Baldo, Temperature dependence of inductively coupled plasma assisted deposition of titanium nitride coatings, *Surf. Coat. Technol.* 120/121, (1999) pp. 206-212

- 13 A. R. Miedema, Heat of Formation of Alloys, Philips Tech. Rev., 36(8), (1976) pp. 217-231
- 14 T. B. Massalski (ed.), Binary Alloy Phase Diagrams, ASM International (1990)



## CHAPTER 6. HIGH-TEMPERATURE INSTRUMENTED MICROSCALE COMPRESSION MOLDING OF Pb<sup>\*</sup>

### Introduction

In the arsenal of microfabrication technologies, the LiGA (Lithographie, Galvanoformung, Abformung) technique, based on deep X-ray lithography and electrodeposition<sup>1</sup>, is unique in its ability to make high aspect ratio microscale structures (HARMS). Due to the high cost of synchrotron radiation and the slow speed of electrodeposition, metal HARMS made from electrodeposition into deep resist structures made by X-ray lithography are very expensive. Therefore the molding (Abformung) step of LiGA holds the key to economical production of HARMS based micro devices. Currently, little effort on replication of *metallic* HARMS by compression molding with LiGA fabricated inserts is reported in the literature.

One major obstacle to high-temperature microscale compression molding of metals is the chemical/mechanical interactions between the hot metal and the insert. These interactions can result in insert/metal bonding and lead to insert damage, inadequate feature definition on the molded metal, or both. We have previously shown that modifying the insert near-surface chemical/mechanical/tribological properties by applying a conformally deposited ceramic coating can enable micromolding of reactive metals such as Zn with Ni inserts<sup>2</sup>. In cases where no chemical interaction exists between the insert and the hot metal, such as Pb and Ni<sup>3</sup>, surface modification of the Ni insert is not necessary.

In addition to surface chemical/mechanical interactions, bulk mechanical properties of LiGA fabricated microscale mold inserts need to be considered. Ni has commonly been used to build LiGA based HARMS. The Ni electrodeposition (Galvanoformung) process typically leads to the formation of a nanocrystalline structure. Upon heating to higher temperatures, extensive structural evolution occurs within the electrodeposited Ni<sup>4</sup>, leading to a significant decrease of its yield strength, from ~370MPa in the as-deposited condition to ~140MPa after annealing to 400°C<sup>5</sup>. If contact stresses during micromolding exceed the yield strength of the Ni insert at the molding temperature, plastic deformation of the insert is expected, which will lead to insert deformation and loss of shape definition. Despite these concerns, little information on stresses needed for high-temperature microscale compression molding of metals and subsequent insert extraction is available in the current literature.

In this chapter, high-vacuum, high-temperature instrumented micromolding of Pb with LiGA fabricated Ni inserts is reported. The ability to monitor the molding force, insert extraction force, and insert displacement during the micromolding process allowed to quantitatively measure the molding normal stress, demolding friction stress, and mechanical work needed for Pb micromolding as a function of temperature. The results show that, in cases where surface chemistry is favorable, present LiGA fabricated Ni inserts are adequate for micromolding of low melting temperature metals.

---

<sup>\*</sup> Reprinted from Microsystem Technologies with the permission of Springer-Verlag

## Experimental

Ni microscale mold inserts, consisting of fields of cylindrical microposts 400  $\mu\text{m}$  in height and diameter ranging from 100 - 200 $\mu\text{m}$ , were fabricated with the LiGA technique using the synchrotron facility at the Louisiana State University Center for Advanced Microstructures and Devices (LSU CAMD). Further details about the X-ray mask fabrication, X-ray exposure, resist pattern development, and Ni electrodeposition have been reported previously<sup>2-6</sup>. Post-to-post spacing ranged from 400 - 800 $\mu\text{m}$ . All Ni inserts were cleaned in acetone and methanol prior to being used to compression mold Pb plates. Pb plates (99.9%) were in the form of circular disks with 1.4 inches in diameter and 0.25 inch in thickness. Pb plate surfaces were mechanically polished with SiC abrasive papers from 400 to 1000 in grit size prior to being molded.

Instrumented micromolding was carried out using a single-axis MTS858 Mini-Bionix II© testing system interfaced to a custom-built high-vacuum chamber. As shown in Fig. 1(a), the testing system included a hydraulically powered, cross-head-mounted, linear actuator, and a TestStar© digital controller capable of controlling either the load force or the actuator displacement. The linear actuator could be programmed to move according to prescribed load forces in the force-controlled mode or actuator displacements in the displacement-controlled mode. The axial force was measured by a 5kN full-scale load cell with a resolution of  $\sim 5\text{mN}$ , and the axial displacement was measured by a linear variable displacement transducer (LVDT) with a resolution of  $\sim 0.5\mu\text{m}$ . The entire molding/demolding process was programmed through the TestStar software and controlled through the TestStar digital controller.

A high-vacuum molding chamber, shown in Fig. 1(b), and two heating stations within, were custom-built for the high-temperature micromolding experiment. The Pb plate to be molded was fixed on the lower heating station, mechanically attached to the bottom of the vacuum chamber. The Ni microscale mold insert was mechanically attached to the upper heating station, which was connected to the linear actuator through a Z-motion manipulator shown in Fig. 1(a). Each heating station was heated by three 120V/300W heating cartridges. Temperatures of the two heating stations were varied independently through separate input voltages into the heating cartridges. Insert and Pb plate temperatures were measured by two separate K-type thermocouples connected to a Stanford Research Systems SR630 16-channel thermocouple monitor. Temperature – time histories were recorded on a computer through an interface to the thermocouple monitor. Pumped by a turbomolecular pumping system, the ultimate base-pressure of the molding chamber was below  $1 \times 10^{-8}$  Torr. All Pb micromolding experiments were performed at pressures below  $\sim 2 \times 10^{-7}$  Torr at the final molding temperature.

The entire micromolding process was divided into five segments: 1) a displacement-controlled approach with a force limit; 2) a force-controlled molding with a displacement limit; 3) a constant force hold; 4) a displacement-controlled demolding; 5) a constant displacement final hold. The initial approach segment was executed with a constant displacement rate of 1mm/min. Before insert/Pb contact, a small compression force,  $\sim -12\text{N}$ , arose from compression of the Z-motion manipulator bellows. In the approach segment, a force limit of  $-30\text{N}$  was therefore set to trigger the initiation of the second segment, ensuring insert/Pb contact. In the molding segment, a constant loading rate of 100N/min was used together with a displacement limit of 500 $\mu\text{m}$  to ensure full molding

by the 400 $\mu$ m tall Ni insert and trigger the initiation of the third segment. After a constant-force hold for five minutes, the Ni insert was withdrawn 6mm at a constant displacement rate of 1mm/min, ensuring full demolding. The demolding segment was followed by the final hold segment. Using one Ni insert, the same micromolding process was repeated on a series of Pb plates heated to temperatures ranging from  $\sim 120^{\circ}\text{C}$  to  $\sim 270^{\circ}\text{C}$ . The corresponding Ni insert temperatures were controlled to be within  $\sim 5^{\circ}\text{C}$  of the Pb plate temperature. Demolding occurred at the same temperature as in the molding process. In addition, at the Pb plate temperature of  $\sim 200^{\circ}\text{C}$ , the influence of three different loading rates in the molding segment, 33.33N/min, 100N/min and 300N/min, on the maximum molding force were studied. At the Pb plate temperature of  $\sim 175^{\circ}\text{C}$ , the influence of three different insert withdrawal rates, 0.2mm/min, 1.0mm/min and 5.0mm/min, on the maximum demolding force was also studied. Scanning Electron Microscopy (SEM) examinations of the molded features in Pb and the Ni insert condition after molding were carried out on a JEOL 840A microscope.

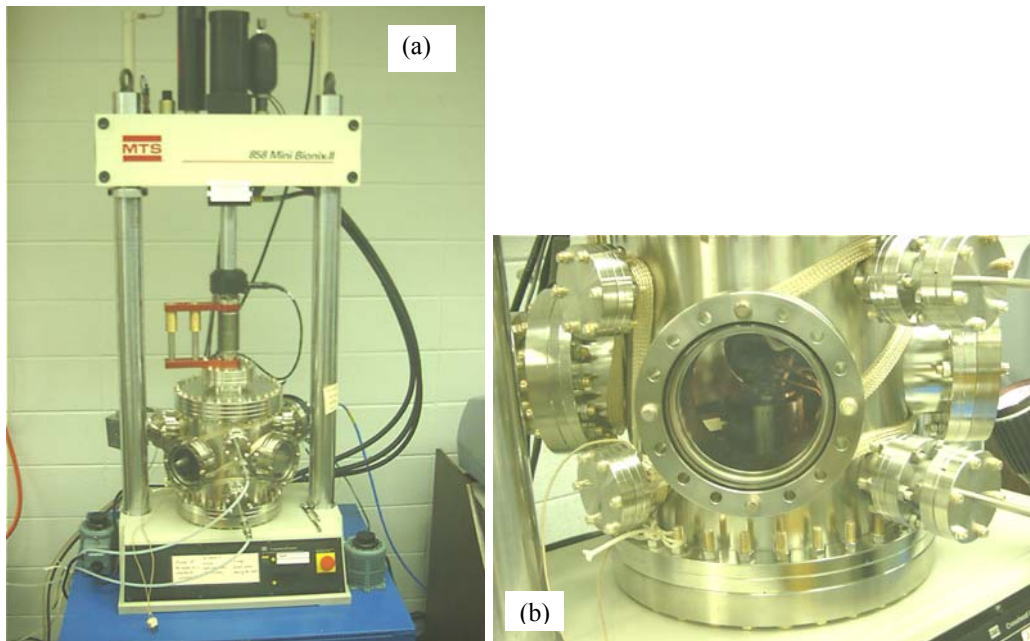


**Fig. 6.1 The custom-built, high-vacuum, high-temperature compression-molding machine: (a) an overview of the system layout; (b) a close-up view of the high-vacuum chamber. The bottom heating station is visible through the view port**

## Results and Discussion

Fig. 6.2(a) shows an optical micrograph of a Pb plate after being compression molded by a microscale Ni insert at  $256^{\circ}\text{C}$ . The Ni insert contains 585 Ni microposts, 150 $\mu$ m in diameter, arranged in a square array with a post-to-post spacing of 650 $\mu$ m. The imprints of four Ni support pads, located at the four corners of the square-shaped insert, are also clearly visible on the Pb plate. Each Ni support pad is at the same height as the

Ni microposts, and contains a threaded hole in the middle through which the insert was threaded to the upper heating station. No contact of the securing screws and the Pb plate took place during molding. Fig. 6.2(a) shows that features on the Ni insert were transferred in entirety to the Pb plate. Fig. 6.2(b) shows a SEM micrograph of the same Pb plate, clearly showing the presence of an array of sharply defined microholes.

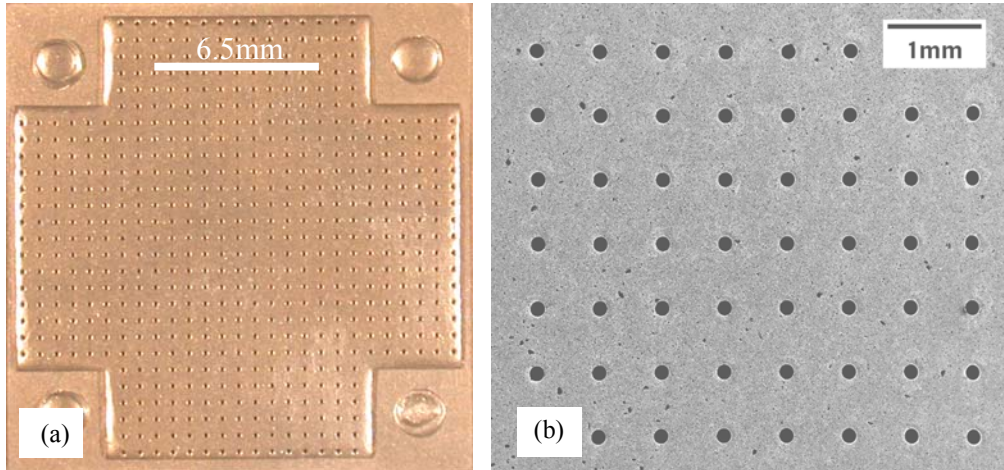


**Fig. 6.2** A Pb plate after micromolding by a LiGA Ni insert at 256°C: (a) an optical micrograph showing the entire molded Pb piece; (b) a SEM micrograph showing an array of microholes generated. The microhole diameter is 150 $\mu$ m and the hole-to-hole spacing is 650 $\mu$ m

Fig. 6.3(a) and (b) show respectively the insert displacement and the total force on the linear actuator as a function of time during one entire Pb micromolding run at 118°C.

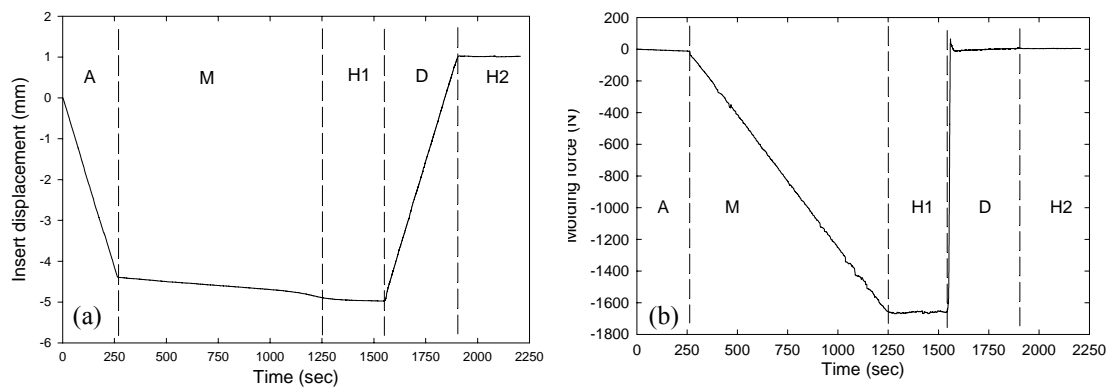


**Fig. 6.3** Output signals from a Pb micromolding run at 118°C: (a) insert displacement vs. time; (b) total force on the actuator vs. time. The approach (A), molding (M), constant-force hold (H1), demolding (D), and constant-displacement hold (H2) segments of the micromolding process are delineated by dashed lines

During the approach segment, the slight increase in compression force due to insert movement,  $\sim -3\text{N/mm}$ , reflects the compression of the Z-motion manipulator bellow. During the molding segment, while the compression force increases with a prescribed rate of  $-100\text{N/min}$ , the insert displacement appears to be also varying linearly with time. After the constant force hold segment, the initial insert withdrawal led to a rapid change in the total force from a compressive to a tensile one. With continued insert withdrawal, the tensile force is seen to reach a maximum, and then decrease to a slowly varying background level. This background force changes with insert displacement at a rate of  $\sim +3\text{N/mm}$ , and reflects the stretching of the Z-motion manipulator bellow. The excess tensile force above this background measures the maximum force on the insert due to demolding friction. During the final hold segment, neither insert displacement nor force changes with time.

Fig. 6.4(a) shows the force – displacement curve corresponding to micromolding of Pb at  $118^\circ\text{C}$ , extracted from the molding segment data shown in Fig. 6.3. The compressive molding force appears to be approximately linear with molding depth, and the area under the force – displacement curve reflects the total amount of work spent in the molding process. Experiments done at other temperatures likewise showed approximately linear force – displacement curves. Fig. 6.4(b) shows the total work of molding as a function of the Pb temperature, where the molding work is observed to decrease significantly with increasing temperature, from  $\sim 300\text{Nmm}$  at  $\sim 120^\circ\text{C}$  to  $\sim 100\text{Nmm}$  at  $\sim 270^\circ\text{C}$ . Correspondingly, the maximum compressive molding force is shown as a function of the Pb temperature in Fig. 6.4(c), where a similar three-fold decrease in the magnitude of the compression force from  $\sim 1500\text{N}$  at  $\sim 120^\circ\text{C}$  to  $\sim 500\text{N}$  at  $\sim 270^\circ\text{C}$  is observed. As expected from the approximately linear nature of the force – displacement curves, the ratio of molding work and maximum molding force, as shown in Fig. 6.4(d), is approximately  $200\mu\text{m}$ , independent of the molding temperature.

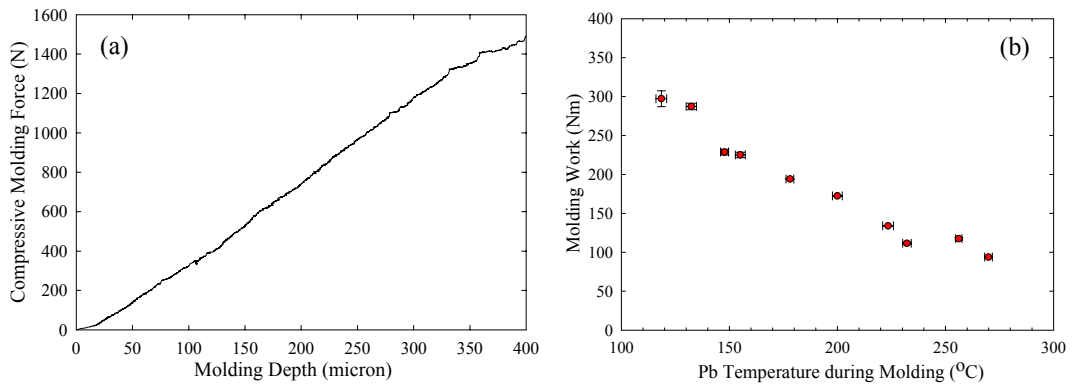


**Fig. 6.4 Quantitation of the micromolding process: (a) the load – displacement curve during the molding segment of a Pb micromolding run at  $118^\circ\text{C}$ ; (b) total work of molding as a function of the Pb temperature**

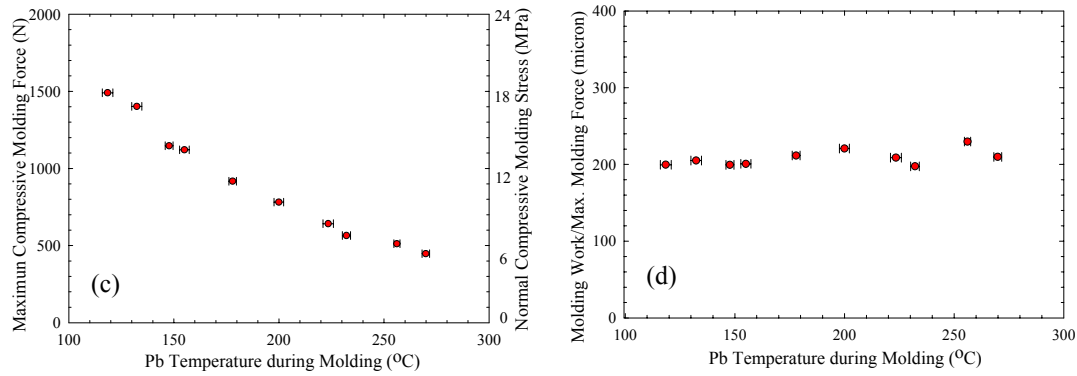


**Fig. 6.4 (Continued) (c) the maximum normal compressive molding force/stress as a function of the Pb temperature; (d) the ratio of the total molding work to the maximum compressive molding force**

The quantitative measurement of the maximum molding force can be converted to a maximum normal compressive stress on the Ni microposts. The calculated result, taking into account the entire area of contact, is shown on the right hand side force axis in Fig. 6.4(c). At the lowest molding temperature of  $\sim 120^{\circ}\text{C}$ , the maximum molding force corresponds to a maximum normal compressive stress of  $\sim 18\text{MPa}$ . This is significantly below the measured yield stress of microscale electrodeposited Ni specimens heated to  $\sim 400^{\circ}\text{C}$ ,  $\sim 140\text{MPa}$ <sup>5</sup>, and shows that the electrodeposited Ni inserts should possess adequate strength for Pb micromolding.

The portion of the force – time curve shown in Fig. 6.3(b) corresponding to the demolding segment is shown in more detail in Fig. 6.5(a). While the insert was continuously withdrawn from the molding Pb plate, the total force rapidly changes from

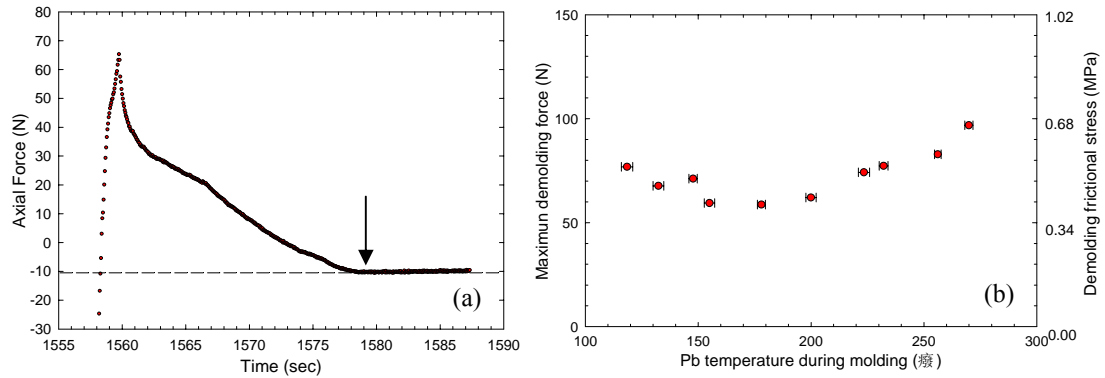


**Fig. 6.5 Quantitation of the demolding process: (a) a section of the force – time data during the insert withdrawal segment of a Pb micromolding run at  $118^{\circ}\text{C}$ . The background delineated by the dashed line corresponds to a slope of  $\sim 3\text{N/mm}$  and reflects the stretching of the manipulator bellow; (b) the maximum demolding friction force/stress as a function of the Pb temperature**

compression to tension, and reaches a maximum in tension at  $\sim 1560$ sec. The decrease of the maximum tensile force to the slowly varying background occurred in  $\sim 20$ sec after the maximum tensile force was reached, corresponding to a distance of further insert withdrawal of  $\sim 333\mu\text{m}$  at a displacement rate of  $1\text{mm/min}$ . Considering the total height of Ni microposts of  $400\mu\text{m}$ , it can be seen that the maximum demolding force was reached close to the point where the microposts had full side contact with Pb. The slowly varying background force, shown in Fig. 6.5(a) from  $\sim 1580$ sec to  $\sim 1587$ sec, corresponds to a slight decrease in compression force with further insert withdrawal,  $\sim +3\text{N/mm}$ . The difference between the maximum tensile force and the extrapolated background measures the maximum demolding force experienced during the insert withdrawal process. Fig. 6.5(b) shows the maximum demolding force as a function of the Pb temperature. Using the entire micropost side area, the measured maximum demolding force was converted into a maximum frictional stress during demolding. The demolding friction stress is shown on the right hand side of the demolding force axis in Fig. 6.5(b), where it is evident that it exhibits a smooth variation with molding temperature, and is on average  $\sim 0.5\text{MPa}$ .

Features generated on the Pb plate by micromolding are illustrated in Fig. 6.6 and Fig. 6.7. Figure 6.6(a) shows a close-up view of the top surface of one microhole in a Pb plate molded at  $256^\circ\text{C}$ . A view of the corresponding microhole interior is shown in Fig. 6.6(b), where the relatively smooth sidewall and the sharp sidewall to bottom transition are evident. Depth measurements by optical interference microscopy showed that the depth of microholes were  $\sim 400\mu\text{m}$ , demonstrating that 100% micromolding was achieved.

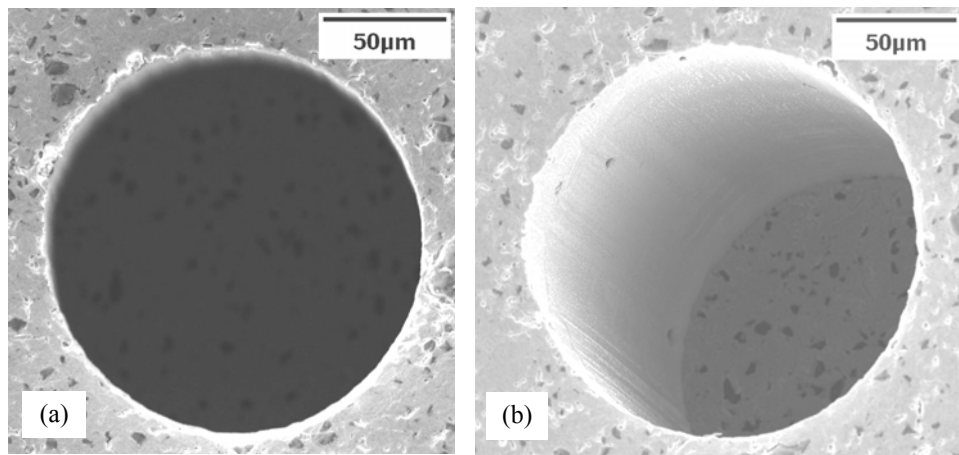


**Fig. 6.6 Examination of microholes generated in Pb by micromolding at  $256^\circ\text{C}$ : (a) a SEM micrograph of the top surface of a microhole; (b) a SEM micrograph of the microhole interior**

Fig. 6.7(a) and (b) show respectively the views of one microhole top surface and the microhole interior on one Pb specimen molded at  $118^\circ\text{C}$ . Although well-defined microholes were generated by micromolding at  $118^\circ\text{C}$ , comparison between Fig. 6.6(b)



and Fig. 6.7(b) revealed rougher sidewall morphologies of the microhole molded at 118°C. Thus while sharp geometric features can be generated by micromolding in the entire temperature range of ~120°C to ~270°C, the choice of an optimum molding temperature needs to take into account the molding and demolding forces required, as well as surface morphologies of the generated microscale features.

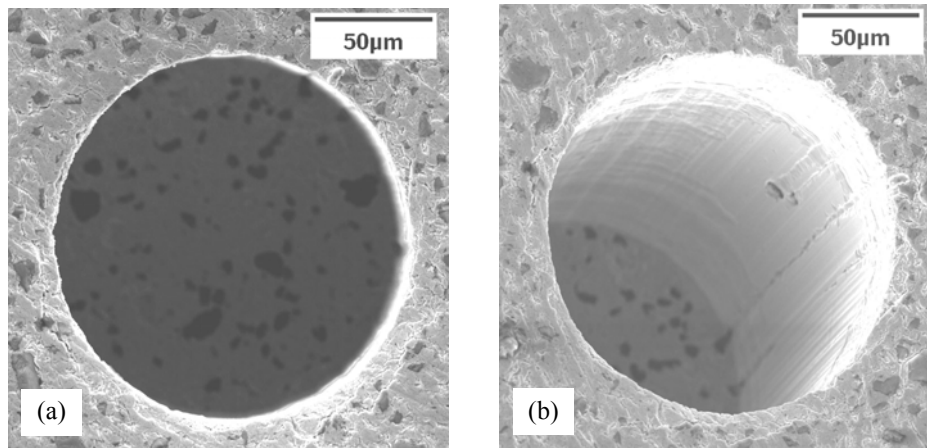


**Fig. 6.7 Examination of microholes generated in Pb by micromolding at 118°C: (a) a SEM micrograph of the top surface of a microhole; (b) a SEM micrograph of the microhole interior**

Table 6.1 shows the influence of the prescribed loading rate in the molding segment of Pb micromolding on the maximum compressive molding force. Holding the Pb temperature at ~200 °C and all other process parameters constant, data shown in Table 1 shows that changing the loading rate from 33.33N/min to 100N/min led to a slight increase of the maximum compressive molding force from 642N to 783N. No further change in the maximum compressive molding force was observed when the loading rate was further increased from 100N/min to 300N/min. The maximum demolding friction forces showed no systematic variation with the loading rate.

**Table 6.1. Influence of the loading rate on the maximum compressive molding force**

Pb Temperature (°C)	Loading Rate (N/min)	Maximum Compressive Molding Force (N)	Maximum Demolding Friction Force (N)
205	33.33	642	74
200	100.0	781	62
203	300.0	783	72

Table 6.2 shows the influence of the demolding rate on the maximum demolding friction force. Holding the Pb temperature at ~175 °C and all other process parameters constant, data shown in Table 2 shows that changing the insert withdrawal rate from 0.2mm/min to 5.0mm/min does not seem to have a significant influence on the maximum



demolding friction force. The variation of the maximum compressive molding force shown in Table 2 is typical of the Pb micromolding experiments.

**Table 6.2. Influence of the demolding rate on the maximum demolding friction force**

Pb Temperature (°C)	Demolding Rate (mm/min)	Maximum Compressive Molding Force (N)	Maximum Demolding Friction Force (N)
177	0.2	989	72
178	1.0	917	59
173	5.0	995	66

The condition of the Ni insert after repeated Pb micromolding runs is illustrated in Fig. 6.8. Fig. 6.8(a) shows that essentially no damage is visible on any of the Ni microposts. A close-up view of a typical Ni micropost is presented in Fig. 6.8(b), where it is evident that the micropost has not undergone any shape change. This is consistent with our molding and demolding stress measurements, which showed that stresses involved in Pb micromolding remained well below the Ni insert yield stress within the entire temperature range studied.

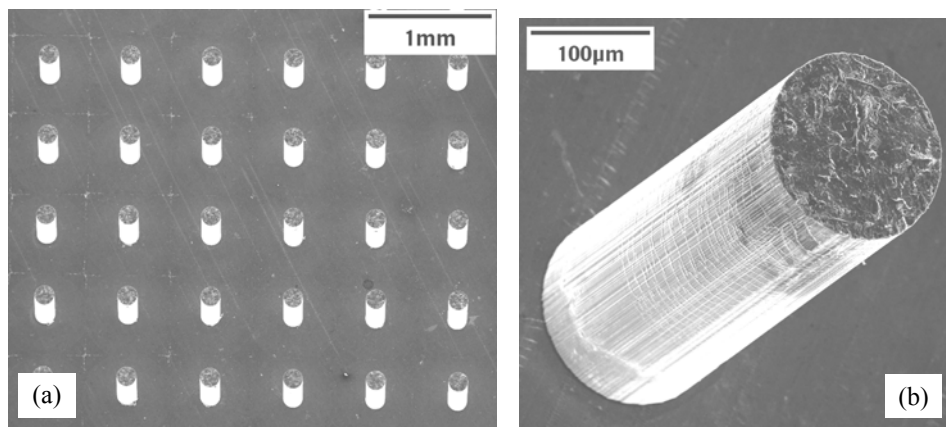


**Fig. 6.8 Condition of the LiGA Ni microscale mold insert after repeated Pb molding runs: (a) a low-magnification SEM micrograph of a field of Ni microposts; (b) a close-up view of one Ni micropost**

Although the presently measured demolding frictional stresses, arising from sliding of the Ni micropost against the Pb microhole sidewall during insert extraction, are relatively low in magnitude ( $\sim 0.5\text{MPa}$ ), their influence on molding behavior is expected to increase as the lateral dimension to depth ratio of the microscale features increases. Further experimentation along this line is clearly needed. Although a soft metal such as Pb may not be a suitable structural material, specialized applications for Pb with compression molded microscale features may exist. The high X-ray absorption coefficient of Pb and its low melting temperature make molded Pb structures potential X-

ray masks or lost molds for replicating other metallic/ceramic HARMs. Applications in these arenas remain to be explored.

## Summary

Microscale compression molding of Pb plates with LiGA fabricated Ni microscale inserts was carried out in a custom-built, high-vacuum, high-temperature, molding apparatus in the temperature range of 100 – 300°C. In-situ measurements of compressive molding force, demolding friction force, and insert displacement allowed total work of molding, maximum compressive normal stress required for molding, and maximum demolding friction stress to be measured as a function of molding temperature. Our results demonstrate that normal contact stresses required for Pb micromolding are well below the yield stress of electrodeposited Ni insert. The capability of measuring demolding friction stresses allows quantitative comparison of the efficacy of various insert surface engineering in the future. Sharp microscale features were generated on Pb plates by molding, and no apparent degradation of the Ni insert was observed after repeated molding runs. Our results show that present LiGA Ni inserts are adequate for repeated micromolding of low melting temperature metals, provided no significant metal/insert chemical interactions exist.

## References

- 1 E. W. Becker, W. Ehrfeld, P. Hagmann, A. Manner, and D. Munchmeyer, Fabrication of Microstructures with Extreme Structural Heights by Synchrotron Radiation Lithography, Galvanoforming and Plastic Moulding (LiGA Process), *Microelectron. Eng.*, 4, (1986) pp.35-56
- 2 D. M. Cao, D. Guidry, W. J. Meng, K. W. Kelly, Molding of Pb and Zn with microscale mold inserts, *Microsystem Technol.*, 9(8), (2003) pp.559-566
- 3 T. B. Massalski (ed.), *Binary Alloy Phase Diagrams*, American Society of Metals, Metals Park, Ohio (1986)
- 4 H. S. Cho, W. G. Babcock, H. Last, K. J. Hemker, *Mat. Res. Soc. Symp. Proc.* 657, EE5.23. (2001) pp. 1-6
- 5 H. S. Cho, K. J. Hemker, K. Lian, J. Goettert, G. Dirras, Measured mechanical properties of LIGA Ni structures, *Sensors and Actuators A*, 103 (1-2), (2003) pp. 59-63
- 6 D. M. Cao, T. Wang, B. Feng, W. J. Meng, K. W. Kelly, Amorphous hydrocarbon based thin films for high-aspect-ratio MEMS application, *Thin Solid Films* 398/399, (2001) pp. 553-559

## CHPATER 7. MICROSCALE COMPRESSION MOLDING OF Al WITH SURFACE ENGINEERED LiGA INSERTS \*

### Introduction

The LiGA (Lithographie, Galvanoformung, Abformung) technique occupies an important place in the arsenal of micromanufacturing technologies. In the LiGA process, high energy X-ray radiation, usually from an electron synchrotron source, is used to perform deep lithography on either polymethyl methacrylate (PMMA) or epoxy-based SU-8 resists. Developing exposed resists followed by electrodeposition yields primary high aspect ratio microscale structures (HARMS). In contrast to silicon-based microfabrication techniques, the LiGA process yields microscale structures up to a few thousand  $\mu\text{m}$  in height and widths ranging from a few tens to a few hundreds of  $\mu\text{m}$ , consisting of metals and alloys rather than silicon-based materials <sup>1</sup>.

Currently, the main impediment to commercial deployment of LiGA micromanufacturing is cost. The cost for synchrotron radiation is high, and the speed of electrodeposition is low. These two factors conspire to make primary metallic HARMS prohibitively expensive as commercial devices. To reduce production cost and increase manufacturing speed, primary metallic HARMS can be used as mold inserts to replicate secondary HARMS by compression molding. Molding in the ideal case can replicate numerous microparts from one insert and greatly reduce the cost per part. Furthermore, the electrodeposition process is often controlled by complex electrochemistry, limiting the range of materials which can be readily deposited to a few transition metals and dilute alloys <sup>2</sup>. If other metals and alloys can be compression molded with primary inserts, the range of materials which can be incorporated into HARMS based microdevices will be greatly increased. Thus economic fabrication of HARMS out of useful materials hinges on the ability to micromold. At the present time, microscale compression molding <sup>3</sup> and injection molding <sup>4</sup>, using primary HARMS as inserts, have been utilized for replication of polymer-based HARMS. Recently, we have demonstrated micromolding of low melting temperature metals such as Pb and Zn with LiGA fabricated primary Ni HARMS inserts <sup>5</sup>. Replication of Al-based HARMS by molding has not been achieved to date.

Industrial motivation for economical mass production of Al-based HARMS is high. Al-based HARMS are prime candidates for high efficiency micro heat exchangers <sup>6</sup>. Current micro heat exchanger prototypes were built out of non-optimal materials, such as polymers and electrodeposited Ni, using procedures that are not amenable to mass production <sup>7</sup>. In addition, Al-based HARMS with high surface quality may also find applications as micro optical elements <sup>8</sup>.

The process of microscale compression molding of metals, which in general occurs at higher temperatures as compared to molding polymers, requires the consideration of two issues. At the molding temperature, the yield strength of the material making up the insert bulk has to be sufficiently high to endure the stresses needed for molding. In addition, the chemical/mechanical properties of the near-surface regions of the insert have to be adequate to allow repeated molding cycles without damage to the insert and the molded metal part.

---

\* Reprinted from Microsystem Technologies with the permission of Springer-Verlag

Mechanical properties of the insert bulk need to be considered, because as-electrodeposited metallic HARMS are micro-/nano- crystalline in structure and undergo significant grain growth at elevated temperatures. Yield strength of electrodeposited Ni microparts decreased significantly to ~140MPa, less than 40% of the as-deposited value, when they are annealed to 400°C or higher <sup>9</sup>. With decreasing yield strengths at increasing temperatures, the choice of molding temperature needs to reflect a compromise between the requirement of sufficiently high yield strength of the insert, which ensures no plastic deformation of the insert bulk, and the requirement of sufficiently low yield strength of the molded metal, which facilitates generation of microscale features by plastic flow without the need for excessive force. Currently, little quantitative data regarding forces required for microscale compression molding of metals exist in the literature.

A qualitative difference in molding behavior exists depending on whether or not the insert and the molded metal have a thermodynamic driving force to mix. At present, electrodeposited Ni is the most common material choice for the insert bulk <sup>10</sup>. Regarding the chemical/mechanical interactions between the Ni insert and the molded metal, Pb and Al exemplify two extreme situations. In one instance, Pb and Ni are immiscible in both the solid and the liquid state <sup>11</sup>. In the other instance, Al and Ni have a strong driving force to form intermetallic compounds. We have previously shown that surface modification of as-fabricated Ni inserts is not necessary for Pb micromolding <sup>12</sup>. In contrast, the significant chemical interactions between Al and Ni constitute a major barrier to Al micromolding with LiGA fabricated Ni inserts.

During molding of a given metal, the chemical/mechanical interactions experienced by the insert depend critically on the chemical/mechanical/tribological properties of its near-surface region. If the mechanical properties of the insert bulk are sufficient, the key to successful high temperature micromolding of reactive metals is to alter the chemical/mechanical interactions between the insert and the molded metal. We have explored the use of ceramic coatings to modify the insert near-surface chemical/mechanical properties. With an inductively coupled plasma (ICP) assisted hybrid chemical/physical vapor deposition (CVD/PVD) technique, conformal deposition of Ti-containing hydrocarbon (Ti-C:H) coatings over LiGA fabricated Ni HARMS was demonstrated <sup>13</sup>. Morphology and composition of conformally deposited Ti-C:H coatings over Ni HARMS were characterized by scanning electron microscopy (SEM) and scanning Auger electron spectroscopy (SAES) <sup>14</sup>. Ti-C:H coatings consist of TiC nanocrystals embedded within an amorphous hydrocarbon (a-C:H) matrix <sup>15</sup>, and exhibit mechanical/tribological properties which depend systematically on the coating composition <sup>16 17</sup>. Although an aluminum carbide phase, Al<sub>3</sub>C<sub>4</sub>, exists, aluminum carbide formation induced by solid state reaction between Al and C is expected to be very sluggish <sup>18</sup>. Ti-C:H coatings are therefore promising candidates for altering the chemical/mechanical interactions between the Ni insert and Al.

In this chapter, we report high temperature instrumented micromolding of Al with as-fabricated and Ti-C:H coated Ni inserts. The molding force, demolding force, and insert displacement during molding were continuously monitored. Our results show that as-fabricated Ni inserts are not adequate for Al micromolding. We report here, to our knowledge for the first time, successful repeated high-temperature micromolding of Al, utilizing Ni inserts conformally coated with a Ti-C:H coating.

## Experimental

Primary Ni HARMs inserts were fabricated with the LiGA technique using the synchrotron facility at the Louisiana State University Center for Advanced Microstructures and Devices (LSU CAMD). Two inserts were used for evaluating the efficacies of using Ti-C:H coated and uncoated Ni inserts for Al micromolding. These two inserts were identical in nominal dimension, each consisting of a square array of cylindrical microposts,  $\sim 400\mu\text{m}$  in height,  $\sim 200\mu\text{m}$  in diameter,  $\sim 700\mu\text{m}$  in post center-to-center spacing. Each insert had a total lateral footprint of  $\sim 1.8\text{cm} \times 1.8\text{cm}$ , and contained a total of 525 microposts. One Ni insert was used in the as-fabricated condition, and the other was conformally coated with a Ti-C:H coating. Further details about insert fabrication were described elsewhere [refs. 5, 13, 14].

Deposition of Ti-C:H coatings was carried out in an ICP assisted hybrid CVD/PVD tool<sup>19</sup>. As-fabricated Ni HARMs were cleaned in acetone and methanol, loaded into the deposition chamber, and etched in a pure Ar ICP followed immediately by the deposition of a pure Ti adhesion layer and a Ti-C:H top layer. Ti-C:H deposition was carried out in the hybrid CVD/PVD mode, in which two Ti cathodes were sputtered in an Ar(99.999+%/C<sub>2</sub>H<sub>2</sub>(99.99+%) ICP at a total pressure of  $\sim 1.7\text{mTorr}$ . The ratio of Ar and C<sub>2</sub>H<sub>2</sub> input flow rates, the total ICP input power, and the Ti cathode current were fixed at 5/3, 1000W, and 1.0A, respectively. Further details on conformal Ti-C:H deposition over HARMs structures were described previously [refs. 13, 14]. No intentional substrate heating or cooling was applied, and the substrate temperature was estimated to be  $\sim 250^\circ\text{C}$  during deposition through separate thermocouple measurements.

Circular Al (1100H14, 99%Al) disks were molded. The disks were 1.4 inch in diameter and 0.25 inch in thickness, with their top surface mechanically polished with SiC abrasive papers down to 1200 grit size prior to being molded. Instrumented micromolding was carried out using a MTS858 single-axis testing system interfaced to a custom-built high-vacuum chamber. Pumped by a turbomolecular pump system, the base pressure of the molding chamber was  $\sim 1 \times 10^{-8}$  Torr. Two heating stations were installed within the vacuum chamber. Al plates to be molded were fixed on the lower heating station, mechanically attached to the bottom of the vacuum chamber. The insert was mechanically attached to the upper heating station, which was connected to the linear actuator through a bellows-sealed Z-motion feedthrough. The two heating stations were heated separately by resistive heating cartridges. Insert and metal temperatures were measured by two separate K-type thermocouples, with the temperature – time histories recorded on a computer. The entire molding/demolding process commenced after temperatures of the Al plate and the insert reached steady state. The inserts were heated to  $462 \pm 5^\circ\text{C}$  prior to molding. The Al plate temperatures prior to molding are given in Table 1. All Al micromolding experiments were performed at pressures  $\leq 3 \times 10^{-4}$  Torr at the final molding temperature. Insert attached to the linear actuator could be programmed to move according to prescribed load forces in the force-controlled mode or actuator displacements in the displacement-controlled mode. The axial force was measured by a 5kN load cell with a resolution of  $\sim 5\text{mN}$ , and the axial displacement was measured by a linear variable displacement transducer with a resolution of  $\sim 0.5\mu\text{m}$ . Further details on the instrumented micromolding apparatus and the molding procedure were described elsewhere [ref. 12].

SEM examinations of as deposited Ti-C:H coatings, inserts before and after Al molding runs, and molded Al plates were carried out on a JEOL 840A microscope. X-ray photoelectron spectroscopy (XPS) and scanning Auger electron spectroscopy (SAES) examinations were carried out on a Kratos AXIS165 Auger/XPS system. Optical profilometry (OP) measurements were carried out on a Wyko NT1000 interference microscope. XPS and AES data were collected using respectively monochromatic Al K $\alpha$  and 5kV/45 $\mu$ A electron excitation. AES data were recorded in the N(E) mode and derivatized using a 23-point quadratic Savitzky-Golay filter. Surface profiles were obtained through OP in the vertical scanning interferometry (VSI) mode. XPS measurements on Ti-C:H coatings deposited with the same recipe on Si wafer substrates showed that oxygen impurity level is below 1 at.%, and the Ti to C ratio was less than 0.05.

## Results and Discussion

A number of Al disks were compression molded with the Ti-C:H coated Ni insert at  $\sim 450^\circ\text{C}$ . Figures 7.1(a) and 1(b) show respectively the axial displacement of and the total force on the insert as a function of time during one entire Al micromolding run at  $458^\circ\text{C}$ . At the beginning of the initial approach (A) segment, the insert did not make contact with the Al plate. In the approach segment, the insert was moved toward the Al plate at a constant displacement rate. The slight increase in compression force due to insert movement, about -3N/mm, reflected the compression of the Z-motion feedthrough bellow. Insert/Al contact was detected when the compression force showed an abrupt

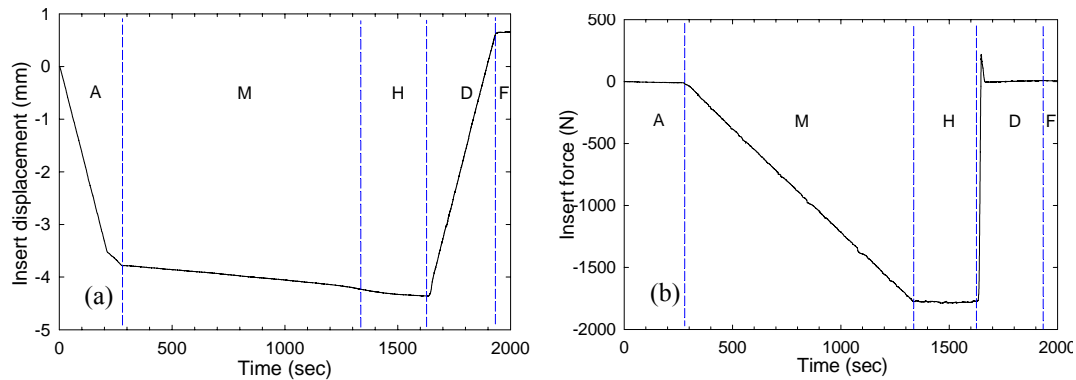


**Fig. 7.1 Data from an instrumented Al micromolding run at  $458^\circ\text{C}$  with a Ti-C:H coated Ni insert: (a) insert displacement vs. time; (b) total force on the insert vs. time. The initial approach (A), molding (M), constant-force hold (H), demolding (D), and final hold (F) segments of the micromolding process are delineated by dotted lines**

increase, at which time a constant loading-rate, -100N/min, molding (M) segment was initiated. During the molding segment, the insert displacement was observed to be roughly linear with time. The molding segment was terminated when the cumulated insert displacement within this segment reached  $400\mu\text{m}$ , at which point a 5 min duration constant force hold (H) segment was initiated. After the hold segment, the insert was withdrawn from the Al plate at a constant displacement rate of  $1000\mu\text{m}/\text{min}$  in the

demolding (D) segment. The initial demolding led to a rapid change in the total force on the insert, from a compressive to a tensile one. This tensile force reached a maximum, and then decreased to a slowly varying background level in ~21sec. This background force variation, about +3N/mm, reflected the stretching of the Z-motion feedthrough bellow after complete insert/Al plate separation. The insert was held at the final position for 2min during the final hold (F) segment, during which force on the insert remained a constant.

The molding segment is examined in Figure 7.2(a), in which the molding force on the insert is displayed against molding depth for four consecutive Al micromolding runs with the same Ti-C:H coated Ni insert. Data shown in Figure 7.2(a) indicate very similar molding behavior during four consecutive Al micromolding runs with the same Ti-C:H coated Ni insert, from which the maximum molding force, occurring at the end of the molding segment, and the total work of molding were obtained and shown in Table 7.1.

**Table 7.1. Measured parameters of Al micromolding runs with one Ti-C:H coated Ni insert (CI) and one uncoated Ni insert (UCI)**

Insert / molding cycle	Al plate temperature (°C)	Maximum molding force (N)	Total work of molding (N*mm)	Maximum demolding force (N)
CI/1 <sup>st</sup>	433	1627	341	189
CI/2 <sup>nd</sup>	459	1732	345	204
CI/3 <sup>rd</sup>	457	1677	368	223
CI/4 <sup>th</sup>	458	1644	346	225
UCI/1 <sup>st</sup>	460	1790	389	582

The demolding behavior for these four Al micromolding runs is examined in more detail in Figure 7.2(b), in which total forces on the insert are displayed against time during the relevant portions of the demolding segments. The total axial force on the insert reached a maximum in tension, about +200N, and subsequently decreased to a slowly

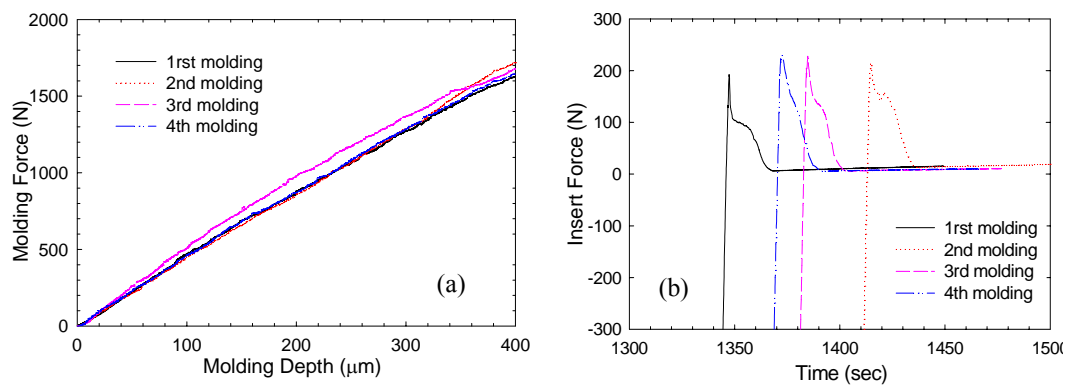


**Fig. 7.2 Molding and demolding behavior during Al micromolding with the Ti-C:H coated Ni insert at ~450°C: (a) molding force – insert displacement relationship for four consecutive molding runs; (b) demolding force versus time for four consecutive molding runs**

varying background in ~21sec. The difference between the maximum tensile force and the extrapolated background measures the maximum demolding force experienced during demolding, the values of which are also shown in Table 7.1. The duration of the tensile force decrease corresponds to an insert withdrawal distance of ~350 $\mu$ m. Considering the height of the microposts on the insert was 400 $\mu$ m, the maximum demolding force was reached close to the point where the microposts had full side contact with Al. Data shown in Table 7.1 indicate that, as the same Ti-C:H coated Ni insert was used to mold Al repeatedly, there was no significant increase in either the maximum molding force or the maximum demolding force. The demolding behavior, as judged from data shown in Figure 7.2(b), remained largely unchanged.

The difference in Al molding/demolding behavior with Ti-C:H coated and uncoated Ni inserts is illustrated in Figure 3. The total force on the insert versus time during the entire molding/demolding cycle is shown in Figure 7.3(a). The initial approach segments are not shown. Force-time histories for the first and the fourth runs of the four consecutive molding runs with the Ti-C:H coated Ni insert are shown, together with the corresponding information recorded during the first molding run with an uncoated Ni insert. In all cases, the insert loading rate was held constant at 100N/min in the molding segment, resulting in an insert displacement rate of about 24 $\mu$ m/min. When the uncoated Ni insert was used to mold Al, a small increase in the maximum molding force was observed, as evidenced in Figure 7.3(a) and shown in Table 7.1. The more striking contrast was observed in the demolding behavior, as illustrated in more detail in Figure 7.3(b). Rather than reaching a tensile force maximum in the beginning of insert withdrawal followed by a continuous decrease in the tensile force to the background level, the extraction of the uncoated Ni insert from the Al plate led to an increasing tensile force over a 90sec period. This tensile demolding force, over 2.5 times higher than the maximum demolding forces experienced with the coated Ni insert, led to a partial breakage of the insert attachment on the upper heating station, resulting in an abrupt force decrease. Even after the attachment breakage, a part of the insert remained attached to the Al plate, as reflected by the remnant tensile force above the background level. The Ni

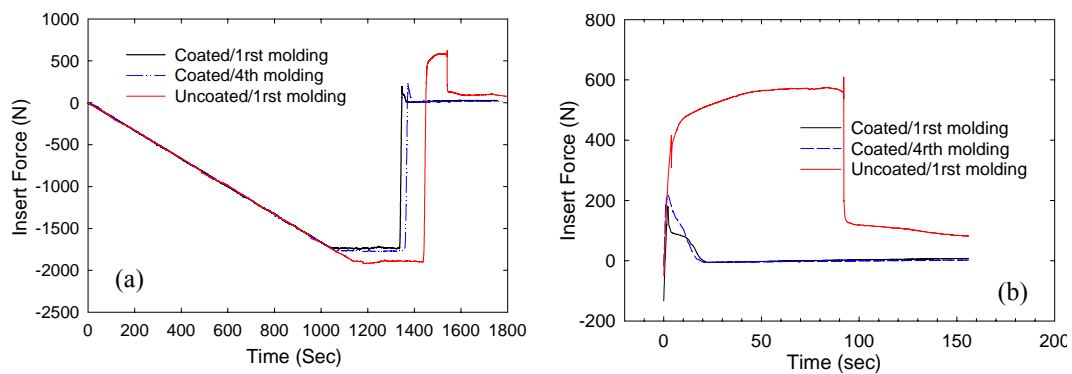


**Fig. 7.3** Micromolding of Al with Ti-C:H coated and uncoated Ni inserts: (a) total force on the insert versus time during three entire Al molding/demolding cycles with Ti-C:H coated and uncoated Ni inserts; (b) corresponding demolding force vs. time. Time origins in (b) were shifted to make the demolding curves coincide in the beginning of the demolding process



insert, after manual detachment, was significantly bent and unsuitable for additional molding runs. One side of the insert had extensive Al pickup, which embedded one entire row of Ni microposts. As expected, chemical interactions between the uncoated Ni insert and the Al plate led to bonding and difficulty in insert extraction from the Al plate after molding.

Figure 7.4(a) shows an optical micrograph of the Al plate molded in the fourth molding run with the Ti-C:H coated Ni insert. The imprints of four support pads and rims, located respectively at the four corners and outer perimeters of the square shaped insert, are also visible on the Al plate. Support pads and rims are at the same height as the cylindrical microposts. Each support pad contained a threaded hole in the middle through which the insert was attached to the upper heating station. No contact of the securing screws and the Al plate took place during molding. Figure 7.4(a) shows that the molded Al plate contained in entirety the negative of the features present on the insert. The low magnification SEM image shown in Figure 7.4(b) indicates that the square array of

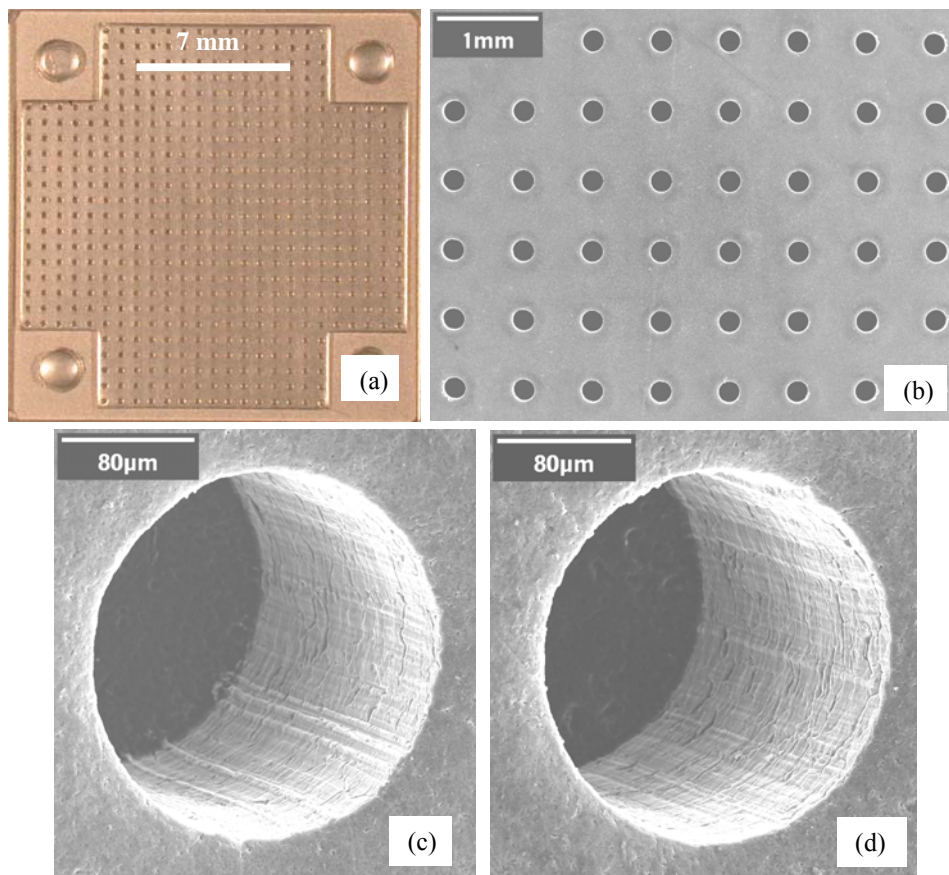


**Fig. 7.4 Condition of a Al plate after micromolding by the Ti-C:H coated Ni insert at 458°C: (a) an optical micrograph showing the entire molded Al plate; (b) a SEM image showing an array of microholes generated. The microhole diameter is 200μm and the hole center-to-center spacing is 700μm; (c) and (d) are high magnification views from opposite sides of a typical microhole**

cylindrical microposts on the insert was faithfully replicated into a square array of cylindrical microholes on the Al plate. Higher magnification views from opposite sides of a typical microhole, shown respectively in Figures 4(c) and 4(d), show that molded Al microholes have sharp top rim, smooth sidewalls, and abrupt sidewall to bottom transitions. All 525 microholes were intact, and no damage to the microhole feature was observed. OP measurements showed microholes with depths about 400 $\mu\text{m}$ , demonstrating the achievement of 100% molding. Examination of other molded Al plates showed microholes with similar quality of feature replication.

The overall condition of the Ti-C:H coated Ni insert after the fourth molding run is illustrated in Figure 7.5(a). The high magnification view of one typical Ti-C:H coated Ni micropost, shown in Figure 7.5(b), indicates little deformation of and no Al transfer on Ti-C:H coated Ni microposts after four consecutive molding runs. No coating delamination from the Ni microposts is evident. To our knowledge, data shown in Figures 7.4 and 7.5 represent the first successful demonstration of replication of Al HARMs by high temperature compression molding with LiGA fabricated inserts.

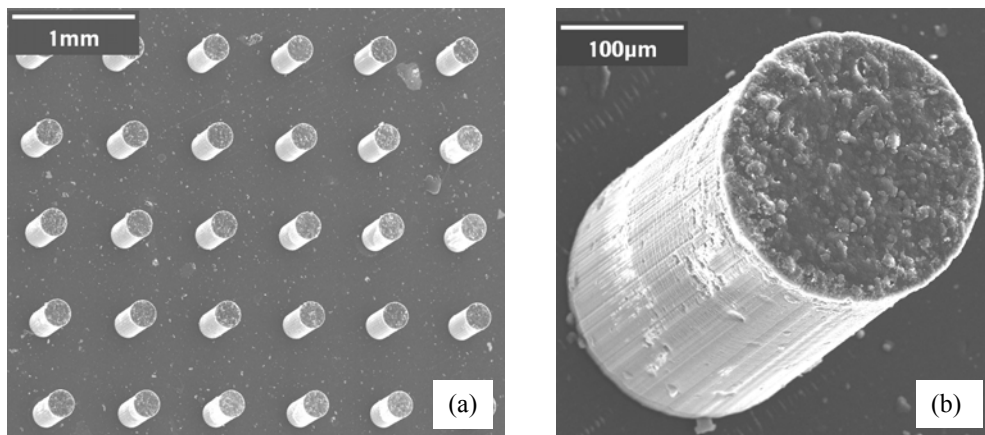


**Fig. 7.5 Condition of the Ti-C:H coated Ni insert after four consecutive Al molding runs at  $\sim 450^\circ\text{C}$ : (a) insert overview; (b) high magnification view of a typical Ti-C:H coated Ni micropost on the insert**

Figure 7.6 shows conditions of the Al plate molded with the uncoated Ni insert and the uncoated insert after one molding run. Although a microhole array was generated on the Al plate, the low magnification view of the Al plate shown in Figure 7.6(a) shows that some Al was torn away from one side of each microhole. Some Al pickup occurred on each Ni micropost. The damage to the uncoated Ni insert is exemplified by the high magnification view of one typical Ni micropost in Figure 7.6(b), showing clear evidence of Al transfer after one molding run, which was confirmed by SAES. The asymmetric damage observed both on the Al plate and the Ni microposts is believed to be related to a small misalignment between the insert and the Al plate, resulting in preferential insert/Al contact on one side of the micropost. Since the same misalignment existed between the coated insert and the Al plate, data shown in Figures 7.4, 7.5, and 7.6 suggest that the reduced chemical/mechanical interaction between the insert and Al afforded by the conformal Ti-C:H coating led to more misalignment tolerance. Figure 7.6(c) illustrates

one form of severe insert damage. The high magnification view of the Al plate molded by the uncoated Ni insert shows that the particular Ni micropost was broken from the insert and trapped within the Al microhole. This is confirmed by the SAES spectra shown in Figure 7.6(d), taken in the spot mode respectively from areas outside and within the microhole. Outside the microhole [spot A], only Al signal is present in addition to C and O contamination. Inside the microhole [spot B], additional Ni signal is clearly present, confirming the material within the microhole is the trapped Ni micropost from the insert. While over ten such micropost breakages were observed on the uncoated Ni insert, none was observed on the coated insert. The broken microposts may reflect existing weaknesses due to the electrodeposition process.

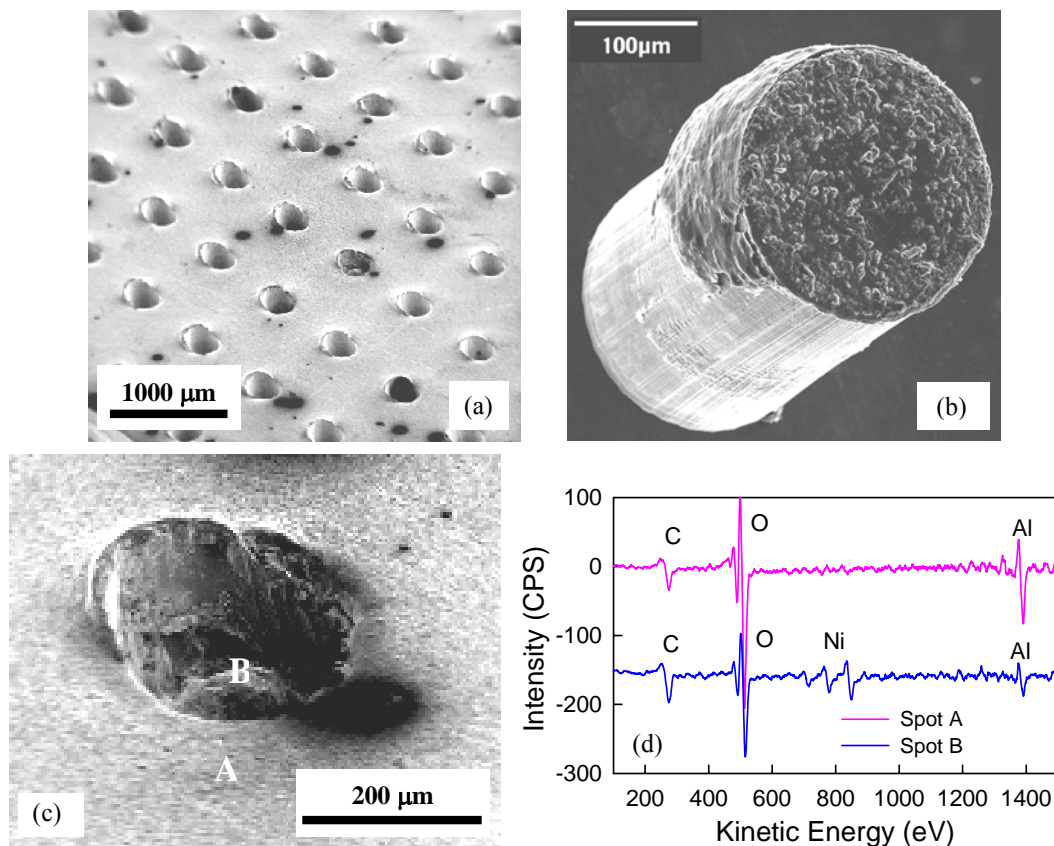


**Fig. 7.6** Conditions of the uncoated Ni insert after one molding run and of the corresponding molded Al plate: (a) overview of the molded Al plate; (b) high magnification view of a typical Ni micropost on the insert; (c) high magnification view of a Ni micropost trapped within one Al microhole; (d) AES spectra obtained from outside (A) and within (B) the microhole

The measured maximum force needed to mold Al can be converted to a maximum normal compressive stress on the Ni insert. The calculated maximum compressive stress, taking into account the entire nominal area of contact, is  $\sim 18\text{MPa}$  at molding temperatures  $\sim 450^\circ\text{C}$ . Our present observations showed no perceptible shape change in the microposts after molding, and suggest that electrodeposited Ni inserts possess

adequate bulk strength for Al micromolding at  $\sim 450^{\circ}\text{C}$ . These observations are consistent with strength measurements on electrodeposited Ni microscale specimens [ref. 9]. Observations presented in Figures 7.4 and 7.5 suggest that no significant bonding occurred between Al and the Ti-C:H coated Ni insert. Thus it is justifiable to convert the measured maximum demolding force for the coated insert into a demolding frictional stress. Assuming full micropost sidewall contact when the maximum demolding force was generated, the average frictional stress based on the data shown in Table 7.1 is  $\sim 1.1\text{MPa}$ . The same demolding force to frictional stress conversion cannot be made in the case of the uncoated Ni insert, since in this case adhesive forces likely make the dominant contribution to the demolding force, as evidenced in Figure 7.6.

Further experimentation on Al micromolding also demonstrated the need for carbon based coatings with improved high temperature stability. Current Ti-C:H coatings were deposited at  $\sim 250^{\circ}\text{C}$ , and may suffer hydrogen desorption at the higher molding temperatures of  $\sim 450^{\circ}\text{C}$ , which may in turn induce further coating degradation. Figure 7.7(a) shows a high magnification view of a typical micropost on the Ti-C:H coated Ni insert after the first Al molding run at  $\sim 450^{\circ}\text{C}$ , showing no Al transfer on the micropost and little change in coating appearance. Figure 7.7(b) shows a high magnification view of another typical micropost on the same Ti-C:H coated Ni insert after the fourth Al molding run. Although little Al pickup on the micropost can be seen, there is clearly a change in a fraction of the Ti-C:H coating on the micropost, resulting in increased image brightness over some regions on the micropost. We speculate that this change may be due to hydrogen loss from the coating and subsequent coating graphitization, which changes the secondary electron yield of the region and therefore the brightness in the SEM image. Additional Al micromolding experiments were conducted at  $\sim 500^{\circ}\text{C}$  with another primary Ni insert conformally coated with a Ti-C:H coating of nominally the same

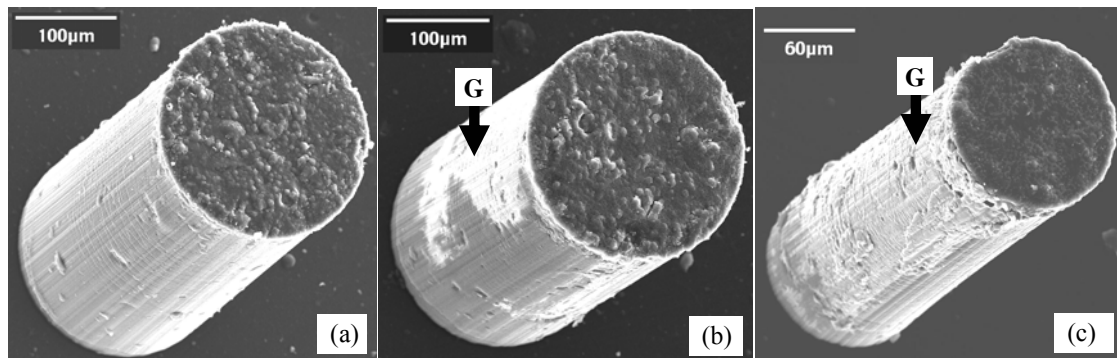


**Fig. 7.7 Behavior of Ti-C:H coatings deposited on Ni inserts at  $\sim 250^{\circ}\text{C}$  during high temperature Al micromolding: (a) a typical Ti-C:H coated Ni micropost after one Al molding run at  $\sim 450^{\circ}\text{C}$ ; (b) appearance of the same Ti-C:H coating on another typical Ni micropost after four Al molding runs at  $\sim 450^{\circ}\text{C}$ ; (c) appearance of another Ti-C:H coating on another Ni insert after one Al molding run at  $\sim 500^{\circ}\text{C}$ . The compositions of all the Ti-C:H coatings were nominally identical. Change in secondary electron image brightness and coating appearance, speculatively attributed to graphitization, can be seen in areas marked “G”**

composition deposited under nominally identical conditions. With the increase in molding temperature from  $\sim 450^{\circ}\text{C}$  to  $\sim 500^{\circ}\text{C}$ , Figure 7.7(c) shows that the change in the Ti-C:H coating evidenced in Figure 7.7(b) appears to accelerate. This is consistent with the expectation of accelerated hydrogen loss and graphitization of Ti-C:H at higher temperatures. Hydrogen loss from and graphitization of Ti-C:H coatings implies lessened coating durability and consequently shortened insert life. Extended life testing for coated inserts has not been conducted.

In general, the choice of coating material is expected to influence the friction between the coated insert and Al during molding and the demolding force during insert withdrawal due to variation in the chemical/mechanical interactions. Detailed study on the high temperature tribochemistry between various coating materials and Al has not been conducted to date, and clearly deserves further investigation. Friction between the coated insert and the molded metal may influence sidewall roughness of molded features, which may impact the ability to use replicated Al HARMs for micro optical applications. The design of the insert/adhesion-layer/coating-layer system will affect coating delamination and therefore long-term insert life. Strategies for accelerated insert life evaluation need to be devised. The mechanical properties of the insert bulk may need further improvement, especially for higher temperature applications.

## Summary

In summary, microscale compression molding of Al plates with as-fabricated Ni inserts and Ni inserts conformally coated with a Ti-C:H coating was carried out. In-situ measurements of the molding force, demolding force, and insert displacement allowed molding behavior with as-fabricated Ni inserts to be compared quantitatively with that using Ti-C:H coated Ni inserts. Our results showed that as-fabricated Ni inserts are not suitable for Al micromolding, and that conformal Ti-C:H deposition over Ni HARMs inserts enables repeated Al micromolding with 100% feature replication.

## References

- 1 M. Madou, Fundamentals of Microfabrication, CRC Press, Boca Raton (2000)
- 2 J. A. MacGeough, M. C. Leu, K. P. Rajurkar, A. K. M. De Silva, Q. Liu, Electroforming process and application to micro/macro manufacturing, CIRP Annals-Manuf. Technol. 50(2), (2001) pp. 499-514
- 3 M. Hecke, W. Bacher, and K. D. Müller, Hot Embossing - The Molding Technique for Plastic Microstructures, Microsystem Technol., 4(3), (1998) pp.122-124
- 4 V. Piottter, K. Mueller, K. Plewa, R. Ruprecht, and J. Hausselt, Performance and Simulation of Thermoplastic Micro Injection Molding, Microsystem Technol., 8, (2002) pp. 387-390
- 5 D. M. Cao, D. Guidry, W. J. Meng, and K. W. Kelly, Molding of Pb and Zn with microscale mold inserts, Microsystem Technol. 9 (8), (2003) pp. 559-566

- 6 C. Harris, M. Despa, K. W. Kelly, Design and Fabrication of a Cross Flow Micro Heat Exchanger, IEEE J. MEMS. 9, (2000) pp.502-508
- 7 C. Harris, K. Kelly, T. Wang, A. McCandless, and S. Motakef, Fabrication, Modeling, and Testing of Micro-Cross-Flow Heat Exchangers, IEEE J. MEMS 11(6), (2002) pp. 726-735
- 8 K. Evans-Lutterodt, J. M. Ablett, A. Stein, C. C. Kao, D. M. Tennant, F. Klemens, A. Taylor, C. Jacobsen, P. L. Gammel, H. Huggins, S. Ustin, G. Bogart, L. Ocola, Single-element elliptical hard x-ray micro-optics, Optics Express 11 (8), (2003) pp. 919-926
- 9 H. S. Cho, K. J. Hemker, K. Lian, J. Goettert, G. Dirras, Measured mechanical properties of LIGA Ni structures, Sensors and Actuators A, 103 (1-2), (2003) pp. 59-63
- 10 W. Bacher, K. Bade, B. Matthis, M. Saumer, R. Schwarz, Fabrication of LIGA mold inserts, Microsystem Technol., 4(3), (1998)pp. 117-119
- 11 T. B. Massalski (ed.), Binary Alloy Phase Diagrams, American Society of Metals, Metals Park, Ohio, (1986)
- 12 D. M. Cao, W. J. Meng, and K. W. Kelly, High-temperature instrumented microscale compression molding of Pb, Microsystem Technol. 10, (2004) pp. 323-328
- 13 D. M. Cao, T. Wang, B. Feng, W. J. Meng, and K. W. Kelly, Amorphous hydrocarbon based thin films for high-aspect-ratio MEMS applications, Thin Solid Films 398/399, (2001) pp. 553-559
- 14 D. M. Cao, W. J. Meng, S. J. Simko, G. L. Doll, T. Wang, and K. W. Kelly, Conformal deposition of Ti-C:H coatings over high-aspect-ratio microscale structures and tribological characteristics, Thin Solid Films 429, (2003) pp. 46-54
- 15 W. J. Meng, R. C. Tittsworth, J. C. Jiang, B. Feng, D. M. Cao, K. Winkler, V. Palshin, Ti atomic bonding environment in Ti-containing hydrocarbon coatings, J. Appl. Phys., 88 (5), (2000) pp.2415-2422
- 16 D. M. Cao, B. Feng, W. J. Meng, L. E. Rehn, P. M. Baldo, M. M. Khonsari, Friction and Wear Characteristics of Ceramic Nanocomposite Coatings: Titanium Carbide/Amorphous Hydrocarbon, Appl. Phys. Lett. 79 (3), (2001) pp. 329-331
- 17 B. Shi, W. J. Meng, Intrinsic stresses and mechanical properties of Ti-containing hydrocarbon coatings, J. Appl. Phys. 94 (1), (2003) pp. 186-194

- 18 C. A. Handwerker, M. D. Vaudin, U. R. Kattner, D. J. Lee, in *Metal-Ceramic Interfaces*, edited by M. Ruhle, A. G. Evans, M. F. Ashby, J. P. Hirth, Pergamon Press, Oxford, (1990)
- 19 W. J. Meng, T. J. Curtis, L. E. Rehn, P. M. Baldo, Temperature dependence of inductively coupled plasma assisted growth of TiN thin films, *Surf. Coat. Technol.* 121, (1999) pp. 206-212

## **CHAPTER 8. STRESS DURING MICROMOLDING OF METALS AT ELEVATED TEMPERATURES: PILOT EXPERIMENTS AND A SIMPLE MODEL**

### **Introduction**

Metal-based microdevices and micro-electro-mechanical systems (MEMS) have important advantages over Si-based MEMS, especially for devices designed to operate under high stresses, at high temperatures, or using the physical properties of metals and alloys. Because of these advantages, a number of metal-based microdevice prototypes have been built, and many more have been envisioned. Examples of existing, metal-based, active microdevices include magnetohydrodynamic micropumps <sup>1</sup>, electrostatic microactuators <sup>2</sup>, and electromagnetic micro relays <sup>3</sup>. Examples of existing, metal-based, passive microdevices include cross-flow micro heat-exchangers <sup>4</sup>, microscale X-ray masks <sup>5</sup>, and microscale chemical reactors <sup>6</sup>. Most of the metal-based active or passive microdevices envisioned require the construction of microscale structures with larger ratios of height to lateral dimensions as compared to what is typical for Si-based MEMS. Despite the considerable practical implications if metal-based microdevices can be manufactured economically, current techniques for making metallic, high-aspect-ratio, microscale structures (HARMS) are much less well developed as compared to the mature, Si-based, integrated-circuit, fabrication technologies.

Among the techniques for making metallic HARMS, one the most important is the LiGA (Lithographie, Galvanoformung, Abformung) technique based on deep lithography and electrodeposition. In the conventional LiGA approach, a primary pattern is generated in polymeric resist by X-ray lithography. The penetrating power of X-ray, usually from an electron synchrotron source, creates vertical structures in the resist ranging from a few hundred  $\mu\text{m}$  to a few thousand  $\mu\text{m}$  in height. Chemical dissolution of resist in areas exposed to X-ray is followed by metal electrodeposition into the developed resist recesses. Dissolution of the remaining resist after electrodeposition yields primary metallic HARMS. Further explanation of the LiGA process can be obtained elsewhere <sup>7</sup>.

Unfortunately, the electrodeposition process in LiGA is often controlled by complex electrochemistry, limiting the range of materials which can be readily deposited to Au, Cu, Ni, and dilute Ni alloys. Furthermore, the high cost of synchrotron radiation and the slow speed of metal electrodeposition conspire to make primary metallic HARMS too expensive for commercial deployment. Although replication of secondary structures by molding using electrodeposited primary metallic HARMS as mold inserts was proposed over twenty years ago <sup>8</sup>, up to 2002 only polymer-based HARMS have been replicated from primary metallic HARMS by compression molding <sup>9</sup> or injection molding <sup>10</sup>.

Alternative techniques for fabricating metallic HARMS have been explored. Micromilling ( $\mu\text{MIL}$ ) with tools fabricated with a focused ion beam technique extends the traditional metal cutting approach to the micro realm <sup>11</sup>. Micro electrical-discharge-machining ( $\mu\text{EDM}$ ) have been used to machine HARMS out of metallic alloys <sup>12</sup> and electrically conducting ceramics <sup>13</sup>. Techniques derived from the LiGA approach include micro powder injection-molding ( $\mu\text{PIM}$ ) and micro casting ( $\mu\text{CAS}$ ). In the  $\mu\text{PIM}$  approach, feedstock consisting of fine metal powders mixed with an organic binder is injected into a LiGA fabricated mold insert. After separation from the insert, the shaped



compact is subjected to multiple heat treatments to achieve close-to-full density<sup>14</sup>. In the  $\mu$ CAS approach, plastic HARMS replicated from a LiGA fabricated mold insert are embedded in a ceramic investment material, which is fired to form a hollow ceramic mold by pyrolyzing the plastic structure. Molten metal is subsequently made to fill the ceramic mold by centrifugal or vacuum pressure casting<sup>15</sup>. Serial subtractive techniques such as  $\mu$ MIL and  $\mu$ EDM are time consuming, and can suffer from serious tool wear. The  $\mu$ PIM technique requires multiple heat treatment steps, and suffers from incomplete mold filling and part shrinkage during heat treatment<sup>16</sup>. The  $\mu$ CAS technique again requires multiple heat treatment steps, and is a “double lost mold” technique in that the initial plastic HARMS as well as the ceramic mold are sacrificed to obtain the final metallic HARMS. The disadvantages associated with each of these alternative techniques motivate further investigation of micromolding as a means of replicating secondary metallic HARMS.

Recently, we have investigated the feasibility of directly replicating metallic HARMS by compression molding of metals with LiGA fabricated mold inserts. Successful replication of Pb and Zn HARMS was demonstrated with LiGA fabricated primary Ni mold inserts. It was shown that the process of high temperature micromolding of metals is strongly influenced by chemical and mechanical interactions between the molded metal and the mold insert. In the case where the molded metal and the insert are immiscible, such as Pb and Ni, no modification of the LiGA fabricated insert is necessary. In the case where the molded metal and the insert have a thermodynamic driving force to react, such as Zn and Ni, modification of the chemical and mechanical properties of the near-surface region of the insert is critical to achieving molding replication without damage to the insert or the molded features<sup>17</sup>. We have investigated the potential of engineering the chemical, mechanical, and tribological properties of the near-surface region of metallic mold inserts by conformal deposition of nanostructured ceramic coatings over LiGA fabricated HARMS<sup>18</sup>. The technique of high density plasma assisted hybrid chemical/physical vapor deposition was shown to be an effective means for conformal deposition of nanostructured ceramic coatings over HARMS with heights up to 1000 $\mu$ m<sup>19</sup>. Following this approach, we demonstrated, in 2003, successful replication of Al-based HARMS, 400 to 500 $\mu$ m in height, by compression molding at  $\sim$ 450°C with LiGA fabricated Ni mold inserts conformally coated with titanium-containing amorphous hydrocarbon<sup>20</sup>. As compared to other techniques for fabricating metal-based HARMS, this procedure for direct replication of metallic HARMS by high temperature compression micromolding is fast and simple, and therefore holds potential advantages in production cost and throughput.

Besides the need to engineer the chemical and mechanical interactions between the molded metal and the mold insert, the bulk mechanical properties of LiGA fabricated inserts restrict the range of metals and alloys which can be compression molded. Electrodeposition of Ni and other metals and alloys typically results in the formation of nanocrystalline deposits. The extensive structural evolution occurring within the electrodeposited insert bulk at high molding temperatures can lead to a significant decrease in its yield strength<sup>21</sup>. This yield strength decrease places limits on the highest allowable molding temperature and consequently the type of metals and alloys which can be compression molded. Although we have previously monitored in-situ the forces exerted on the mold insert during molding and extraction<sup>22</sup>, the issue of how the

mechanical properties of the molded metal influence the contact stresses exerted on the mold insert during molding was not addressed. Answering this question enables an intelligent choice of molding temperature for any metal to be molded, provided its mechanical properties at the intended molding temperature are known.

The metal Pb serves as a good model material in which to study the mechanics of micromolding. The first reason for choosing Pb is its immiscibility with Ni in both the solid and liquid states<sup>23</sup>. Because of this immiscibility, LiGA fabricated Ni mold inserts in the as-fabricated state can be used repeatedly to generate well-defined microscale features in Pb by compression molding without damage<sup>22</sup>. The second reason for choosing Pb is its melting temperature,  $T_m$ , of 601K. Because of this low melting temperature, Pb micromolding experiments can be easily executed in a wide range of reduced molding temperatures,  $\bar{T}$ , where  $\bar{T} = T/T_m$  and  $T$  is the temperature at which molding is undertaken. For example, Pb micromolding at  $\bar{T}$  ranging from 0.5 to 0.9 is readily achieved<sup>22</sup>.

This chapter reports on preliminary experiments and modeling pertaining to the mechanics of Pb micromolding, as carried out with LiGA-fabricated, Ni microscale inserts. In what follows, the experimental procedures and results for forces during Pb micromolding are given in Section II, along with the morphologies of the Pb after micromolding. Section III provides a basis for modeling the micromolding process by summarizing known results for indentation of an elasto-plastic half-space by a spherical indenter. Section IV draws on Section III to develop a simple model relating force on a cylindrical micropost to indentation depth. Section V reports the results of tensile testing on Pb which gives the mechanical properties at the various temperatures needed for the simple model. Section VI then compares experimental results with the simple model. Section VII closes the paper with some concluding remarks in light of these comparisons.

## Microscale Compression Molding at Elevated Temperatures

### A. Experimental Procedures

Ni microscale mold inserts were fabricated with the LiGA technique using the synchrotron facility at the Center for Advanced Microstructures and Devices (CAMD) at Louisiana State University (LSU). The mold insert consisted of an array of cylindrical Ni microposts protruding from a flat Ni base. The Ni microposts were 500 $\mu$ m in height and 200 $\mu$ m in diameter, with a 800 $\mu$ m post-to-post spacing. The insert had a lateral footprint of ~18mm $\times$ 18mm, and contained a total of 377 microposts. Further details about the insert fabrication process have been reported previously<sup>18 19 22</sup>. An as-fabricated Ni insert was cleaned in acetone and methanol prior to being used to compression mold Pb plates, which were 99% pure and in the form of circular disks, ~35mm in diameter and ~6.4mm in thickness. The Pb plate surfaces were mechanically polished with SiC abrasive papers from 400 to 1000 in grit size prior to being molded.

Instrumented micromolding was carried out on a MTS858 single-axis testing system interfaced to a high-vacuum molding chamber. Pumped by a turbomolecular pump system, the ultimate chamber base pressure was  $\sim 1 \times 10^{-8}$  Torr. All Pb micromolding experiments were performed at pressures  $\leq 2 \times 10^{-7}$  Torr. Two heating stations were installed within the vacuum chamber. The Pb plates to be molded were fixed on the lower

heating station, mechanically attached to the bottom of the molding chamber. The insert was mechanically attached to the upper heating station, which was connected to the linear actuator through a bellows-sealed Z-motion feedthrough. The two heating stations were heated separately by resistive heating cartridges. Insert and metal temperatures were measured by two separate K-type thermocouples, with the temperature – time histories recorded on a computer. In steady state, the plate temperature and the insert temperature were held to within  $\sim 5^{\circ}\text{C}$  of each other. The entire molding and demolding process only commenced after steady state temperature conditions were reached, with a typical temperature variation of  $\pm 2^{\circ}\text{C}$ . The insert attached to the linear actuator could be programmed to move according to prescribed load forces in the force-controlled mode or prescribed actuator displacements in the displacement-controlled mode. The axial force was measured by a 5kN load cell with a resolution of  $\sim 5\text{mN}$ , and the axial displacement was measured by a linear variable displacement transducer with a resolution of  $\sim 0.5\mu\text{m}$ . The entire micromolding process includes five segments: a displacement-controlled approach with a force limit; a force-controlled molding with a displacement limit; a constant force hold; a displacement-controlled demolding; and a constant displacement final hold. Further details on the instrumented micromolding apparatus and the molding procedure are described elsewhere <sup>22</sup>.

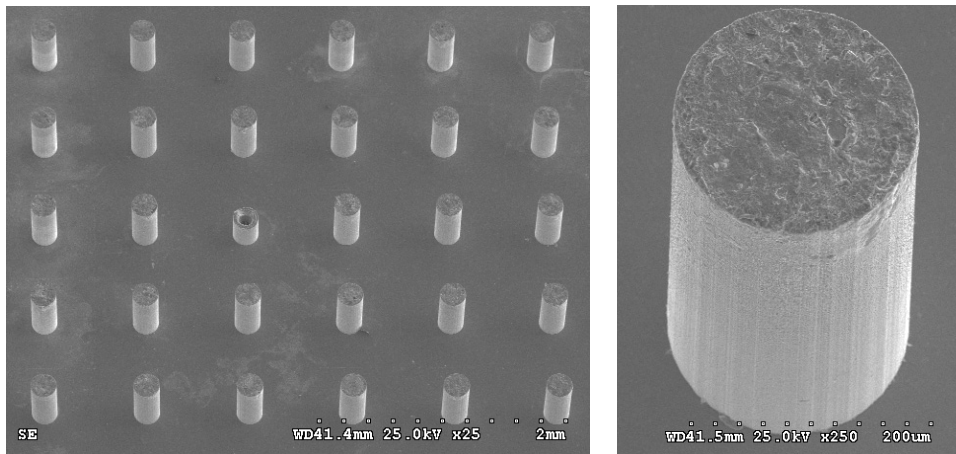
Using a single Ni insert, the same micromolding process was repeated on a series of Pb plates heated to temperatures ranging from  $\sim 30^{\circ}\text{C}$  to  $\sim 220^{\circ}\text{C}$ , corresponding to  $0.5 \leq \bar{T} \leq 0.8$ . Demolding occurred at the molding temperature. Scanning Electron Microscopy (SEM) examinations of the molded features in Pb and the Ni insert condition after molding were carried out on a Hitachi S-3600N microscope.

## B. Experimental Results

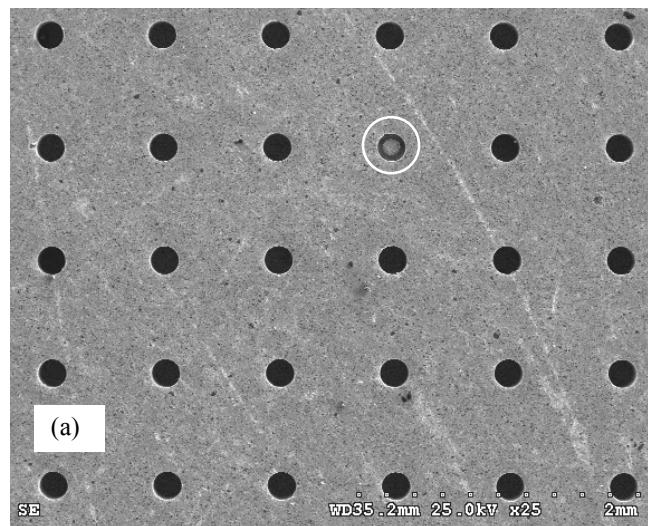
Figure 8.1(a) shows a SEM micrograph of a portion of the Ni insert after multiple Pb compression molding runs at temperatures ranging from  $\sim 30^{\circ}\text{C}$  to  $\sim 220^{\circ}\text{C}$ . The square arrangement of Ni microposts protruding from the flat Ni base is clearly visible, and the insert contained no protruding features other than these microposts. Occasional defective Ni microposts are visible on the insert, resulting from defects in either the pattern definition stage or the electrodeposition stage of the insert fabrication. During compression molding, the only contacting parts between the Ni insert and the Pb plate are the microposts. Figure 8.1(b) shows a higher magnification view of a typical Ni micropost, showing no evidence of insert damage or Pb transfer to the micropost after repeated Pb micromolding at different temperatures. These results confirm the expectation that no conformal coatings are needed when Ni microposts are used to mold Pb.

Figure 8.2(a) shows a SEM micrograph of a portion of the Pb plate after being compression molded by the Ni insert. The actual molding temperature was  $41^{\circ}\text{C}$ , or  $\bar{T} = 0.52$ . Similar results were obtained for other molding temperatures. The process of molding has transferred the negative of the protruding features on the Ni insert to the Pb plate, from an array of cylindrical microposts on the insert to an array of cylindrical microholes on the plate. As is evident in Fig. 8.2(a), defective Ni microposts on the insert lead to defective microholes on the Pb plate. Figure 8.2(b) shows a SEM micrograph of a typical microhole, showing the well-defined top rim and the sharp transition from the top

surface to the vertical sidewalls. Figure 8.2(c) shows in more detail the transition region from the sidewall to the bottom of the microhole: it reveals this transition to be as sharp as at the top rim. Instead of being perfectly smooth, a sidewall roughness is generated by the molding process, with a series of circumferential striations perpendicular to the molding direction. Overall, Fig. 8.2 demonstrates that a multitude of sharply defined, high-aspect-ratio, microscale features in Pb can be successfully generated in parallel by micromolding with LiGA fabricated Ni inserts, and illustrates the potential of high temperature micromolding for metal-based HARMS fabrication.



**Fig. 8.1 Ni insert condition after repeated Pb micromolding runs in the temperature range of 30-220°C: (a) a low magnification SEM micrograph (the circle highlights a defective Ni micropost); (b) a higher magnification SEM micrograph of a typical Ni micropost**



**Fig. 8.2 Morphology of molded Pb plate: (a) a low magnification SEM micrograph (the circle highlights a defective Pb microhole due to a defective micropost on the insert)**

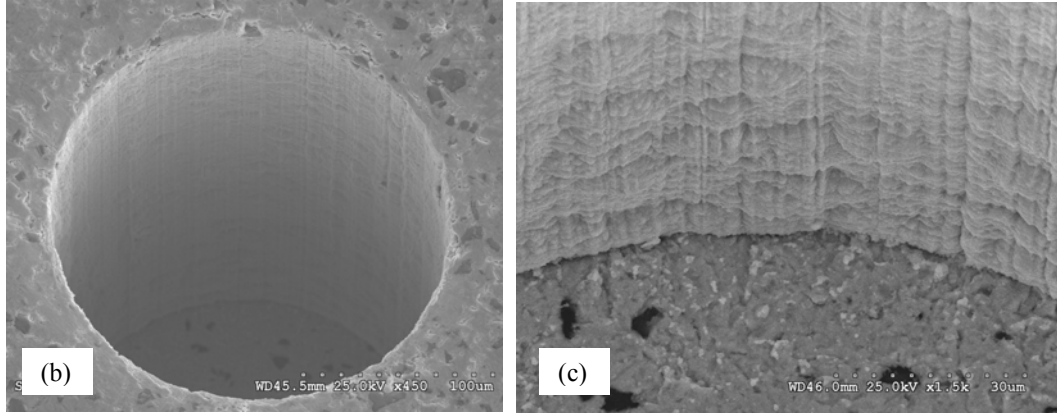


**Fig. 8.2 (continued) (b) a higher magnification SEM micrograph of a typical Pb microhole; (c) a higher magnification SEM micrograph of the sidewall to bottom transition within a Pb microhole**

Figure 8.3(a) shows the measured total compressive force on the Ni insert,  $P$ , versus the insert displacement,  $d$ , into the molded Pb plate, again at 41°C. The  $P$ - $d$  curve is initially concave upwards with  $P$  increasing rapidly with increasing  $d$ . Thereafter there is a slowdown in force increase with further increase in  $d$  and a curvature change to convex. As  $d$  increases even further,  $P$  becomes approximately linearly proportional to  $d$ . Figure 8.3(b) shows a series of measured  $P$ - $d$  curves with molding runs at temperatures ranging from ~30°C to ~120°C. At all temperatures, the measured  $P$ - $d$  curves exhibit the same general features as described in Fig. 8.3(a). The maximum molding force, observed at the maximum molding depth of 500μm, is seen to decrease monotonically with increasing molding temperature. In order to understand experimentally observed trends for compressive molding forces and companion stresses during molding, some simple modeling is undertaken next.

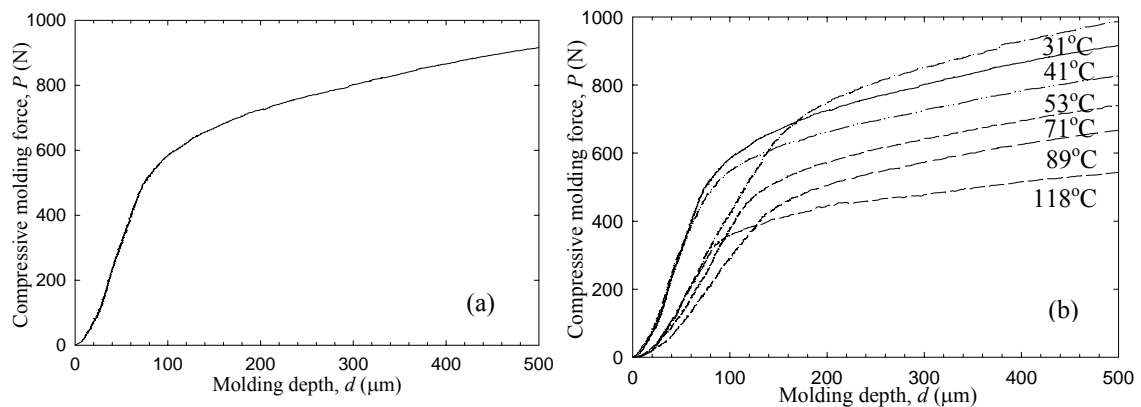


**Fig. 8.3 Measured Pb micromolding response: (a) a typical force versus depth curve obtained from a Pb molding run at 41°C; (b) molding force versus molding depth curves obtained from Pb molding runs at temperatures ranging from 31°C to 118°C**

## Development of a Simple Model: Ball Indentation Stresses

### A. Basic Approach

To gain some appreciation of the physics underlying the response of molding force to micropost depth, one could undertake a stress analysis of the process. As has been done for ball indentation, it may be possible to track the stresses that accumulate as posts are pushed into a plate with finite element analysis (FEA). However, even with FEA using advanced contact elements (e.g., Refs. 24, 25) and the considerable computational capability accessible today, such a stress analysis is an extensive undertaking for post indentation. In the first instance, this is because of the unusually high stresses and stress gradients initially produced by a post compared to a ball (e.g., Fig. 8.4 for the normal contact stress for a post,  $\sigma_c$ , positive when compressive). In the second, it is because of the nonlinearities attending the varying contact regions with friction present, friction being of considerably more importance for a post than for a ball. In the third, it is because of the more extensive yielding and larger plastic strains accumulated with post indentation (the yield region for a post at the maximum penetration is about twice the size of that for a ball with the same contact radius). As a result, here instead a simpler, albeit approximate, approach is adopted. This approach draws on the physical understanding already available for a ball pressed into a half-space. By paralleling this spherical indentation process, some appreciation of the physics involved in the present molding process is gained. Accordingly, next ball indentation is briefly reviewed (see Ref. 26 for a more complete exposition).

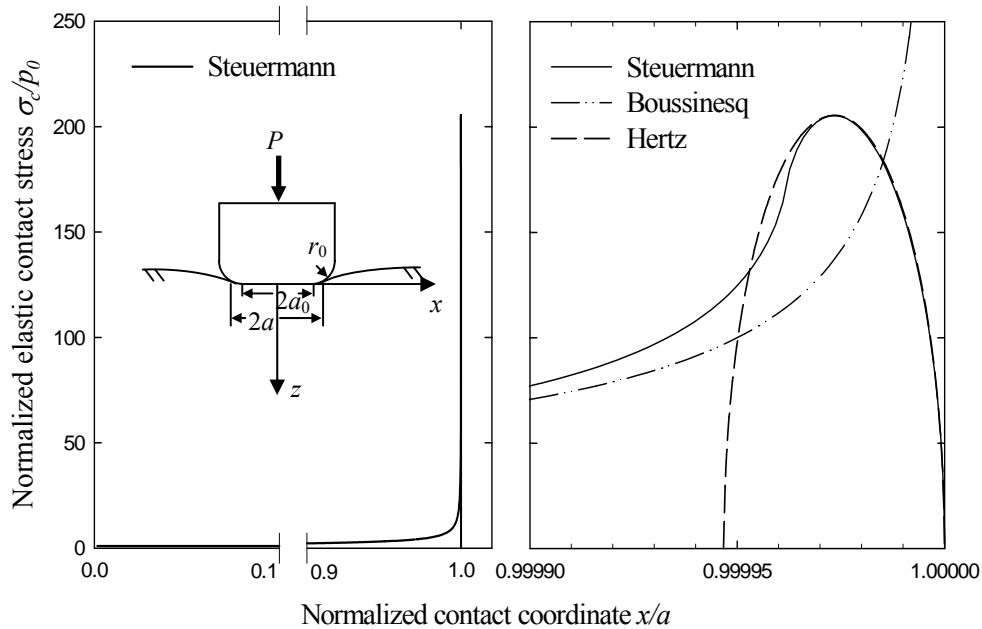


**Fig. 8.4 Elastic contact stresses for rigid frictionless punches indenting an elastic half-space: (left) contact stress for a strip punch normalized by the value at the center of the punch as a function of the normalized contact coordinate,  $x/a$ ; (right) contact stress distributions close to the point of maximum stress concentration**

In Fig. 8.5, the response of an elasto-plastic half-space to normal indentation by a relatively-rigid ball is summarized. The ball has radius  $R$  and is under an increasing compressive force  $P$  acting in the  $z$ -direction (see sketch in the initial elastic region of Fig. 8.5). This  $P$  produces contact over a circle of radius  $a$ . Hence the average contact pressure produced is  $p = P/\pi a^2$ . By definition,  $p$  is the Meyer hardness. In Fig. 8.5, this hardness dependence on contact extent is tracked from an elastic stress state, through an elasto-plastic state, to a state termed fully plastic. In what follows, the response in these states is described by drawing on results in the literature.

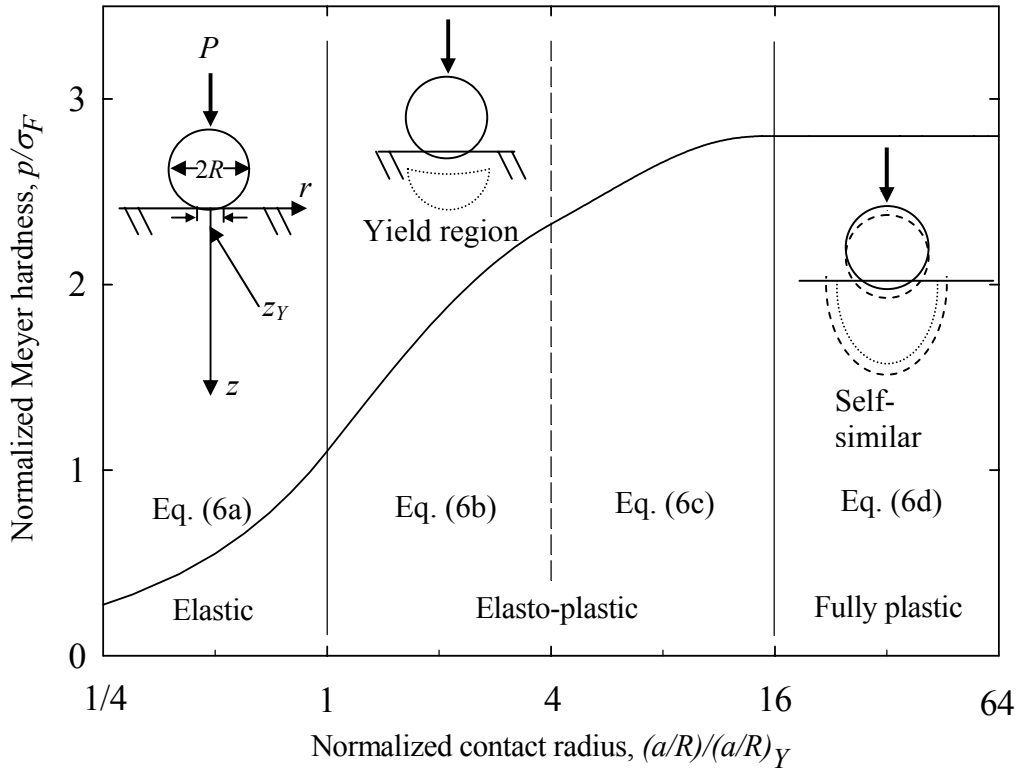


**Fig. 8.5 Response of an elasto-plastic half-space to ball indentation: the normalized contact pressure versus normalized contact radius curve is a fit to numerical results of  $p$ FEA and given in Eq. (6). Different indentation regimes are illustrated in the sketches within the graph**

### B. Elastic Response

When the rigid ball is frictionless and the half-space is purely elastic, the dependence of the average contact pressure on the contact radius is, from Hertz<sup>27</sup>,

$$p = \frac{4}{3\pi} \frac{E}{1-\nu^2} \frac{a}{R}, \quad (1)$$

where  $E$  is the Young's modulus of the half-space and  $\nu$  is its Poisson's ratio. Friction can increase  $p$  of Eq. (1) by at most 5% for a given  $a$ <sup>28</sup>. Consequently Eq. (1) is adopted here irrespective of the level of friction present.

The limit on the use of Eq. (1) can be found by determining the pressure that first induces local yielding. This yielding occurs at a point on the  $z$ -axis beneath the ball. Analyzing the interior stresses, using either a Tresca or a von Mises yield criterion, furnishes the pressure at yield  $p_Y$  and its location  $z_Y$  as functions of Poisson's ratio<sup>29</sup>,

$$\begin{aligned} p_Y &= \sigma_Y (0.866 + 0.59\nu + 0.36\nu^2), \\ z_Y &= 0.382a(1 + 0.87\nu), \end{aligned} \quad (2)$$

where  $\sigma_Y$  is the yield strength. The fit for  $p_Y$  implicit in Eq. (2) is accurate to within 0.1%.

The indentation response depicted in Fig. 8.5 actually corresponds to that for a 304L stainless steel ( $E = 193$  GPa,  $\nu = 0.28$ ,  $\sigma_Y = 243$  MPa). This choice of material enables the use of previous FEA results for the hardness once yielding commences (from Ref. 30, henceforth denoted  $p$ FEA). Consequently Eq. (2) has  $p_Y = 1.1\sigma_Y$  as the limit for purely elastic stresses. Then the companion value of  $(a/R)_Y$  follows from Eq. (1). Thus throughout the elastic state

$$\frac{p}{\sigma_Y} = 1.1 \left( \frac{a}{R} \right) / \left( \frac{a}{R} \right)_Y, \quad (3)$$

for  $p \leq p_Y$ . This response shows as a curve in Fig. 8.5 rather than a straight line because of the log scale employed on the horizontal axis.

### C. Plastic Response

Once the contact pressure exceeds  $p_Y$ , yielding commences. The ensuing plastic flow is taken to be governed by the hardening curve from uniaxial tension testing of 304L stainless steel in  $p$ FEA. One possible equation for such a curve has  $\sigma/\sigma_Y = (\varepsilon/\varepsilon_Y)^n$ , where  $\sigma, \varepsilon$  are uniaxial stress and strain values, respectively,  $\varepsilon_Y = \sigma_Y/E$  is the uniaxial yield strain, and  $n$  is the strain hardening exponent (typically  $0 \leq n \leq 1/2$ ). This equation suggests the form for the fit used here for  $p$  early in the elasto-plastic state.

Tabor<sup>31</sup> was first to appreciate that, as loading force and extent of indentation are increased; the plastic response in ball hardness tests could approach a self-similar state. In such a self-similar state, yield region extents in both the horizontal and vertical directions approach respective constant factors times the contact radius (indicated in the sketch in the fully plastic region of Fig. 8.5). This expectation is confirmed experimentally<sup>32</sup> and analytically in  $p$ FEA to within about  $\pm 30\%$ . Given a degree of self-similarity, Tabor also expected that the hardness  $p$  should approach a steady-state response, provided it could be normalized by an appropriate flow stress. This flow stress has to reflect the fact that, with work hardening ( $n > 0$ ), the stresses within self-similar yet expanding yield regions continue to grow as loading force increases. To this end, Tabor chose a representative flow stress  $\sigma_F$  as given by the uniaxial  $\sigma - \varepsilon$  curve for the indented material at a representative flow strain  $\varepsilon_F$ . He further chose  $\varepsilon_F$  to reflect experimentally-obtained strain values near the edge of contact, thereby capturing the increases in both stress and strain that occur with further indentation. Approximately Tabor's choice results in



$\varepsilon_F \approx a/5R$ . Then  $\sigma_F$  follows from the uniaxial stress strain curve. With this flow stress, Tabor experimentally finds that typically

$$\frac{p}{\sigma_F} = 2.8, \quad (4)$$

in what he terms the fully plastic state. This value is also confirmed analytically in *p*FEA.

Here, then, the following normalized hardness  $\bar{p}$  and contact radius  $\bar{a}$  are adopted for the entire hardness curve (Fig. 5):

$$\bar{p} = \frac{p}{\sigma_F}, \quad \bar{a} = \left( \frac{a}{R} \right) / \left( \frac{a}{R} \right)_Y. \quad (5)$$

The first of these follows from Eq. (4), with the added proviso that  $\sigma_F \geq \sigma_Y$  because now the flow stress is being used throughout. The second simplifies initial elastic response as in Eq. (3). With the normalizations of Eq. (5), the entire hardness curve computed in *p*FEA can be fitted to within 1.5% by the following expressions:

for *elastic* stress states ( $0 \leq \bar{a} \leq 1$ ),

$$\bar{p} = 1.1\bar{a}; \quad (6a)$$

for *early elasto-plastic* stress states ( $1 \leq \bar{a} \leq 4$ ),

$$\bar{p} = 1.1\bar{a}^n, \quad n = \bar{a}^{-4/9}; \quad (6b)$$

for *late elasto-plastic* stress states ( $4 \leq \bar{a} \leq 16$ ),

$$\bar{p} = 2.8 - \frac{9}{8} \left( 1 - \frac{\bar{a}}{16} \right)^3; \quad (6c)$$

and for *fully plastic* stress states ( $16 \leq \bar{a}$ ),

$$\bar{p} = 2.8. \quad (6d)$$

The fit of Eq. (6) is what is actually shown in Fig. 5.

It is possible to adjust the fits in Eq. (6) somewhat for other values of Poisson's ratio (recall  $\nu = 0.28$  in *p*FEA, hence effectively in Eq. (6)). One uses Eq. (2) to alter the common coefficient in Eqs. (6a, b), then adjusts the exponent in the second of (6b) so that its magnitude matches that of Eq. (6c) at  $\bar{a} = 4$ . This results in exponents ranging from about  $-2/9$  to  $-5/9$ . No further adjustments need be made. This is because  $\nu \rightarrow 1/2$  underlies Eqs. (6c, d), irrespective of its elastic value. This is consistent with the accepted model of plastic flow as being incompressible.

While Eq. (6) is based on a theoretical determination in *p*FEA, there is nonetheless some experimental support of its validity<sup>31 32 34</sup>. Typically experimental results are within 5% of Eq. (6): this is shown for seven different metals and for a range of indentations spanning both elasto-plastic and fully plastic response.

As a final comment on Eq. (6), it is noted that *p*FEA also carries out its finite element simulation assuming complete adhesion of the ball with the half-space. This interface condition represents an upper bound on the possible effects of friction. Even so,  $\bar{p}$  values do not vary much, consistently shadowing the curve shown in Fig. 5 and being about 3% above it. In all, then, Eq. (6) can be expected to be applicable to quite a wide range of metals and indentation conditions. Next, therefore, adaptation of the ideas underlying Eq. (6) to the post micromolding experiments of Section II is sought.

## Development of a Simple Model: Post Indentation Stresses

### A. Basic Approach

The experiments of Section II involved right circular cylinders as indenters. Furthermore, the experiments of Section II in effect tracked stresses as an array of such Ni microposts was pressed into a Pb plate. The model developed here simplifies the experimental configuration by considering the stresses produced as a *single rigid* post is pressed into a Pb *half-space*. Some justifications of these simplifications follow. In these and subsequent justifications in this section, simplifications that introduce 10% or less error are judged to be acceptable.

First, the center-to-center spacing of the posts in the experiments is  $8R$ , where  $R$  is now the radius of a post. Later in this development, stresses at a radial distance of  $2R$  away from the center of an isolated post are used. When response is elastic, the stresses at such a location stemming from an additional rigid post  $8R$  away from the original are less than 0.2% of  $p$ , where  $p = P/\pi R^2$  is now the average pressure on a post (the value of  $\nu$  taken here is 0.44 for Pb)<sup>35 36</sup>. When the response is elasto-plastic, no analysis would appear to be available. However, as a rough estimate of interaction effects, the elasto-plastic response to spherical indentation can again be considered. From *p*FEA, at a radial station 6 times the contact radius (cf.  $8R - 2R$ ), stresses in the fully plastic state can be estimated as being less than 5% of  $p$ . Both of these estimates, then, would suggest that interaction effects can reasonably be ignored for the present experimental configuration, and just a single indenting post modeled.

Second, to be relatively rigid during elastic and elasto-plastic indentation, both the Young's modulus and the yield strength of the post need to be an order of magnitude larger than those of the material being indented. Over the range of temperatures treated in the experiments, the  $E$  for Ni is greater than that for Pb by at least a factor of 12, while the  $\sigma_y$  for Ni is greater than that for Pb by at least a factor of 50<sup>21</sup>. Both of these factors, then, support treating the post as rigid. Experimental observations of Ni microposts after repeated indentations into Pb also support such a simplification.

Third, the plate material beneath the deepest penetration in the experiments still has a thickness greater than  $50R$ . If the plate is treated as being of this thickness and resting on a frictionless rigid surface, by reflection this configuration is tantamount to having an additional indenting post, aligned with the original but opposing it in direction, acting at a depth of  $100R$ . Stresses from such a second post in the vicinity of the original post are of the order of  $10^{-4}$  times those of the original post<sup>35</sup>. Hence treating the plate as a half-space is reasonable.

In Fig. 8.6, the response of an elasto-plastic half-space to normal indentation by a rigid, right circular, cylinder is shown schematically. This response is in terms of the average contact pressure  $p$  acting as the depth of penetration  $d$  increases. As in Fig. 8.5, elastic, elasto-plastic, and fully plastic states can be identified. Responses in these different states are developed primarily by drawing on results in the literature and analogous results for Fig. 8.5.

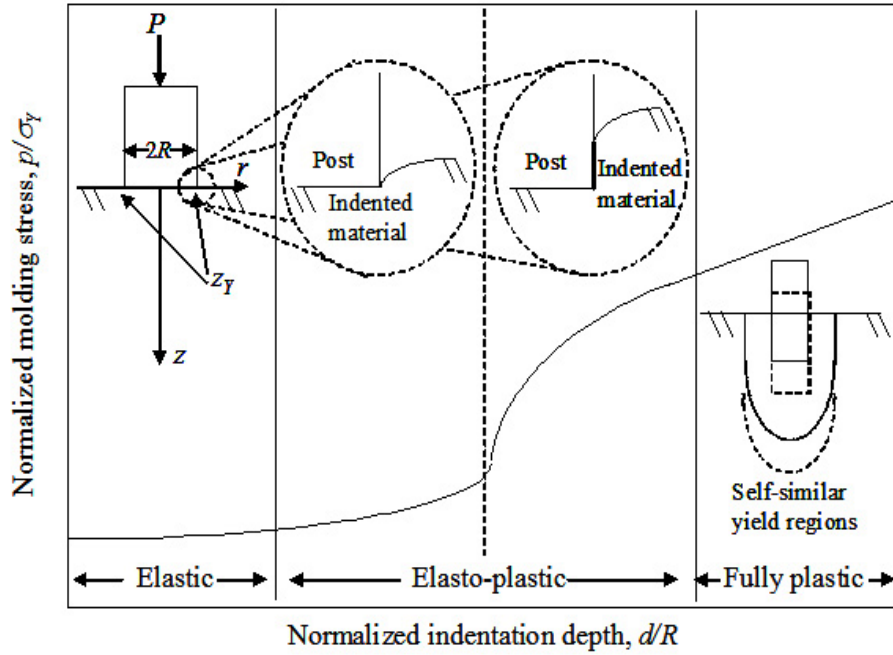


**Fig. 8.6 Schematic of the response of an elasto-plastic half-space to post indentation: the normalized molding stress versus normalized indentation depth curve delineates the various indentation regimes, which are illustrated with the sketches within the graph. The indentation depth is not drawn to scale**

### B. Elastic Response

When the cylinder is frictionless and the half-space purely elastic, the dependence of average contact pressure on penetration depth is, from Boussinesq<sup>37</sup>,

$$p = \frac{2}{\pi} \frac{E}{1-\nu^2} \frac{d}{R}. \quad (7)$$

Friction on the end of the cylinder for the Poisson's ratio of Pb ( $\nu = 0.44$ ) only increases  $p$  of Eq. (7) by 0.5%<sup>38</sup>. Consequently friction effects on the *end* of the cylinder are ignored henceforth.

The flat-ended cylinder in Boussinesq<sup>37</sup> has sharp corners. This leads to the contact stress distribution  $\sigma_c = p / 2\sqrt{1-(r/R)^2}$ , where  $r$  is the radial coordinate ( $0 \leq r < R$ , Fig. 6). That is, a contact stress which is singular at the edges of contact. While this singularity is integrable and accordingly the resulting  $p$  is probably acceptable in the relation of Eq. (7), the associated stresses are useless in themselves for determining the pressure first producing yielding, and hence the limit on the use of Eq. (7). Needed instead is a stress analysis which takes into account the finite, albeit small, radii of curvature that are actually present on the corners of the posts in the experiments.

Apparently no such stress analysis is available in the literature for a cylindrical punch. However, there does exist an analytical determination of the contact stress for a rigid strip punch with a flat and two quarter-circular edges (as in sketch included in Fig. 4). This analysis is provided by Steuermann<sup>39</sup> (here as reported in Ref. 40). Moreover, it

can be expected that this plane strain analogue of the actual, axisymmetric, post configuration shares the same contact stress distribution (on normalizing by  $p_0$ , the pressure at the origin, and exchanging the horizontal rectangular coordinate,  $x$  of Fig. 4, for the radial coordinate,  $r$  of Fig. 8.6). This expectation stems from asymptotics which show it to be asymptotically true near the edges of contact<sup>41</sup>, from a common  $\sigma_c$  for a roller and a ball<sup>27</sup>, and from a common  $\sigma_c$  for a flat-ended strip and a flat-ended cylinder<sup>42 37</sup>. Accordingly the contact stress of Steuermann is adopted here for elastic response.

From Steuermann (Eq. (35), Ref. 40), the average pressure under a rounded strip,  $p = P/2a$ , is given in terms of the contact extent  $2a$  by

$$p = \frac{E_c a}{4r_0} \left[ \cos^{-1} \left( \frac{a_0}{a} \right) - \left( \frac{a_0}{a} \right) \sqrt{1 - \left( \frac{a_0}{a} \right)^2} \right], \quad (8)$$

where  $2a_0$  is the contact flat extent and  $r_0$  the edge radius (Fig. 4), while  $E_c = \left[ (1-\nu^2)/E + (1-\nu_p^2)/E_p \right]^{-1}$  is the Young's modulus for contact (this last does take into account the compliance of the strip thus post, the latter entering through the post elastic moduli,  $E_p, \nu_p$ ). The contact stress distribution leading to Eq. (8) is more conveniently expressed by mapping the horizontal coordinate with  $x = a \cos \theta$ . Then  $\sigma_c = \sigma_c(x) = \sigma_c(\theta)$  with

$$\sigma_c = \frac{E_c a}{2\pi r_0} \left\{ 2\theta_0 \sin \theta + \ln \left[ \left| \frac{\sin(\theta_0 + \theta)}{\sin(\theta_0 - \theta)} \right|^{\cos \theta} \left| \frac{\sin \theta_0 - \sin \theta}{\sin \theta_0 + \sin \theta} \right|^{\cos \theta_0} \right] \right\}, \quad (9)$$

where  $\theta_0 = \cos^{-1}(a_0/a)$  (Eq. (9), Ref. 40). In Fig. 4, a plot of the contact stress of Eq. (9) is given for rounding typical of the Ni microposts used in the molding experiments ( $r_0/a_0 \sim 0.03$ ), and material properties representative of the Ni posts and Pb plate in these experiments (at 31°C on the point of yield). As noted earlier, it features an unusually sharp stress peak near the edge of contact (by symmetry, there is a second such peak at  $x = -a$ ). Over most of the contact region (99.9%), the contact stress in Fig. 8.4 coincides with its singular counterpart, the two being indistinguishable on the scale of Fig. 8.4. Eventually, as the edge of contact is approached, the two have to diverge, as illustrated on the expanded  $x$ -scale in Fig. 8.4.

In order to obtain the contact pressure producing first yielding,  $p_y$ , the peak contact stress attending Eq. (9) needs to be determined. By differentiating Eq. (9), this can be shown to occur at  $\theta = \theta_*$ , where  $\theta_*$  satisfies

$$2\theta_0 = \tan \theta_* \ln \left[ \frac{\tan \theta_0 + \tan \theta_*}{\tan \theta_0 - \tan \theta_*} \right], \quad (10)$$

$0 < \theta_* < \theta_0$ . The corresponding stress concentration factor is  $K_T = \sigma_c(\theta_*)/p$ .

First yielding can be expected to occur beneath the peak stress. The stress distribution near this peak is similar to the plane-strain Hertzian distribution for contact with a long roller. Both share the same asymptotic behavior as the edge of contact is

approached  $\left(\sqrt{1-(x/a)}\right)$  as  $x \rightarrow a^-$ ). Thus when both are given the same peak value, they are almost indistinguishable for contact between the location of the peak stress and the edge of contact (see expanded  $x$ -scale in Fig. 8.4). Inside the peak stress location, they differ (Fig. 4). Nonetheless it would seem reasonable to approximate the contact stress of Eq. (9) by a Hertzian distribution near its peak. Then the interior stresses beneath the peak are available<sup>43</sup>.

The stresses in Ref. 43 vary with Poisson's ratio. Here, ultimately the results of the plane strain analyses in Refs. 40 and 43 are to be applied to the axisymmetric post configuration representative of the experiments in Section II. To this end,  $\nu = 1/2$  is taken because this value makes the out-of-plane normal stress in plane strain coincide with its axisymmetric counterpart. With  $\nu = 1/2$ , first yielding using the Tresca criterion occurs when<sup>43</sup>

$$p_Y = \frac{5\sigma_Y}{3K_T} \text{ at } z_Y = 0.786\Delta a, \quad (11)$$

where  $\Delta a = a(1 - \cos \theta_*)$ .

In general, to determine actual values of  $p_Y$  requires Eqs. (8)-(11) be solved simultaneously. This requires an iterative approach because, with conforming contact,  $a$ , and hence  $K_T$ , depend on the load. Here, however, the relatively sharp corners involved enable a simpler solution procedure. For  $r_0/a_0 \leq 1/10$ , Eq. (10) gives  $\theta_* = 5\theta_0/6$  (to within 0.1%). Furthermore, with this  $\theta_*$ , if at yield

$$\theta_0 = \theta_Y = \frac{5}{3} \sqrt{\pi \left(\frac{r_0}{a_0}\right) \left(\frac{\sigma_Y}{E_c}\right)} \leq \frac{1}{10}, \quad (12a)$$

then the following approximate results hold (to within 0.2% for  $p_Y$ ):

$$K_T = \frac{9}{10\theta_Y}, \quad p_Y = \frac{50}{27} \sigma_Y \theta_Y. \quad (12b)$$

In Eq. (12b), the pressure has been adjusted so that the cylinder and strip share a common  $p_0$  using values for flat-ended indenters because of the small radii of curvature of the posts. For the post configuration of the present experiments,  $\theta_Y$  is indeed less than  $1/10$ , and the determination of first yielding follows directly from Eq. (12).

### C. Plastic Response

Pressures exceeding  $p_Y$  of Eq. (12), with consequent plastic flow, occur very early on in molding experiments because of the high  $K_T$  involved (e.g., Fig. 8.4). Again, as the loading force and extent of indentation are increased, the plastic yield region beneath a post can be expected to approach a self-similar state (indicated in the sketch in the fully plastic region of Fig. 8.6). Since here the indentation radius is fixed, self-similarity means a yield region with constant horizontal and vertical extents. Unfortunately, there would not appear to be either experimental or analytical confirmation of this expectation in the literature at this time. Absent such information, the only estimates that would seem to be available for the extents of this steady-state yield region are from ball indentation results.

The analysis of *p*FEA showed that the yield region in the fully plastic state is approximately a semi-ellipse with horizontal minor-axis extent two times the contact radius and vertical major-axis extent three times. Thus here it is assumed

$$r_Y \approx 2R, d_Y \approx 3R, d'_Y = \frac{\pi}{4} d_Y, \quad (13)$$

where  $r_Y, d_Y$  are the radial, vertical yield region extents beneath a post in the fully plastic state. To simplify balancing forces subsequently, this elliptical region is replaced by a rectangular region of the same area and radial extent, but depth  $d'_Y$  (see Fig. 8.7).

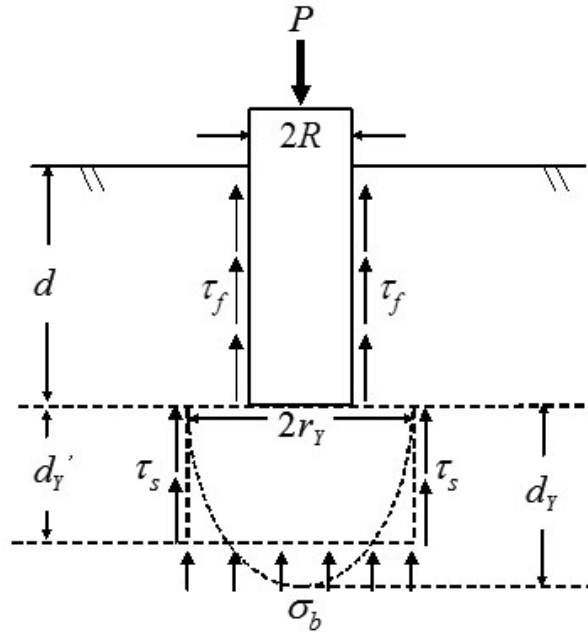


**Fig. 8.7 Cross section showing the force balance used during post indentation in the fully plastic state: the self-similar yield region in front of the advancing post is judged to be semi-elliptical from *p*FEA and further simplified to be rectangular in shape. Resisting pressure on the base of the,  $\sigma_b$ , and resisting shears on the side of the yield region,  $\tau_s$ , are estimated from *p*FEA. Frictional shears,  $\tau_f$ , on the side of the post are characterized by an effective friction coefficient  $f$**

Now to estimate the forces acting in molding experiments, estimates are needed for the resisting pressure on the base of the approximate yield region,  $\sigma_b$ , and the resisting shears on the side of this region,  $\tau_s$  (Fig. 8.7). In addition, there are resisting frictional shears on the sides of a post,  $\tau_f$  (Fig. 8.7). In combination, these tractions provide the resisting force.

To estimate the resisting pressure, again ball indentation results are drawn on. From *p*FEA, at  $z = d'_Y$  on replacing  $a$  with  $R$ ,

$$\sigma_b = \frac{7}{4} \sigma_Y \left[ 1 - \frac{9}{40} \left( \frac{r}{R} \right)^2 \right].$$

This distribution understandably has a peak value under the center of the indenting ball. Here peak values can be expected to occur under the corners on the indenting post. Thus here the peak stress distribution of the ball is maintained but shifted in location to  $r = R$ . One stress distribution that does this, and which also has zero slope at  $r = 0$  as must be the case by symmetry, is:

for  $0 \leq r \leq R/2$ ,

$$\sigma_b = \frac{7}{4} \sigma_Y \left[ \frac{71}{80} + \frac{9}{40} \left( \frac{r}{R} \right)^2 \right]; \quad (14a)$$

for  $R/2 \leq r \leq 2R$ ,

$$\sigma_b = \frac{7}{4} \sigma_Y \left[ 1 - \frac{9}{40} \left( \frac{r}{R} - 1 \right)^2 \right]. \quad (14b)$$

Of course, Eq. (14) is but one adaptation of base pressure from ball to post indentation: others could certainly be made.

On the sides of the yield region, the average shear stress is also estimated from ball indentation results of *p*FEA. On the sides of the post, a representative shear stress is estimated using Coulomb's law and assuming normal stresses there are of the order of the yield strength. Thus

$$\tau_s = \frac{1}{4} \sigma_Y, \tau_f = f \sigma_Y, \quad (15)$$

where  $f$  is an effective friction coefficient.

Now balancing forces on the post, and the approximate yield region in advance of the post, gives

$$\pi R^2 p = 2\pi \int_0^{2R} \sigma_b r dr + 3\pi^2 R^2 \tau_s + 2\pi R d \tau_f,$$

on using  $r_Y$  and  $d'_Y$  of Eq. (13) as yield region extents. In this force balance, any contributions from tractions on  $R \leq r \leq 2R, z = d$  have been taken as negligible. Substituting Eqs. (14) and (15) then gives

$$\frac{p}{\sigma_Y} = 8.8 + 2f \left( \frac{d}{R} \right), \quad (16)$$

for the contact pressure or molding stress in the fully plastic state.

Analogous to hardness testing by spherical indentation, it may be possible to introduce a flow stress for the molding process to effect a coalescing of results for materials with different strain hardening rates. However, given the approximate nature of Eq. (16), such an endeavor would seem premature at this time. Accordingly, here the following simple normalizations are adopted for the molding pressure,  $\bar{p}$ , and depth,  $\bar{d}$ :

$$\bar{p} = \frac{p}{\sigma_Y}, \bar{d} = \frac{d}{R}. \quad (17)$$

Then from Eqs. (7) and (16), the following results are obtained:

for *elastic* stress states ( $0 < \bar{p} < \bar{p}_Y$ ),

$$\bar{p} = k\bar{d}, \quad (18a)$$

where  $\bar{p}_Y = p_Y/\sigma_Y$ ,  $p_Y$  being from Eq. (12), and  $k = 2E/\pi(1-\nu^2)\sigma_Y$ ;

for *fully plastic* stress states ( $\bar{p}_p < \bar{p}$ ),

$$\bar{p} = 8.8 + 2f\bar{d}, \quad (18b)$$

where  $\bar{p}_p$  is the pressure level at which fully plastic response commences, as judged from experiments. The expressions in Eq. (18) for molding with cylindrical posts are the counterpart of those in Eq. (6) for hardness testing using spherical indenters.

It is possible to devise transition fits for elasto-plastic stress states, similar to those of Eq. (6), for inclusion in Eq. (18). This exercise would also seem to be premature at this time. However, some comments on this elasto-plastic transition are appropriate.

Once yielding commences, the indented material can be expected to soften. Then, absent any other physical effects, the slope of the  $\bar{p}$  versus  $\bar{d}$  curve should lessen and possibly flatten, similar to Eqs. (6b, c). With the molding process, though, there is a load level in the elasto-plastic region at which the indented material makes contact with the sides of the post (see sketch in Fig. 8.6). At this point, response stiffens and the  $\bar{p}$  versus  $\bar{d}$  curve can be expected to be concave upwards. Ultimately this “grabbing” of the post should occur over a constant fraction of its length with a consequent steady increase in  $\bar{p}$  with  $\bar{d}$  as in Eq. (18b) (see fully plastic region of Fig. 8.6). Initially, when grabbing commences in the elasto-plastic region, the fraction of the post being grabbed can be expected to change with depth. This implies a steeper slope for the increase in  $\bar{p}$  versus  $\bar{d}$  with grabbing in the elasto-plastic region than in the fully plastic (see elasto-plastic region of Fig. 8.6). Though a more precise quantification of such grabbing effects is beyond the scope of the present simple model, molding experiments can nonetheless be expected to qualitatively reflect such grabbing, and indeed they do (see Fig. 8.3(b)).

To quantitatively compare the foregoing modeling with experiments requires tensile properties of Pb in addition to the force versus depth measurements of Section II. Attention is given to the determination of these tensile properties next.

## Tensile Testing at Elevated Temperatures

### A. Experimental Procedures

In addition to  $\sigma_Y$  of Pb for comparison with Eq. (18), the ratio  $\sigma_Y/E_c$  and hence  $E$  of Pb is needed to use Eq. (12). Although room temperature values of these quantities are available in handbooks, elevated temperature values would not appear to be. Tensile testing was therefore conducted on the same Pb plate materials used in the micromolding experiments and over the same temperature range.

The tensile testing of Pb bar specimens was carried out on the MTS858 single-axis testing system used in the molding experiments. A pair of hydraulic wedge grips, MTS642, was used for specimen holding. Rectangular bar specimens were prepared following standard testing protocols<sup>44</sup>. The bar specimens had an overall length of



200mm and a thickness of 6.25mm. Length and width of the specimen gage section were respectively  $50.0 \pm 0.1$ mm and  $12.50 \pm 0.25$ mm. A MTS632.26F-20 axial extensometer was used to measure the specimen extension. The extensometer had a gage length of 8mm, a maximum extension and compression of  $\pm 1.2$ mm, an accuracy of 0.02% full scale, and a maximum operating temperature of 150°C.

To determine the Young's modulus, each tensile test consisted of multiple partial unloading-reloading cycles, carried out before the ultimate tensile strength of the test specimen was reached. In each unloading-reloading cycle, the unloading segment was performed with a prescribed unloading rate in the force-controlled mode, and the reloading segment was performed with a prescribed displacement rate in the displacement-controlled mode. Displacement rates for the first two reloading segments were 0.05mm/min and 0.10mm/min, respectively. The other reloading segments were executed with the same displacement rate of 0.5mm/min. Three unloading slopes from each experimental  $\sigma$ - $\varepsilon$  curve were averaged together to obtain  $E$ . The Pb modulus measurements were checked by measuring the modulus of Al 1100H (99.9%) with specimens of identical geometry. The Pb yield strength  $\sigma_Y$  was obtained from the experimental  $\sigma$ - $\varepsilon$  curves at 0.2% strain offset using the measured  $E$  value.

A series of such tensile tests were carried out at temperatures ranging from  $\sim 20^\circ\text{C}$  to  $\sim 120^\circ\text{C}$ . The tensile testing temperatures were chosen to be close to (within  $2^\circ\text{C}$ ) the temperatures at which Pb micromolding runs were carried out in this range. Tests at higher temperatures were not conducted due to operating temperature limitations of the extensometer. The temperature of the Pb bar specimens was controlled by wrapping a resistive heating tape around the entire specimen. The resulting elevated temperature was measured by attaching a K-type thermocouple onto the specimen surface. The bar specimens were heated until a steady state temperature was reached before tensile testing began, with a typical temperature variation of  $\pm 3^\circ\text{C}$ . At each temperature, two or three tensile tests were performed following the foregoing procedure.

## B. Experimental Results

Typical tensile testing data are illustrated in Fig. 8.8. Figure 8.8(a) shows three  $\sigma$ - $\varepsilon$  curves measured in the strain range of  $0 < \varepsilon < 0.015$  and at  $41^\circ\text{C}$  corresponding to  $\bar{T} = 0.52$ . Unloading-reloading cycles are shown in Fig. 8.8(a). The sharp bend over of the  $\sigma$ - $\varepsilon$  curves at the onset of plasticity coupled with the relatively slow increase in  $\sigma$  as  $\varepsilon$  increases supports the usual view that Pb is approximately an ideally-plastic material. As shown in Fig. 8.8(b), however, significant strain hardening is clearly evident over a more extended strain range of  $0 < \varepsilon < 0.08$ . The variability of the three  $\sigma$ - $\varepsilon$  curves shown in Fig. 8 is typical of the other tensile experiments.

Figure 8.9 plots measured  $\sigma_Y$  of Pb as a function of temperature, and shows it to decrease smoothly with increasing temperature. A decrease in  $\sigma_Y$  by roughly a factor of 2 is observed as temperature increases from  $\sim 20^\circ\text{C}$  to  $\sim 120^\circ\text{C}$ . Figure 8.9 also plots measured  $E$  of Pb as a function of temperature, and shows a slight decrease as the temperature increases. The measured value of the Young's modulus for Pb is 17.7GPa at  $22.5^\circ\text{C}$ , higher than the handbook value of 16.1GPa<sup>36</sup>. A range of modulus values of Pb is reported, from 13 to 20GPa, depending on the impurity content<sup>45</sup>. Considering the

foregoing, the discrepancy between the presently measured  $E$  of Pb and the handbook value may be due to impurity content. To check that the value of  $E$  obtained here was indeed appropriate for the Pb involved, the modulus of Al was measured using the same test procedures. This measurement gave  $E=71\pm4\text{GPa}$  for Al 1100H, in agreement with the handbook value for the modulus of  $70.6\text{GPa}$  <sup>36</sup>, thereby confirming the appropriateness of the  $E$  measured for Pb here.

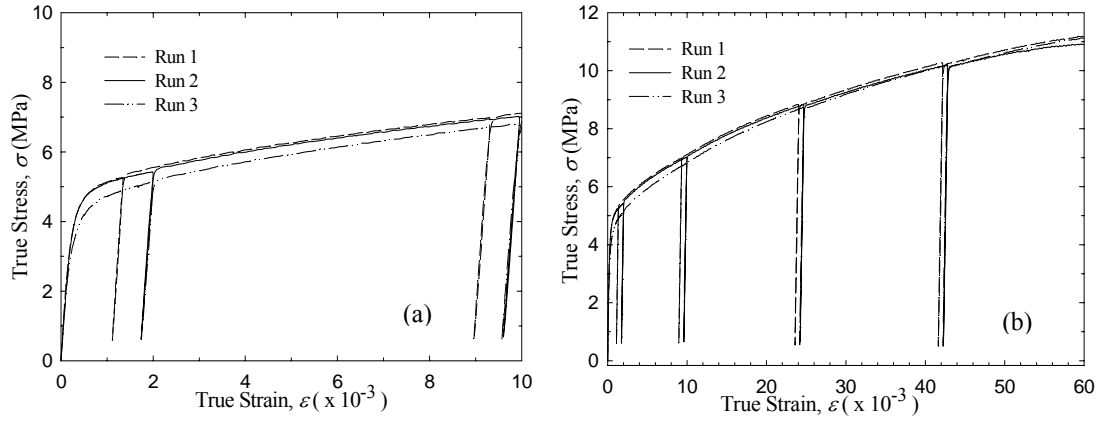


**Fig. 8.8 Results true stress versus true strain curves corresponding to three separate tensile tests on Pb bar specimens at 41°C in the strain range of 0-1% of Pb tensile testing: (a); (b) true stress versus true strain curves obtained at 41°C in the extended strain range of 0-6%**

Using the measured values of  $\sigma_y$  and  $E$ , the ratio of  $\sigma_y/E$  ranges from  $\sim 3.3 \times 10^{-4}$  to  $\sim 2.0 \times 10^{-4}$  as temperature increases from  $\sim 20^\circ\text{C}$  to  $\sim 120^\circ\text{C}$ . These low values of the uniaxial yield strain are as expected for Pb and indicate the low strain level at which plasticity commences for Pb. The ultimate strengths  $\sigma_U$  for Pb at various temperatures were also obtained from these tensile tests <sup>46</sup>. These show a decrease in  $\sigma_U$  with increasing temperature comparable to that for  $\sigma_y$ , indicating that strain hardening of Pb is fairly insensitive to temperature in the range tested.

### Comparison of Experiments with Modeling

To compare measured  $P$ - $d$  curves of Section II quantitatively with the model of Section IV, the total molding force  $P$  is converted to a molding stress  $p$  for a single micropost. This is done by dividing  $P$  by the total number of posts on the insert and the nominal cross-sectional area of one post ( $\pi R^2$ ,  $R = 100\mu\text{m}$ ). The so-calculated molding stresses can then be considered for elastic and plastic response in turn.

To gauge the extent of elastic response using Eq. (12) requires the strain  $\sigma_y/E_c$  and the normalized edge radius  $r_0/a_0$ . The first of these follows from the experiments of the previous section (together with  $E_p = 200\text{GPa}$  and  $\nu_p = 0.31$  <sup>36</sup>, and continuing to take  $\nu = 0.44$  for Pb at all temperatures). For the second, in the present case  $a_0 = R - r_0$ , and

the edge radius is estimated from SEM micrographs of a vertical cross section of a post which give  $r_0 = 3 \mu\text{m}$ . A median value of  $r_0/a_0 = 0.03$  is thus taken. Using Eq. (12) with this median value gives  $\bar{p}_Y = p_Y/\sigma_Y$  in the range

$$0.013 \leq \bar{p}_Y \leq 0.016, \quad (19)$$

as  $T$  varies from 118°C down to 31°C. These low values are a direct result of the high stress concentrations associated with the post indentation geometry ( $K_T = 130$  at 118°C to  $K_T = 102$  at 31°C, the latter being illustrated in Fig. 8.4). The lowest, normalized, molding stress measured in all tests conducted is  $\bar{p} = 0.03$ . Thus there are no experimental values for comparison with Eq. (18a), and the elastic state in the experimentally measured  $\bar{p} - \bar{d}$  curves is essentially nonexistent. This conclusion stands even when the wide range of  $r_0$  estimates ( $2\text{--}4 \mu\text{m}$ ) is admitted (the range in Eq. (19) becomes 0.010-0.019), and indicates that the experimental  $P\text{--}d$  curves shown in Fig. 8.3 reflect completely elasto-plastic and fully plastic responses.

After a transition through elasto-plastic stress states,  $\bar{p}$  enters the fully plastic state. The simple model of Section IV suggests that the molding response should be described by Eq. (18b). If the effective coefficient of friction,  $f$  of Eq. (18b), can be taken as independent of temperature in the range tested here, then Eq. (18b) has that  $\bar{p}_{max}$  at the maximum molding depth ( $\bar{d} = 5$ ) should be a constant. That is,  $p_{max}$  should be linearly proportional to  $\sigma_Y$ . Figure 8.10 shows the dependence of  $p_{max}$  on the different  $\sigma_Y$  values corresponding to the various molding temperatures (the  $\sigma_Y$  values shown in Fig. 8.9). The predicted linear dependence agrees with the experimental data to within experimental scatter for all temperatures.

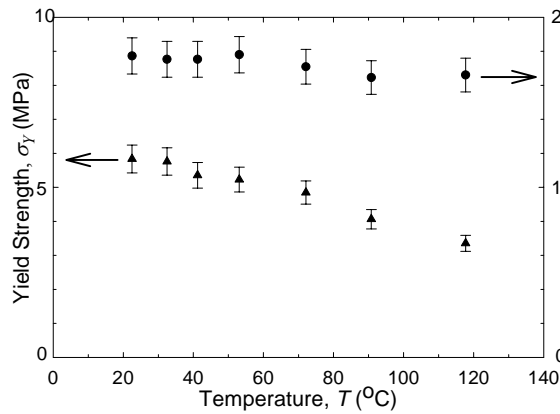


**Fig. 8.9 Measured yield strengths and Young's moduli of Pb as a function of temperature**

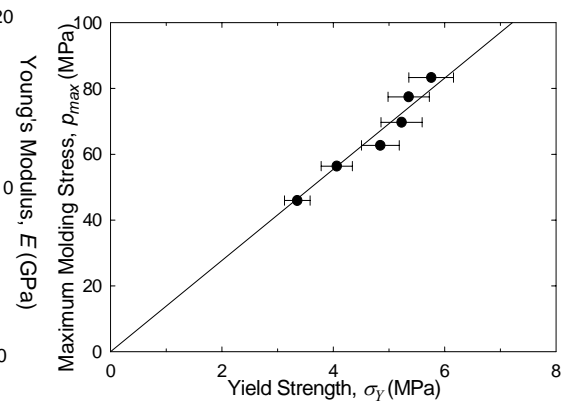


**Fig. 8.10 Measured maximum molding stresses, at a molding depth of 500μm, versus measured Pb yield strengths. Data shown span molding runs and tensile tests conducted in the temperature range of ~30-120°C**

A further consequence of Eq. (18b) is that  $\bar{p}-\bar{d}$  curves approach a single straight line when the indentation response becomes fully plastic. Using the normalization of Eq. (17) together with the  $\sigma_y$  values of Fig. 8.9, experimental data shown in Fig. 8.3(b) are re-plotted in Fig. 8.11. Comparing Figs. 8.3(b) and 11 reveals that, in the fully plastic state (that is, in the range of  $2 < \bar{d} < 5$  judging from data shown in Fig. 8.11), the molding response is significantly closer to a single straight line in the latter figure. In Fig. 8.3(b) at maximum  $\bar{d}$ , the range of  $P$  divided by the mean  $P$  is 57%. In Fig. 11 at maximum  $\bar{d}$ , the range of  $\bar{p}$  divided by the mean  $\bar{p}$  is 12%. Thus the simple normalization of Eq. (17) leads to a coalescence of molding data with nearly a factor of 5 less variation, in support of Eq. (18). The variation remaining after this normalization is comparable to the scatter in the Pb yield strength measurements.

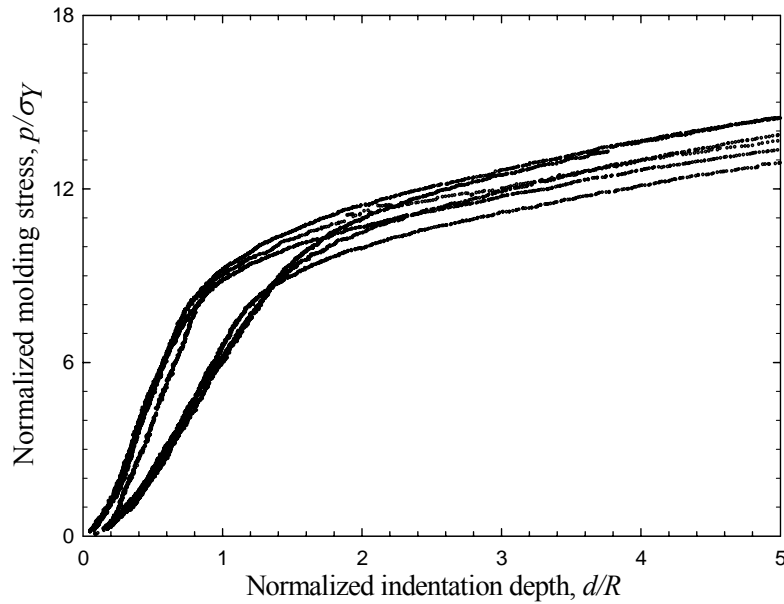


**Fig. 8.11 Normalized molding response: molding stress normalized by the Pb yield strength at the molding temperature versus molding depth normalized by the post radius**

Also apparent in Fig. 8.11 is that the lines in the fully plastic state are nearly parallel. This further supports  $f$  being independent of  $T$  for the ranges of temperatures considered here. Given this, it is appropriate to try and actually fit Eq. (18b) to the experimental data, the one parameter to be so determined being  $f$ . Using average  $\bar{p}$  for a given  $\bar{d}$  from Fig. 11 results in

$$f \approx 0.5. \quad (20)$$

This fitted value of  $f$  does not seem to be physically unreasonable. Figure 8.12 shows how  $\bar{p}$  of Eq. (18b) with  $f$  of Eq. (20) compares with an average molding response, obtained by averaging all experimentally determined molding response curves shown in Fig. 8.11. Considering the adaptation made of the spherical indentation results of  $p$ FEA

to the present case of post indentation, the agreement between Eq. (18b) and the experimentally-determined average  $\bar{p}-\bar{d}$  curve in the fully plastic region of  $2 < \bar{d} < 5$  is certainly somewhat fortuitous. Nevertheless, it is believed that the main physical arguments underlying the simple model, namely that the molding response in the fully plastic regime is dominated by a self-similar plastic zone advancing with the micropost together with frictional stresses on the side of the micropost, do find support from the experimental evidence.

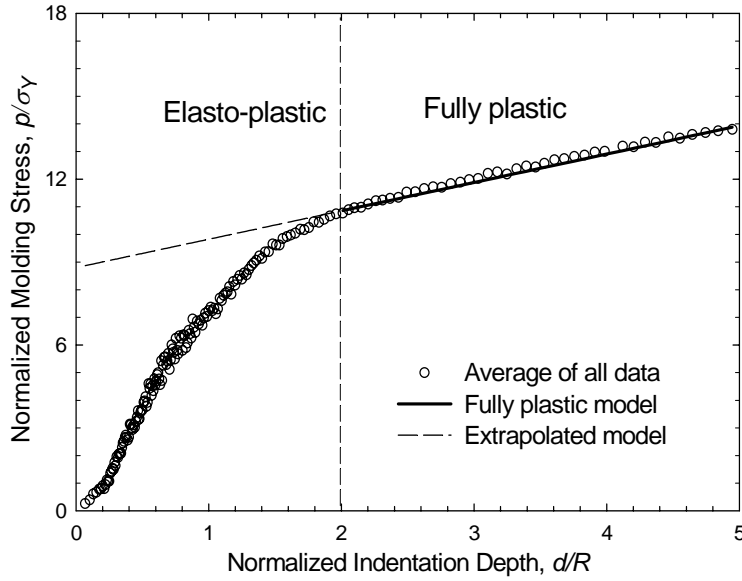


**Fig. 8.12 Experiment-model comparison: the normalized molding response curves obtained in all the molding experiments are averaged together and shown as open circles; the model prediction for the response of post indentation in the fully plastic regime, Eq. (18b), is shown as a solid line (extension of Eq. (18b) into the elasto-plastic regime is shown as a dashed line)**

## Conclusion

While the simple model presented here is consistent with micromolding and tensile testing results on Pb, further experimental verification should be conducted by performing similar experiments on different materials. To our knowledge, no such data exist in the present literature. Assuming, then, the applicability of the simple model to other materials, the average molding response curve shown in Fig. 8.12 offers some guidance to micromolding of metals other than Pb.

First, Fig. 8.12 shows that the contact pressure  $p$  required to reach the fully plastic state ( $d/R \sim 2$ ) is  $\sim 11\sigma_Y$ . Assuming an effective friction coefficient twice that estimated in the present experiments, this implies that, to indent to a similar ratio of depth to lateral dimension, the yield stress of the material making up the mold insert should be  $\sim 16$  times higher than the material to be molded at the molding temperature. The molding

temperature of choice, therefore, reflects a balance between variation of yield strength with increasing temperature for both the insert and the material to be molded.

Second, the increase of  $p$  with increasing molding depth  $d$  in the fully plastic state is proportional to the effective friction coefficient  $f$  generated by insert-metal contact on the sides of the insert. Thus higher  $f$  leads to higher required  $\sigma_Y$  for inserts. Furthermore, the morphology of the sidewalls of the molded microholes consists of a series of circumferential striations perpendicular to the molding direction (as in Fig. 8.2(c)), and this is suggestive of repeated “stick-slip” events. Such “stick-slip” events are generated by insert-metal friction, and the resulting striations markedly increase sidewall roughness of molded features. The increase in sidewall roughness is undesirable for metal-based micro-optical devices. These considerations suggest that engineering insert surfaces to minimize friction may have beneficial effects, and accordingly the influence of temperature and insert-metal friction on molded features merits further study.

Third, the present simple model is based entirely on continuum mechanics, and contains no characteristic length scale. The reasonable agreement between the micromolding and tensile experiments on Pb and the model suggests that continuum mechanics gives a satisfactory description at the length scale of the present experiments (feature size  $\sim 200\mu\text{m}$ , negligible interaction between features), though this is something that should be confirmed by a full FEA of micropost indentation. As the spacing between molded features decreases, a full FEA model of the molding process would also be most helpful in tracking interaction effects. As the characteristic size of the molded features themselves decrease, for example from tens of  $\mu\text{m}$  down to the nm scale, it is an open question whether the present continuum mechanics model would remain satisfactory. As the technology of micromolding advances into the realm of nanofabrication, these issues deserve to be examined.

## References

- 1 L. Huang, W. Wang, M. C. Murphy, K. Lian, and Z. G. Ling, LIGA fabrication and test of a DC type magnetohydrodynamic (MHD) micropump, *Microsystem Technol.* 6 (6), (2000) pp. 235-240
- 2 R. Kondo, S. Takimoto, K. Suzuki, and S. Sugiyama, High aspect ratio electrostatic micro actuators using LIGA process, *Microsystem Technol.* 6 (6), (2000) pp. 218-221
- 3 J. D. Williams and W. Wang, *Microsystem Technol.*, in press (2004)
- 4 C. Harris, K. Kelly, T. Wang, A. McCandless, and S. Motakef, Fabrication, Modeling, and Testing of Micro-Cross-Flow Heat Exchangers, *IEEE J. MEMS* 11(6), (2002) pp. 726-735
- 5 C. Friedrich, P. Coane, J. Goettert, and N. Gopinathin, Precision of micromilled x-ray masks and exposures, *Microsystem Technol.* 4 (1), (1997) pp. 21-24

- 6 H. Lowe and W. Ehrfeld, State-of-the-art in microreaction technology: concepts, manufacturing and applications, *Electrochimica Acta* 44 (21-22), (1999) pp. 3679-3689
- 7 M. Madou, *Fundamentals of Microfabrication* (CRC Press, Boca Raton, Florida, 2000)
- 8 E. W. Becker, W. Ehrfeld, D. Munchmeyer, H. Betz, A. Heuberger, S. Pongratz, W. Glashauser, H. J. Michel, and V. R. Siemens, Production of Separation-Nozzle Systems for Uranium Enrichment by a Combination of X-Ray-Lithography and Galvanoplastics, *Naturwissenschaften* 69 (11), (1982) pp. 520-523
- 9 M. Hecke, W. Bacher, and K. D. Müller, Hot Embossing - The Molding Technique for Plastic Microstructures, *Microsystem Technol.*, 4(3), (1998) pp.122-124
- 10 V. Piottter, K. Mueller, K. Plewa, R. Ruprecht, and J. Hausselt, Performance and Simulation of Thermoplastic Micro Injection Molding, *Microsystem Technol.*, 8, (2002) pp. 387-390
- 11 D. P. Adams, M. J. Vasile, G. Benavides and A. N. Campbell, Micromilling of Metal alloys with Focused Ion Beam-Fabricated tools, *Precision Engr.—J. of the Int. Soc. For Precision Engr. And Nanotechnol.*, 25 (2), (2001) pp.107-113
- 12 G. L. Benavides, L. F. Bieg, M. P. Saavedra, and E. A. Bryce, High Aspect Ratio Meso-scale Parts Enabled by Wire Micro-EDM, *Microsystem Technol.* 8, (2002) pp.395-401
- 13 K. Takahata, N. Shibaike, and H. Guckel, High-Aspect-Ratio WC-Co Microstructure Produced by the Combination of LIGA and Micro-EDM, *Microsystem Technol.*, 6(5) (2000) pp. 175-178
- 14 R. Ruprecht, T. Gietzelt, K. Muller, V. Piottter, and J. Haubelt, Injection molding of microstructured components from plastics, metals and ceramics, *Microsystem Technol.* 8 (4-5), (2002) pp. 351-358
- 15 R. Ruprecht, T. Benzler, T. Hanemann, K. Müller, J. Konys, V. Piottter, G. Schanz, L. Schmidt, A. Thies, H. Wöllmer, and J. Haubelt, Various Replication Techniques for Manufacturing Three-Dimensional Metal Microstructures, *Microsystem Technol.*, 4(1), (1997) pp. 28-31
- 16 Z. Y. Liu, N. H. Loh, S. B. Tor, Y. Murakoshi, R. Maeda, K. A. Khor, and T. Shimiodzu, Injection Molding of 316L Stainless Steel Microstructures, *Microsystem Technol.* 9, (2003) pp.507-510

- 17 D. M. Cao, D. Guidry, W. J. Meng, and K. W. Kelly, Molding of Pb and Zn with microscale mold inserts, *Microsystem Technol.* 9 (8), (2003) pp. 559-566
- 18 D. M. Cao, T. Wang, B. Feng, W. J. Meng, and K. W. Kelly, Amorphous hydrocarbon based thin films for high-aspect-ratio MEMS applications, *Thin Solid Films* 398/399, (2001) pp. 553-559
- 19 D. M. Cao, W. J. Meng, S. J. Simko, G. L. Doll, T. Wang, and K. W. Kelly, Conformal deposition of Ti-C:H coatings over high-aspect-ratio microscale structures and tribological characteristics, *Thin Solid Films* 429, (2003) pp. 46-54
- 20 D. M. Cao and W. J. Meng, Microscale compression molding of Al with surface engineered LiGA inserts, *Microsystem Technol.* in press, (2004)
- 21 H. S. Cho, K. J. Hemker, K. Lian, J. Goettert, G. Dirras, Measured mechanical properties of LIGA Ni structures, *Sensors and Actuators A*, 103 (1-2), (2003) pp. 59-63
- 22 D. M. Cao, W. J. Meng, and K. W. Kelly, High-temperature instrumented microscale compression molding of Pb, *Microsystem Technol.* 10, (2004) pp. 323-328
- 23 T. B. Massalski (ed.), *Binary Alloy Phase Diagrams*, American Society of Metals, Metals Park, Ohio (1986)
- 24 ABAQUS Standard User's Manual, Revision 6.4, Hibbit, Karlsson and Sorenson Inc., Pawtucket, Rhode Island, (2003)
- 25 ANSYS Advanced Analysis Techniques, Revision 8.0, ANSYS Inc., Cannonsburg, Pennsylvania, (2003)
- 26 G. B. Sinclair and W. J. Meng, A summary of hardness dependence on ball indentation, Report MA 1-04, Mechanical Engineering Department, Louisiana State University, (2004)
- 27 H. R. Hertz, *J. Reine Angew. Math.* 92, 156 (1882)
- 28 D. A. Spence, Hertz contact problem with finite friction, *J. Elasticity* 5 (3-4), (1975) pp. 297-319
- 29 M. T. Huber, *Ann. Phys.* 14, 153 (1904)
- 30 G. B. Sinclair, P. S. Follansbee, and K. L. Johnson, Quasi-static normal indentation of an elastoplastic half-space by a rigid sphere .2. Results, *Int. J. Solids Struct.* 21 (8), (1985) pp. 865-888



- 31 D. Tabor, The hardness of metals, Oxford at the Clarendon Press, U.K., (1951)
- 32 L. E. Samuels and T. O. Mulhearn, J. Mech. Phys. Solids 5, 125 (1957)
- 33 P. S. Follansbee and G. B. Sinclair, Quasi-static normal indentation of an elastoplastic half-space by a rigid sphere .1. Analysis, Int. J. Solids Struct. 20 (1), (1984) pp. 81-91
- 34 C. H. Lee, S. Masaki, and S. Kobayashi, Int. J. Mech. Sci. 14, 417 (1972)
- 35 I. N. Sneddon, Fourier Transforms, McGraw-Hill, New York, (1951)
- 36 E. A. Brandes and G. B. Brook (eds.), Smithells Metals Reference Book, 7<sup>th</sup> ed., Butterworth-Heinemann, Oxford, U.K., (1998)
- 37 J. Boussinesq, Application d'es Potentials à l'Etude de l'Équilibre et du Mouvement des Solides Élastiques, Gauthier-Villars, Paris, France, (1885)
- 38 D. A. Spence, Proc. Roy. Soc. A305, 55 (1968)
- 39 I. Y. Steuermann, Contact Problem of the Theory of Elasticity, Gostekhteorizdat, Moscow, U.S.S.R., (1949)
- 40 M. Ciavarella, D. A. Hills, and G. Monno, The influence of rounded edges on indentation by flat punch, Proc. Instn. Mech. Engrs--Part C J. Mech. Engr. Sci. 212 (4), (1998) pp. 319-328
- 41 A. R. Zak, J. Appl. Mech. 31, 150 (1964)
- 42 M. A. Sadowsky, Z. Angew. Math. Mech. 8, 107 (1928)
- 43 M. T. Huber and S. Fuchs, Physikalische Z. 15, 298 (1914)
- 44 American Society for Testing and Materials, Standard Test Methods for Tension Testing of Metallic Materials E8 (2001)
- 45 D. R. Lide (ed.), CRC Handbook of Chemistry and Physics, CRC Press, Boca Raton, Florida, (2003)
- 46 In the range of temperatures tested,  $22 \leq T \leq 118^\circ\text{C}$ , data for  $\sigma_U$  can be represented to within 2% by the following fit:  

$$\sigma_U = 14 - 3\Delta T + 0.3\Delta T^2 \text{ in MPa, where } \Delta T = (T - 22)/20 \text{ and } T \text{ is in } ^\circ\text{C}$$

## CHAPTER 9. GLOBAL CONCLUSIONS

Micro-electro-mechanical-systems (MEMS) and microscale mechanical and chemical devices have been researched for over two decades, hailed for their tremendous market potential, and riled for not having fulfilled the more exuberant predictions of success. Despite these ups and downs, commercial products employing MEMS and microsystems have nonetheless emerged in our everyday lives. Examples include automotive accelerometers and various sensors.

It is safe to state that, at the present time, products employing silicon based MEMS are far more developed as compared to microsystems built from metal-based microscale structures. This more advanced state of silicon MEMS technology results from the existing prior art, which is the fifty-year investment into fabrication of integrated electronic circuits. However, it is believed that metal-based microsystems enjoy some inherent advantages over silicon-based microdevices, especially in the area of harsh-environment-compatible devices. Examples include, but certainly not limited to, devices subjected to high temperatures (micro heat exchangers), placed in contact with corrosive chemicals (micro chemical reactors), and under high mechanical stresses. It is believed that one important factor to commercial realization of metal-based microdevices is efficient and economical fabrication.

As stated in the introductory part of this dissertation, several approaches to fabricating metal-based microscale structures are being researched in Europe, the U.S., and elsewhere in the world. Techniques such as micromilling and micro-electrical-discharge machining have shown potential as well as limitations. It is probable that no one technique will become the panacea for fabricating metal-based microdevices. Instead, researchers worldwide constantly add new tools to the arsenal of metal microfabrication.

This dissertation represents some initial steps taken on a new path toward efficient and economical fabrication of metal-based microscale structures, an attempt to add one more tool to the metal microfabrication arsenal. The demonstration of successful micromolding of aluminum at  $\sim 450^{\circ}\text{C}$  in this dissertation is, to our knowledge, the first in the world, and demonstrates the potential of high temperature compression micromolding for fabrication of metal-based microdevices.

The completed work shown in this dissertation also serves to highlight the unfinished business regarding high temperature compression micromolding of metals. Improving the high temperature bulk mechanical properties of the mold insert, increasing the high temperature stability of nanostructured ceramic coatings, and understanding quantitatively the mechanics of micromolding constitute the obvious challenges in the course of perfecting this micromanufacturing technique.

This dissertation also serves to point out one trend in microsystems research, which is the need for a truly interdisciplinary approach. The ultimate success, or failure, of metal-based microdevices will be judged in the market place, and depends critically on a combination of two factors. One is economical device fabrication, which relies on materials science and engineering. The other is innovative device design, which relies on chemistry, physical, and mechanical engineering principals. These two factors may also be interdependent. The realization of these visions will not occur instantly and will serve as an inspiration to others embarking on this exciting journey.

## APPENDIX. LETTERS OF COPYRIGHT PERMISSION

### Permission of Using Published Material from Applied Physics Letters

Sent by: "RIGHTS" <Rights@aip.org>

To: <dcao2@lsu.edu>

cc:

Subject: Re: obtain permission

Dear Dongmei Cao:

Thank you for requesting permission to reproduce material from American Institute of Physics publications.

Permission is granted for the following:

"Friction and wear characteristics of ceramic nanocomposite coatings: titanium carbide/amorphous hydrocarbon", Appl. Phys. Lett. 79, 329 (2001), of which you are an author, to be published as part of your Ph.D. dissertation at Louisiana State University.

Please be sure to include a credit line referencing the original publication.

Sincerely,  
Susann Brailey

~~~~~

Office of the Publisher, Journals and Technical Publications  
Rights & Permissions  
American Institute of Physics  
Suite 1N01  
2 Huntington Quadrangle  
Melville, NY 11747-4502  
516-576-2268 TEL  
516-576-2450 FAX  
rights@aip.org

>>> Dongmei Cao <dcao2@lsu.edu> 06/28/04 10:29AM >>>

To Whom It May Concern:

I am Dongmei Cao/D.M.Cao, the first author of the paper "Friction and wear characteristics of ceramic nanocomposite coatings: titanium carbide/amorphous hydrocarbon", Appl. Phys. Lett. 79, 329 (2001). I would like to put some of the material in this paper into my dissertation. So I need your permission. If you can email to me the permission as soon as possible before July 2, that will be great. Thanks a lot.

My contact information is as follows:

Dongmei Cao  
Louisiana State University

Mechanical Engineering Department  
CEBA 2508, LA, 70803  
(O) 225-5785947, (F) 225-5789195  
dcao2@lsu.edu

### Permission of Using Published Material from Thin Solid Films

Dongmei Cao  
Louisiana State University  
Dcao2@lsu.edu

Dear Dr Cao

***THIN SOLID FILMS***, Vol 398-399, 2001, pp 553-559, Cao et al, "Amorphous hydrocarbon..."  
Vol 429, 2003, pp 46-54, Cao et al, "Conformal deposition..."

As per your letter dated 28 June 2004, we hereby grant you permission to reprint the aforementioned material at no charge **in your thesis** subject to the following conditions:

1. If any part of the material to be used (for example, figures) has appeared in our publication with credit or acknowledgement to another source, permission must also be sought from that source. If such permission is not obtained then that material may not be included in your publication/copies.
2. Suitable acknowledgment to the source must be made, either as a footnote or in a reference list at the end of your publication, as follows:  
  
"Reprinted from Publication title, Vol number, Author(s), Title of article, Pages No., Copyright (Year), with permission from Elsevier".
3. Reproduction of this material is confined to the purpose for which permission is hereby given.
4. This permission is granted for non-exclusive world **English** rights only. For other languages please reapply separately for each one required. Permission excludes use in an electronic form. Should you have a specific electronic project in mind please reapply for permission.
5. This includes permission for UMI to supply single copies, on demand, of the complete thesis. Should your thesis be published commercially, please reapply for permission.

Yours sincerely



Helen Wilson  
Rights Manager

Your future requests will be handled more quickly if you complete the online form at  
[www.elsevier.com/locate/permissions](http://www.elsevier.com/locate/permissions)

**From: Dongmei Cao on 06/28/2004 09:40 AM**

To: permissions@elsevier.com

cc:

Subject: Obtain Permission

To Whom It May Concern:

I am Dongmei Cao/D.M.Cao, the first author of the following two papers:  
"Amorphous hydrocarbon based thin films for high-aspect-ratio MEMS applications",  
Thin Solid Films, Vol.398-399, Issue ER, (2001) pp. 553-559;  
"Conformal deposition of Ti-C:H coatings over high-aspect-ratio micro-scale structures  
and tribological characteristics", Thin Solid Films, Vol.429, Issue 1, (2003) pp. 46-54

I would like to put certain pages in these two papers into my dissertation. So I need to get your permission. If you can email to me the permission as soon as possible before July 2, it would be great. Thanks a lot.

My contact information is as follows:

Dongmei Cao  
Louisiana State University  
Mechanical Engineering Department  
CEBA 2508, LA, 70803

(O) 225-5785947

(F) 225-5789195

dcao2@lsu.edu

#### **Permission of Using Published Material from Microsystem Technologies**

**From: Sturm@Springer.de on 07/01/2004 02:03 PM ZE2**

Sent by: Sturm@Springer.de

To: dcao2@lsu.edu

cc:

Subject: AW: Customer question from springeronline.com

Dear Mr. Cao,

Thank you for your e-mail of June 28, 04.

We are pleased to grant you the permission requested, provided

• Full credit (Springer journal title, article title, name(s) of author(s), volume, page numbers, year of publication, Springer copyright notice) is given to the publication in which the material was originally published.

With kind regards,

Rosita Sturm (Ms.)

\*\*\*\*\*

Rights & Permissions  
Springer-Verlag GmbH  
Tiergartenstrasse 17  
69121 Heidelberg  
GERMANY

Tel: ++ 49 (0) 6221 - 487 8228  
Fax: ++ 49 (0) 6221 - 487 8100  
e-mail: Rosita.Sturm@springer-sbm.com  
internet: www.springeronline.com

**From: Wen Jin Meng <wmeng@alpha2.eng.lsu.edu> on 06/28/2004 11:34 AM EST**

**Sent by:** Wen Jin Meng <wmeng@alpha2.eng.lsu.edu>

**To:** "preuss@springer.de" <preuss@springer.de>

**cc:** dcao2@lsu.edu

**Subject:** Obtain Permission

Dear Ms. Preuss:

My student, Dongmei Cao, who is the first author on three articles in MST, is finishing her Ph.D. Dissertation. She would like to include the work described in these articles in her dissertation, and would like to confirm with you that this use is within the copyright retained for authors. Since her submission deadline is July the second, I would appreciate a prompt return email.

Thank you for your time.

Regards,

Wen Jin Meng

P.S. The three articles in questions are:

D. M. Cao, D. Guidry, W. J. Meng, K. W. Kelly, "Molding of Pb and Zn with microscale mold inserts", *Microsystem Technologies* 9(8), 559 (2003).

D. M. Cao, W. J. Meng, K. W. Kelly, "High-temperature instrumented microscale compression molding of Pb", *Microsystem Technologies* 10, 323 (2004).

D. M. Cao, W. J. Meng, "Microscale compression molding of Al with surface engineered LiGA inserts", *Microsystem Technologies*, in press (2004).

## **VITA**

Dongmei Cao was born on December 21<sup>st</sup>, 1974, in Henan Province, People's Republic of China. In 1992 she entered Sichuan University in Chengdu, China, where she obtained her bachelor's degree in precision instrument engineering in 1996 and master's degree in measurement and control engineering in 1999. In August 1999, she started her graduate study in the Department of Mechanical Engineering at Louisiana State University in the United States of America. She received her master's degree in mechanical engineering from LSU in 2001 and the LSU ME Outstanding Graduate Student Research Award in the same year. She has authored and coauthored seven journal papers by 2003. In 2004, she received the LSU ME Outstanding Research Assistant Award for a second time based on her doctoral dissertation research. Presently, she is a candidate for the degree of Doctor of Philosophy in the Department of Mechanical Engineering of LSU.